PACIFIC EARTHQUAKE ENGINEERING RESEARCH CENTER

Mechanics of Fiber Reinforced Bearings

James M. Kelly
Department of Civil and Environmental Engineering
University of California, Berkeley

Andrea Calabrese
Department of Structural Engineering
University of Naples Federico II

PEER 2012/101
FEBRUARY 2012

Mechanics of Fiber Reinforced Bearings

James M. Kelly
Department of Civil and Environmental Engineering
University of California, Berkeley

Andrea Calabrese
Department of Structural Engineering
University of Naples Federico II

PEER Report 2012/101
Pacific Earthquake Engineering Research Center
Headquarters at the University of California, Berkeley

February 2012

ABSTRACT

The report contains the findings of a study on the mechanical behavior of unbonded fiber-reinforced bearings (FRB). Typical FRBs consist of several layers of rubber that are bonded to fiber reinforcing sheets. The purpose of the reinforcement is to prevent the rubber from bulging laterally under compressive load. The most important aspects of these bearings are (i) they do not have thick end plates; (ii) they are not bonded to the top and bottom support surfaces; and (iii) their reinforcements are very flexible. These aspects may seem to be design deficiencies, but they have the advantage of eliminating the presence of tensile stresses in the bearing by allowing it to roll off the supports when it is sheared. This reduces the typical bonding requirements. The weight and the cost of isolators is reduced by using fiber reinforcing, no end-plates, and no bonding to the support surfaces, offering a low-cost lightweight isolation system for developing countries. This work is the comparison between an approximated linear elastic theory and the outputs of finite element analyses.

ACKNOWLEDGMENTS

The work of the second author was carried out at the Pacific Earthquake Engineering Research Center under a grant (progetto INTERLINK NÂ°147) from the Italian Ministry of Education, University and Research (MIUR) whose support is gratefully acknowledged.

Any opinions, findings, and conclusions or recommendations expressed in this material are those of the authors and do not necessarily reflect those of the PEER Center or other funding agencies.

CONTENTS

LIST OF FIGURES

LIST OF TABLES

1 Introduction

1.1 FIBER REINFORCED ELASTOMERIC ISOLATORS

An analysis is given for the mechanical characteristics of multilayer elastomeric isolation bearings where the reinforcing elements normally steel plates are replaced by fiber reinforcement. The fiber reinforcement, in contrast to the steel reinforcement (which is assumed to be rigid both in extension and flexure), is assumed to be flexible in extension, but completely without flexural rigidity. The influence of fiber flexibility on the mechanical properties of the fiber reinforced isolator, such as vertical and horizontal stiffness, is studied, and it is shown that it should be possible to produce a fiber reinforced isolator that matches the behavior of steel reinforced isolator. The fiber reinforced bearing (FRB) will be significantly lighter and could lead to a much less labor intensive manufacturing process.

Seismic isolation technology in the United States is applied almost entirely to large, expensive buildings housing sensitive internal equipment, for example, computer centers, chip fabrication factories, emergency operation centers, and hospitals. The isolators used in these applications are large, expensive, and heavy. An individual isolator can weight one ton and often more. To extend this valuable earthquake-resistant strategy to housing and commercial buildings, it is necessary to reduce the cost and weight of the isolators. The primary weight in an isolator is due to the reinforcing steel plates, which are used to provide the vertical stiffness of the rubber steel composite element. A typical rubber isolator has two large endplates (around 1 in. thick) and 20 thin reinforcing plates (1/8 in. thick). The high cost of producing the isolators results from the labor involved in preparing the steel plates and the assembly of the rubber sheets and steel plates for vulcanization bonding in a mold. The steel plates are cut, sandblasted, acid cleaned, and then coated with bonding compound. Next, the compounded rubber sheets with the interleaved steel plates are put into a mold and heated under pressure for several hours to complete the manufacturing process. The purpose of this research is to suggest that both the weight and the cost of isolators can be reduced by eliminating the steel reinforcing plates and replacing them with fiber reinforcement. The weight reduction is possible as fiber materials are available with an elastic stiffness that is of the same order as steel. Thus the reinforcement needed to provide the vertical stiffness may be obtained by using a similar volume of very much lighter material. The cost savings may be possible if the use of fiber allows a simpler, less labor-intensive manufacturing process. It is also possible that the current approach of vulcanization under pressure in a mold with steam heating can be replaced by microwave heating in an autoclave.

Another benefit of using fiber reinforcement is that it would then be possible to build isolators in long rectangular strips, whereby individual isolators could be cut to the required size. All isolators are currently manufactured as either circular or square in the mistaken belief that if the isolation system for a building is to be isotropic, it needs to be made of symmetrically shaped isolators. Rectangular isolators in the form of long strips would have distinct advantages over square or circular isolators when applied to buildings where the lateral resistance is provided by walls. When isolation is applied to buildings with structural walls, additional wall beams are needed to carry the wall from isolator to isolator. A strip isolator would have a distinct advantage for retrofitting masonry structures and for isolating residential housing constructed from concrete or masonry blocks.

The essential characteristic of the elastomeric isolator is the very large ratio of the vertical stiffness relative to the horizontal stiffness. This is produced by the reinforcing plates, which in current industry standard are thin steel plates. These plates prevent lateral bulging of the rubber, but allow the rubber to shear freely. The vertical stiffness can be several hundred times the horizontal stiffness. The steel reinforcement has a similar effect on the resistance of the isolator to bending moments, usually referred to as the "tilting stiffness." This important design quantity makes the isolator stable against large vertical loads. The first analysis of the compression stiffness of the steel reinforced isolator was done using an energy approach by Rocard [1973]; further developments were made by Gent and Lindley [1959] and Gent and Meinecke [1970]. In modeling the isolator reinforced with steel plates, the plates are assumed to be in extension and rigid in flexure. The fiber reinforcement is made up of many individual fibers grouped in strands and coiled into a cord of sub millimeter diameter. The cords are more flexible in tension than the individual fibers; therefore, they may stretch when the bearing is loaded by the weight of a building. On the other hand, they are completely flexible in bending, so the assumption made when modeling steel reinforced isolators that plane sections remain plane no longer holds. In fact, when a fiber reinforced isolator is loaded in shear, a plane cross section becomes curved. This leads to an unexpected advantage in the use of fiber reinforcement. When the bearing is displaced in shear, the tension in the fiber bundle (which acts on the curvature of the reinforcing sheet caused by the shear) produces a frictional damping that is due to individual strands in the fiber bundle slipping against each other. This energy dissipation in the reinforcement adds to that of the elastomer.

Recent tests show that this energy dissipation is larger than that of the elastomer. Therefore, when designing a fiber reinforced isolator for which a specified level of damping is required, it is not necessary to use elaborate compounding to provide the damping, but to use the additional damping from the friction in the fibers. To calculate the vertical stiffness of a steel reinforced bearing, an approximate analysis is used that assumes that each individual pad in the bearing deforms in such a way that horizontal planes remain horizontal and points on a vertical line lie on a parabola after loading. The plates are assumed to constrain the displacement at the top and bottom of the pad. Linear elastic behavior in shear is assumed and bulk compressibility is included.

The additional assumption that the normal stress components are approximated by the pressure is made which leads to the well-known "pressure solution," which is generally accepted as an adequate approximate approach for calculating the vertical stiffness. The extensional flexibility of the fiber reinforcement can be incorporated into this approach, and that predictions of the resulting vertical stiffness can be made. A surprising result of this approach to the analysis of the combined response of the pad to the apparently unrelated effects of stretching of the reinforcement and compressibility in the elastomer is that the mathematical structure of the theory is the same for both effects, and that they can be combined in the resulting solution in a simple way. The horizontal stiffness and buckling of the steel reinforced isolator is modeled by an equivalent beam theory whereby a bearing with many discrete pads is replaced by a continuous composite beam with plane sections normal to the undeformed axis assumed to remain plane but not normal to the deformed axis, reflecting the very low shear stiffness of the rubber and the flexural rigidity of the steel reinforcement. When the reinforcement is perfectly flexible in bending, the beam model must be extended to permit the warping of the cross section. The development of lightweight, low-cost isolators is crucial if this method of seismic protection is to be applied to a wide range of buildings—such as housing, schools, and medical centers—in earthquake-prone areas of the world.

2 Flexible Reinforced Bearings under Compression

2.1 INFINITELY LONG STRIP ISOLATORS

2.1.1 Equilibrium in Elastomeric Layer

A layer of elastomer in an infinitely long, rectangular isolator is shown in Figure 2.1. The elastomeric layer has a width of $2b$ and a thickness of t. The top and bottom surfaces of the layer are perfectly bonded to flexible reinforcements that are modeled as an equivalent sheet with a thickness of t_f. A coordinate system (x, y, z) is established by locating the origin at the center of the layer and the y-coordinate direction is attached to the infinitely long side. Under the compression load P in the z-direction, the deformation of the elastomer is in a plane strain state so that the displacement component in the y-direction vanishes. The displacement components of the elastomer in the x- and z-coordinate directions, denoted as u and w, respectively, are assumed to have the form

$$u(x,z) = u_0(x)\left(1 - \frac{4z^2}{t^2}\right) + u_1(x) \tag{2.1}$$

$$w(x,z) = w(z) \tag{2.2}$$

In Equation (2.1), the term of u_0 represents the kinematic assumption that vertical lines in the elastomer become parabolic after deformation; the horizontal deformation is supplemented by additional displacement u_1, which is constant through the thickness and is intended to accommodate the stretch of the reinforcement. Equation (2.2) represents the assumption that horizontal planes in the elastomer remain planar after deformation. The elastomer is assumed to have linearly elastic behavior with incompressibility. The assumption of incompressibility means that the summation of normal strain components is negligible and produces a constraint on displacements in the form

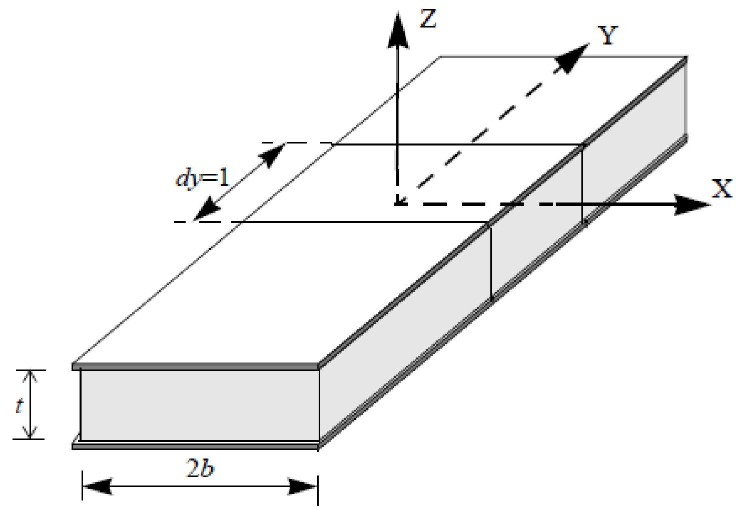

Figure 2.1 Infinitely long rectangular pad showing dimensions.

$$u_{,x} + w_{,z} = 0 \tag{2.3}$$

where the commas imply partial differentiation with respect to the indicated coordinate.

Substitution of Equations (2.1) and (2.2) into the above equation gives

$$u_{0,x}\left(1-\frac{4z^2}{t^2}\right)+u_{1,x}+w_{,z}=0 \tag{2.4}$$

Integration through the thickness of the elastomer from $z=-t/2$ to $z=t/2$ leads to

$$u_{0,x}+\frac{3}{2}u_{1,x}=\frac{3}{2}\varepsilon_c \tag{2.5}$$

in which ε_c is the nominal compression strain defined as

$$\varepsilon_c=-\frac{w\left(\frac{t}{2}\right)-w\left(\frac{-t}{2}\right)}{t} \tag{2.6}$$

The stress state in the elastomer is assumed to be dominated by the internal pressure p, such that the normal stress components τ_{xx} and τ_{zz} are assumed as

$$\tau_{xx}\approx\tau_{zz}\approx-p \tag{2.7}$$

Under these stress assumptions, the equilibrium equation of the elastomer in the x-direction

$$\tau_{xx,x}+\tau_{xz,z}=0 \tag{2.8}$$

is reduced to

$$-p_{,x}+\tau_{xz,z}=0 \tag{2.9}$$

The assumption of linearly elastic behavior for the elastomer means that

$$\tau_{xz}=G\left(u_{,z}+w_{,x}\right) \tag{2.10}$$

with G being the shear modulus of the elastomer. Using the displacement assumptions in Equations (2.1) and (2.2), the above equation becomes

$$\tau_{xz}=-8Gu_0\frac{z}{t^2} \tag{2.11}$$

which gives, from Equation (2.9),

$$p_{,x}=-\frac{8G}{t^2}u_0 \tag{2.12}$$

Differentiating the above equation with respect to x and then combining the result with Equation (2.5) to eliminate the term of $u_{0,x}$, we have

$$p_{,xx}=\frac{12G}{t^2}\left(u_{1,x}-\varepsilon_c\right) \tag{2.13}$$

2.1.2 Equilibrium in Reinforcing Sheet

The deformation of the elastomeric layers bonded to the top and bottom surfaces of the reinforcing sheet generates the bonding shear stresses σ_{xz} on the surfaces of the reinforcing sheet, as shown in Figure 2.2.

In an infinitesimal dx width of the reinforcing sheet, the internal normal farce per unit length in the x-direction, F, is related to these bonding shear stresses through the equilibrium equation

$$dF_{,x}+\left(\sigma_{xz}\big|_{z=-\frac{t}{2}}-\sigma_{xz}\big|_{z=\frac{t}{2}}\right)=0 \tag{2.14}$$

The shear stresses acting on the top and bottom surfaces of the reinforcing sheet can be derived from Equation (2.11)

$$\sigma_{xz}\big|_{z=-\frac{t}{2}}=\frac{8G}{2t}u_0\ ;\ \sigma_{xz}\big|_{z=\frac{t}{2}}=-\frac{8G}{2t}u_0 \tag{2.15}$$

Substitution of these into Equation (2.14) gives

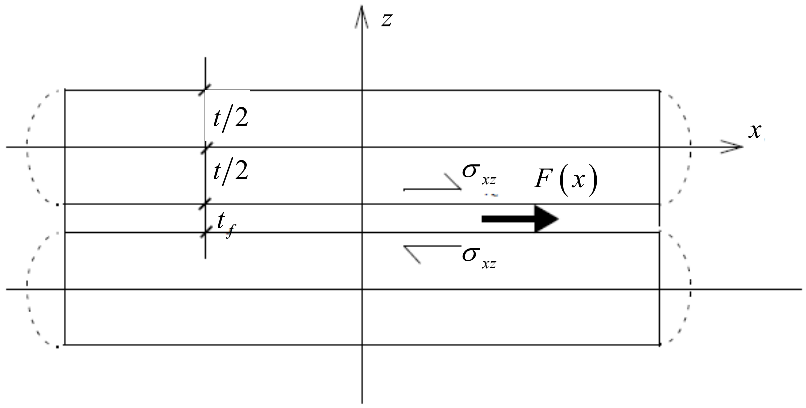

Figure 2.2 Forces in reinforcing sheet bonded to layers of elastomers.

$$F_{,x} = -\frac{8G}{t} u_0 \tag{2.16}$$

The displacement in the reinforcement is related to the internal normal forces through the linearly elastic strain-stress relation such that

$$\varepsilon_f = u_{1,x} = \frac{F}{E_f t_f} \tag{2.17}$$

where E_f is the elastic modulus of the reinforcement, and F is the internal normal force per unit length in the y-direction. Combined with Equation (2.16) gives

$$u_{1,xx} = -\frac{8G}{E_f t_f t} u_0 \tag{2.18}$$

The complete system of equations is

$$p_{,x} = -\frac{8Gu_0}{t^2} \tag{2.19}$$

$$u_{0,x} + \frac{3}{2} u_{1,x} = \frac{3\Delta}{2t} \tag{2.20}$$

$$u_{1,xx} = -\frac{8G}{E_f t_f t} u_o \tag{2.21}$$

With boundary conditions or symmetric conditions as follows:

$$u_0(0) = 0 \tag{2.22}$$

$$u_1(0) = 0 \tag{2.23}$$

$$\tau_{xx}\left(\pm b\right)=0 \tag{2.24}$$

$$F\left(\pm b\right)=0 \tag{2.25}$$

Combining Equation (2.20) and Equation (2.21) to eliminate u_0, gives

$$u_{1,xxx}=-\frac{12G}{E_f t_f t} \qquad u_{1,x}=-\frac{12G}{E_f t_f t}\frac{\Delta}{t} \tag{2.26}$$

We define

$$\alpha=\sqrt{\frac{12Gb^2}{E_f t_f t}} \tag{2.27}$$

Leading to

$$\frac{2}{3}u_1=A+B\cosh\alpha x/b+C\sinh\alpha x/b+\frac{\Delta}{t}x \tag{2.28}$$

Symmetry suggests that $A=0$, $B=0$, giving

$$u_1=C\sinh\alpha x/b+\frac{\Delta}{t}x \tag{2.29}$$

From Equation (2.17) we have

$$F=E_f t_f u_{1,x}=E_f t_f\left(\frac{\alpha}{b}C\cosh\alpha x/b+\frac{\Delta}{t}\right) \tag{2.30}$$

which with $F=0$ on $x=\pm b$ leads to

$$F\left(x\right)=\frac{\Delta}{t}E_f t_f\left(1-\frac{\cosh\alpha x/b}{\cosh\alpha}\right) \tag{2.31}$$

The displacements pattern for the reinforcement and the force in the reinforcement for various values of α from $\alpha=0$, corresponding to $E_f=\infty$ (the steel pressure solution), to $\alpha=3$, corresponding to very flexible reinforcement are shown in Figure 2.3 and Figure 2.4. As the reinforcement becomes more flexible, the displacement tends to almost linear in x and the force is almost constant.

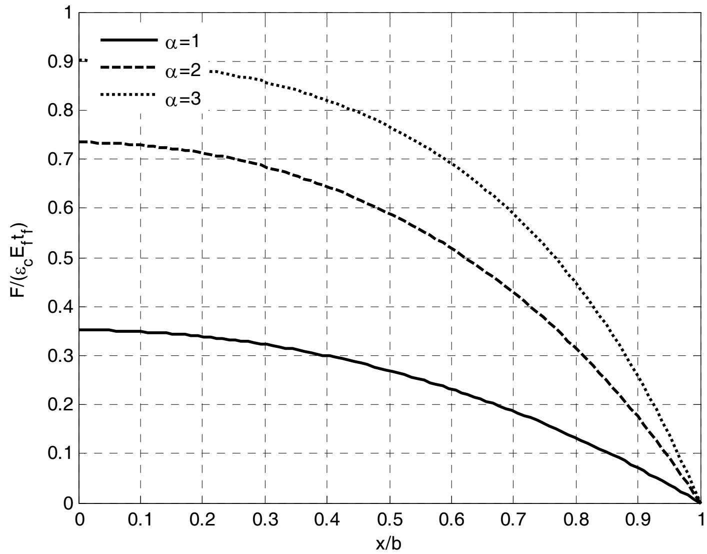

Figure 2.3 Normalized force pattern in reinforcement.

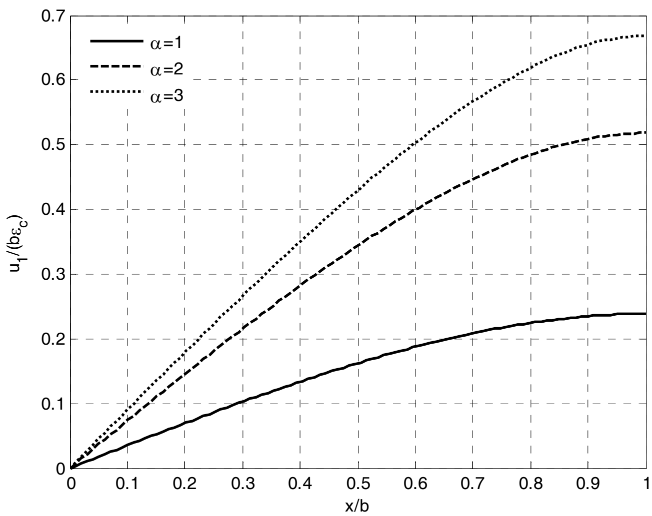

Figure 2.4 Displacement pattern for fiber reinforcement for various values of α .

2.1.3 Solution of Pressure and Effective Compressive Modulus

Equation (2.30) with $F = 0$ on $x = \pm b$ leads to

$$u_1(x) = \frac{\Delta}{t}\left(x - \frac{b \sinh \alpha x/b}{\alpha \cosh \alpha}\right) \tag{2.32}$$

$$u_0(x) = \frac{3}{2}\frac{\Delta}{t}\frac{b \sinh \alpha x/b}{\alpha \cosh \alpha} \tag{2.33}$$

Also, using Equation (2.13) and the boundary condition $\tau_{xx} = 0$ at $x = \pm b$ gives

$$p = \frac{\Delta}{t}\frac{E_f t_f}{t}\left(1 - \frac{\cosh \alpha x/b}{\cosh \alpha}\right) \tag{2.34}$$

The load per unit length of the strip, P, is given by

$$P = \frac{E_f t_f}{t} 2\int_0^b \left(1 - \frac{\cosh \alpha x/b}{\cosh \alpha}\right) dx \frac{\Delta}{t} = \frac{2E_f t_f}{\alpha t} b\left(\alpha - \tanh \alpha\right)\frac{\Delta}{t} \tag{2.35}$$

This result can be interpreted as an effective compression modulus, E_c, given by

$$E_c = \frac{P}{A}\frac{t}{\Delta} = \frac{E_f t_f}{t}\left(1 - \frac{\tanh \alpha}{\alpha}\right) \tag{2.36}$$

We note that when $\alpha \to 0$, i.e., $E_f \to \infty$, we have $E_c \to 4GS^2$ as for rigid reinforced bearing. The formula also shows that $E_c < 4GS^2$ for all finite values of E_f.

The effect of the elasticity of the reinforcement on the various quantities of interest can be illustrated by a few examples. We normalize the compression modulus, E_c, by dividing by $4GS^2$, giving from Equation (2.36)

$$\frac{E_c}{4GS^2} = \frac{3}{\alpha^2}\left(1 - \frac{\tanh \alpha}{\alpha}\right) \tag{2.37}$$

which is shown in Figure 2.5 for $0 \le \alpha \le 5$; note how the stiffness decreases with decreasing E_f. The distribution of the pressure for various values from $\alpha = 0$, corresponding to $E_f = \infty$ (the steel pressure solution), to $\alpha = 3$, corresponding to very flexible reinforcement is shown in Figure 2.5.

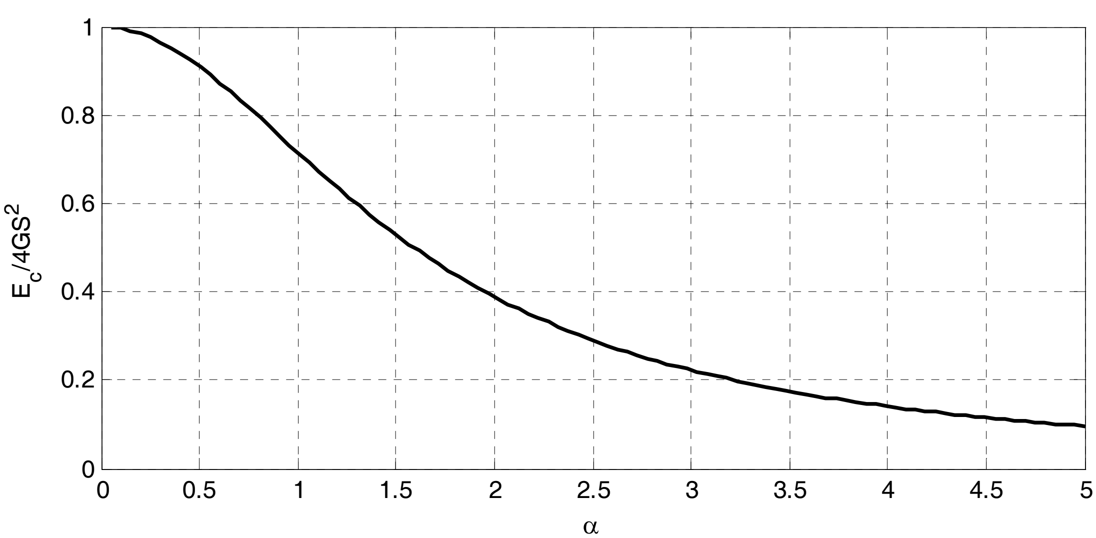

Figure 2.5 Variation of effective compression modulus with αb in infinitely long strip pad.

2.1.4 Flexible Reinforcement and Compressibility

In cases of large shape factors, to estimate E_c including compressibility in a manner consistent with the assumptions of the previous analysis, the equation of incompressibility is replaced by

$$\varepsilon_{xx} + \varepsilon_{zz} = -\frac{p}{K} \tag{2.38}$$

where K is the bulk modulus. Integration through the thickness leads to

$$\frac{2}{3}u_{0,x} + u_{1,x} + \frac{p}{K} = \varepsilon_c \tag{2.39}$$

This is then supplemented by the same equation of stress equilibrium and by the equation for the forces in the reinforcement. The system of equation for the combined effects of reinforcement flexibility and compressibility is now

$$p_{,x} = -\frac{8Gu_0}{t^2} \tag{2.40}$$

$$u_{1,xx} = -\frac{8Gu_0}{E_f t_f t} \tag{2.41}$$

$$\frac{2}{3}u_{0,x} + u_{1,x} + \frac{p}{K} = \varepsilon_c \tag{2.42}$$

Two dimensionless parameters, $\alpha = \sqrt{12Gb^2 / E_f t_f t}$ and $\beta = \sqrt{12Gb^2 / Kt^2}$, determine the comparative significance of flexibility in the reinforcement and compressibility in the elastomer.

In terms of α and β, Equation 2.40 and Equation 2.41 become

$$\left(\frac{p}{K}\right)_{,x} = \frac{2}{3}\beta^2 u_0 b^2 \tag{2.43}$$

$$u_{1,xx} = -\frac{2}{3}\alpha^2 u_0 \Big/ b^2 \tag{2.44}$$

Differentiation of Equation 2.42 once and substitution of p and u_1 from Equations 2.43 and 2.44 gives

$$u_{0,xx} - \frac{\left(\alpha^2 + \beta^2\right)}{b^2} u_0 = 0 \tag{2.45}$$

from which we have

$$u_0 = A\cosh \lambda x/b + B\sinh \lambda x/b \tag{2.46}$$

where

$$\lambda^2 = \alpha^2 + \beta^2 \tag{2.47}$$

In turn, using Equation 2.40 and Equation 2.41 gives solution for p and u_1 in the forms

$$u_1 = -\frac{2}{3}\frac{\alpha^2}{\lambda^2} A\cosh \lambda x/b + -\frac{2}{3}\frac{\alpha^2}{\lambda^2} B\sinh \lambda x/b + C_1 x + D \tag{2.48}$$

and

$$\frac{p}{K} = -\frac{2}{3}\frac{\beta^2}{\lambda b} A\sinh \lambda x/b + -\frac{2}{3}\frac{\beta^2}{\lambda b} B\cosh \lambda x/b + C_2 \tag{2.49}$$

The constants of integration are, of course, not independent of each other but are related through the basic equations. Substitution of three solutions into Equation 2.49 gives

$$\begin{gathered}\frac{2}{3}\frac{\lambda}{b}\left(A\sinh \lambda x/b + B\cosh \lambda x/b\right) - \frac{2}{3}\frac{\alpha^2}{\lambda b}\left(A\sinh \lambda x/b + B\cosh \lambda x/b\right) + \\ C_1 - \frac{2}{3}\frac{\beta^2}{\lambda}\left(A\sinh \lambda x/b + B\cosh \lambda x/b\right) + C_2 = \varepsilon_c\end{gathered} \tag{2.50}$$

The coefficients of $\sinh \beta x/b$ and $\cosh \beta x/b$ vanish and the result is $C_1 + C_2 = \varepsilon_c$.

For the particular problem of the compression of the strip it is convenient to use the symmetry of the solutions. Thus u_0 and u_1 are anti-symmetric and p is symmetric on $-b \le x \le +b$. It follows that $A = 0$ and $D = 0$ giving

$$u_0 = B\sinh \lambda x/b \tag{2.51}$$

$$u_1 = -\frac{2}{3}\frac{\alpha^2}{\lambda^2} B\sin \lambda x/b + C_1 x \tag{2.52}$$

$$\frac{p}{K} = -\frac{2}{3}\frac{\beta^2}{\lambda b} B\cosh \lambda x/b + \varepsilon_c - C_1 \tag{2.53}$$

The boundary conditions for B and C_1 are that the pressure p at the edges $x = \pm b$ is zero and that the stress in the reinforcement $E_f u_{1,x}$ also vanishes at the edges. Thus

$$-\frac{2}{3}\frac{\alpha^2}{\lambda b} B\cos \lambda + C_1 = 0 \tag{2.54}$$

$$-\frac{2}{3}\frac{\beta^2}{\lambda b} B\cosh \lambda - C_1 = -\varepsilon_c \tag{2.55}$$

giving

$$B = \frac{3}{2}\frac{\lambda}{\alpha^2+\beta^2} b \frac{1}{\cosh\lambda}\varepsilon_c \tag{2.56}$$

$$C_1 = \frac{\alpha^2}{\alpha^2+\beta^2}\varepsilon_c \tag{2.57}$$

and the solution becomes

$$u_0 = \frac{3}{2} b \frac{\sinh \lambda x/b}{\alpha \cosh\lambda}\varepsilon_c \tag{2.58}$$

$$u_1 = b\frac{\alpha^2}{\alpha^2+\beta^2}\left(\frac{x}{b} - \frac{\sinh\lambda x/b}{\lambda\cosh\lambda}\right)\varepsilon_c \tag{2.59}$$

and

$$\frac{p}{K} = \frac{\beta^2}{\alpha^2+\beta^2}\left(1-\frac{\cosh\lambda x/b}{\cosh\lambda}\right)\varepsilon_c \tag{2.60}$$

Integration of p from Equation 2.60 gives

$$E_c = K\frac{\beta^2}{\alpha^2+\beta^2}\left(1-\frac{\tanh\lambda}{\lambda}\right) \tag{2.61}$$

If the effect of compressibility is negligible, then $\beta \to 0$ and $\lambda = \alpha$, and we have

$$K\beta^2 = \frac{12Gb^2}{t^2} \tag{2.62}$$

giving

$$E_c = \frac{E_f t_f}{t}\left(1-\frac{\tanh\alpha}{\alpha}\right) \tag{2.63}$$

which is the same as the result in the previous section. On the other hand, if the flexibility of the reinforcement is negligible, then $\alpha \to 0$ and $\lambda \to \beta$, giving

$$E_c = K\left(1-\frac{\tanh\beta}{\beta}\right) \tag{2.64}$$

If the compression modulus is normalized by $4GS^2$, then from Equation (2.63) we have

$$\frac{E_c}{4GS^2} = \frac{3}{\alpha^2+\beta^2}\left(1-\frac{\tanh\left(\alpha^2+\beta^2\right)^{1/2}}{\left(\alpha^2+\beta^2\right)^{1/2}}\right) \tag{2.65}$$

which demonstrates that the vertical stiffness is reduced by both compressibility in the elastomer and flexibility in the reinforcement. Figure 2.6 shows the variation of normalized effective compression modulus with α and β, and Figure 2.7 shows the variation of normalized effective compression modulus with β for various values of α, from $\alpha = 3$.

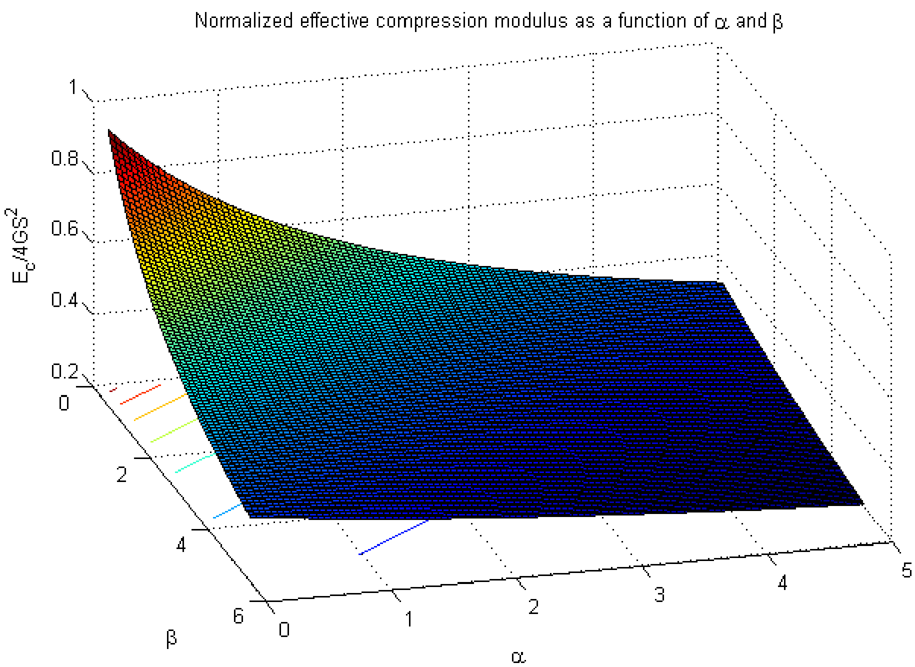

Figure 2.6 **Variation of normalized effective compression modulus with α and β, in an infinitely long strip pad.**

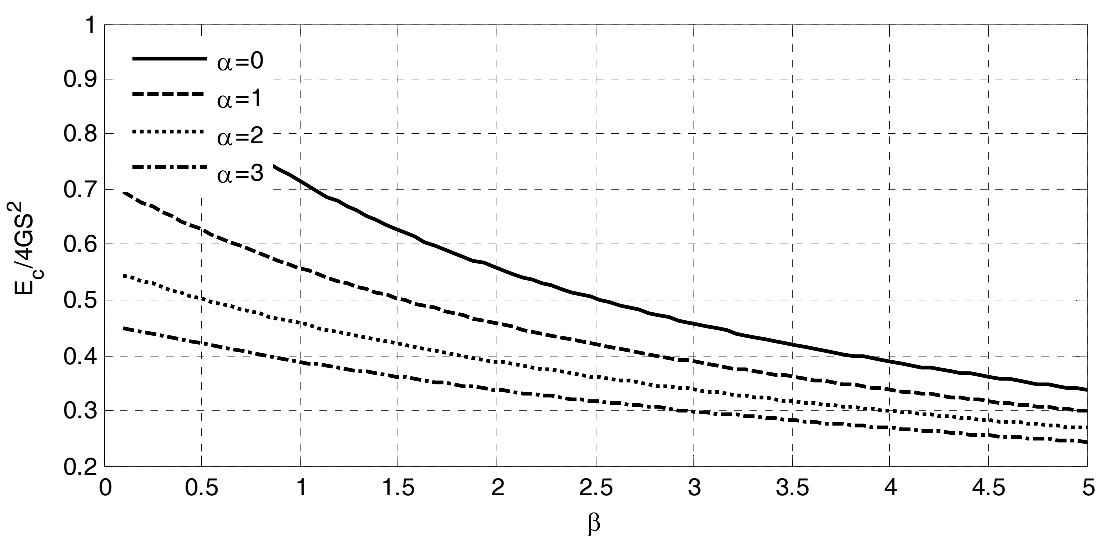

Figure 2.7 **Variation of normalized effective compression modulus with β for** $\alpha = 0 - 3.$

2.2 CIRCULAR PAD

2.2.1 Deformation of Pad under Compression

The circular pad shown in Figure 2.8 has a radius of R and a thickness of t, in which we locate a cylindrical coordinate system, (r,θ,z), in the middle surface of the pad. The displacements of the elastomer along the r - and z -directions, denoted as u_r, are assumed to have the forms:

$$u_r(r,z) = u_0(r)\left(1-\frac{4z^2}{t^2}\right)+u_1(r) \\ w(x,z) = w(z) \tag{2.66}$$

In the first equation, the term of u_0 represents the kinematic assumption of quadratically varied deformation of the vertical lines in the elastomer and is supplemented by additional displacement u_1 to accommodate the stretch of the reinforcement. The second equation represents the assumption that horizontal plane remain planar after deformation in the elastomer.

If the assumption of incompressibility were to be made, further constraint on the three components of strain, $\varepsilon_r, \varepsilon_\theta, \varepsilon_z$, in the form $\varepsilon_r + \varepsilon_\theta + \varepsilon_z = 0$ would be needed; but when the material is assumed to be compressible with bulk modulus K, this constraint is replaced by

$$\varepsilon_r + \varepsilon_\theta + \varepsilon_z = -\frac{p}{K} \tag{2.67}$$

where p is the pressure in the elastomer. The three normal strains are given by

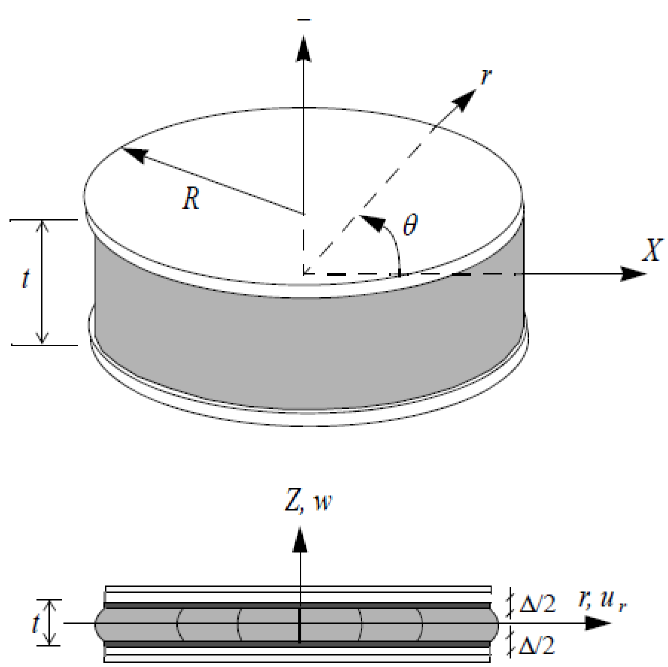

Figure 2.8 Coordinate system for a circular pad of radius *R*.

$$\varepsilon_r = \frac{du_r}{dr} = \frac{du_0}{dr}\left(1-\frac{4z^2}{t^2}\right)\frac{du_1}{dr}$$
$$\varepsilon_\theta = \frac{1}{r}u_r = \frac{1}{r}\left(1-\frac{4z^2}{t^2}\right)\frac{1}{r}u_1 \tag{2.68}$$
$$\varepsilon_z = \frac{dw}{dz}$$

leading to

$$\left(\frac{du_0}{dr}+\frac{1}{r}u_0\right)\left(1-\frac{4z^2}{t^2}\right)+\frac{du_1}{dr}+\frac{1}{r}u_1+\frac{dw}{dz} = -\frac{p}{K} \tag{2.69}$$

which, when integrated through the thickness with respect to z, leads to

$$\left(\frac{du_0}{dr}+\frac{1}{r}u_0\right)+\frac{3}{2}\left(\frac{du_1}{dr}+\frac{1}{r}u_1\right) = \frac{3\Delta}{2t}-\frac{3p}{2K} \tag{2.70}$$

The stress state is assumed to be dominated by the internal pressure, p, such that the normal stress components, $\sigma_r, \sigma_\theta, \sigma_z$, differ from $-p$ only by terms of order $\left(t^2/R^2\right)p$, i.e.,

$$\sigma_r \approx \sigma_\theta \approx \sigma_z \approx -p \tag{2.71}$$

The shear stress component, τ_{rz}, which is generated by the constraints at the top and bottom of the pad, is assumed to be of order $\left(t/R\right)p$.The equation of stress equilibrium in the rubber along the radial direction

$$\frac{d\sigma_r}{dr}+\frac{d\tau_{rz}}{dz}+\frac{\sigma_r-\sigma_\theta}{r} = 0 \tag{2.72}$$

reduces under these assumptions to

$$\frac{d\tau_{rz}}{dz} = \frac{dp}{dr} \tag{2.73}$$

The assumption of elastic behavior means that

$$\tau_{rz} = G\gamma_{rz} \tag{2.74}$$

in which G is the shear modulus of the rubber and γ_{rz} is the shear strain with

$$\gamma_{rz} = -\frac{8z}{t^2}u_0 \tag{2.75}$$

These give

$$\frac{dp}{dr} = -\frac{8Gu_0}{t^2} \tag{2.76}$$

The internal forces per unit length in the reinforcing sheet are denoted by N_r in the radial r-direction and in the tangential direction. If the sheet is made of fiber reinforcement, the individual fibers are replaced by an equivalent sheet of reinforcement of thickness t_f. As shown in Figure 2.2, the internal forces of the equivalent reinforcing sheet are related to the shear stresses on the top and bottom of the pad through the equilibrium equation

$$\frac{dN_r}{dr} + \frac{N_r - N_\theta}{r} - \tau_{rz}\big|_{z=\frac{t}{2}} + \tau_{rz}\big|_{z=-\frac{t}{2}} = 0 \tag{2.77}$$

From Equations (2.74) and (2.75) we have

$$\tau_{rz}\big|_{z=\frac{t}{2}} = -\frac{8Gu_0}{2t}; \tau_{rz}\big|_{z=-\frac{t}{2}} = \frac{8Gu_0}{2t} \tag{2.78}$$

Giving

$$\frac{dN_r}{dr} + \frac{N_r - N_\theta}{r} = -\frac{8Gu_0}{t} \tag{2.79}$$

The extensional strains in the reinforcement are

$$\varepsilon_r^f = \frac{du_1}{dr}; \varepsilon_\theta^f = \frac{1}{r}u_1 \tag{2.80}$$

which are related to the internal forces through the elastic modulus E_f and Poisson's ratio ν of the equivalent sheet and its thickness t_f such that

$$\varepsilon_r^f = \frac{N_r - \nu N_\theta}{E_f t_f}; \varepsilon_\theta^f = \frac{-\nu N_r + N_\theta}{E_f t_f} \tag{2.81}$$

And by inversion

$$N_r = \frac{E_f t_f}{1-\nu^2}\left(\varepsilon_r^f + \nu\varepsilon_\theta^f\right); N_\theta = \frac{E_f t_f}{1-\nu^2}\left(\nu\varepsilon_r^f + \varepsilon_\theta^f\right) \tag{2.82}$$

Substitution of these relationships into the equation of equilibrium for the reinforcement, Equation (2.79), gives

$$u_0 = -\frac{E_f t_f t}{8\left(1-\nu^2\right)G}\left[\frac{d^2u_1}{dr^2} + \nu\frac{d}{dr}\left(\frac{u_1}{r}\right) + \left(1-\nu\right)\frac{1}{r}\frac{du_1}{dr} - \left(1-\nu\right)\frac{u_1}{r^2}\right] \tag{2.83}$$

which reduces to

$$u_0 = -\frac{3R^2}{2\alpha^2}\left(\frac{d^2u_1}{dr^2} + \frac{1}{r}\frac{du_1}{dr} - \frac{u_1}{r^2}\right) = -\frac{3R^2}{2\alpha^2}\left(\frac{d}{dr}\left(\frac{du_1}{dr} + \frac{1}{r}u_1\right)\right) \tag{2.84}$$

in which we define a non-dimensional parameter α by

$$\alpha^2 = \frac{12\left(1-\nu^2\right)GR^2}{E_f t_f t} \tag{2.85}$$

A second non-dimensional parameter β is defined as

$$\beta^2 = \frac{12GR^2}{Kt^2} \tag{2.86}$$

in terms of which the equilibrium equation of the elastomer can be written as

$$\frac{d\left(p/K\right)}{dr} = -\frac{2\beta^2 u_0}{3R^2} \tag{2.87}$$

It is convenient at this point to collect together the three equations for the three unknown functions u_0, u_1, and p in the form,

$$\frac{d\left(p/K\right)}{dr} = -\frac{2\beta^2 u_0}{3R^2} \tag{2.88}$$

$$\frac{d}{dr}\left(\frac{du_1}{dr} + \frac{1}{r}u_1\right) = -\frac{2\alpha^2 u_0}{3R^2} \tag{2.89}$$

$$\frac{2}{3}\left(\frac{du_0}{dr} + \frac{1}{r}u_0\right) + \left(\frac{du_1}{dr} + \frac{1}{r}u_1\right) = \frac{\Delta}{t} - \frac{p}{K} \tag{2.90}$$

Differentiation of the third equation and substitution of p and u_1 from the first and second equation leads to

$$\frac{2}{3}\left(\frac{du_0}{dr} + \frac{1}{r}u_0\right) - \frac{\alpha^2 + \beta^2}{R^2}u_0 = 0 \tag{2.91}$$

It is now clear why the two apparently unrelated effects of stretching of the reinforcement and compressibility of the elastomer affect the solution in the same way: the parameter α solely determines the effect of stretching and β that of compressibility. At this point it is convenient to define another parameter λ through

$$\lambda^2 = \alpha^2 + \beta^2 \tag{2.92}$$

The solution of Equation (2.91) is

$$u_0(r) = AI_1(\lambda(r/R)) + BK_1(\lambda(r/R)) \tag{2.93}$$

where A and B are constants of integration and I_n, K_n are modified Bessel functions of the first and second kind of order n. In turn, substitution of this into the first two equations provides the solutions for p and u_1 in the forms

$$p/K = -\frac{2\beta^2}{3\lambda R}\left(AI_0(\lambda(r/R)) - BK_0(\lambda(r/R))\right) + C_1 \tag{2.94}$$

and

$$u_1(r) = -\frac{2\alpha^2}{3\lambda^2}\left(AI_1(\lambda(r/R)) + BK_1(\lambda(r/R))\right) + \frac{C_2}{2}r + \frac{D}{r} \tag{2.95}$$

The constants of integration A, B, C_1, C_2, and D are not independent but are related through the compressibility constraint equation. Substitution of the three solutions into Equation (2.70) gives

$$\begin{aligned}
&\frac{2}{3}\left[\frac{1}{r}\frac{d}{dr}\left(ArI_1(\lambda(r/R)) + BrK_1(\lambda(r/R))\right)\right] + \\
&-\frac{2\alpha^2}{3\lambda^2}\left[\frac{1}{r}\frac{d}{dr}\left(ArI_1(\lambda(r/R)) + BrK_1(\lambda(r/R))\right)\right] - \\
&+\left[\frac{1}{r}\frac{d}{dr}\left(\frac{C_2r^2}{2} + D\right)\right] - \frac{2\beta^2}{3\lambda R}\left[\left(AI_0(\lambda(r/R)) + BK_0(\lambda(r/R))\right)\right] + C_1 = \varepsilon_c
\end{aligned} \tag{2.96}$$

The first expression becomes

$$\begin{aligned}
&\frac{2}{3}\left[\frac{1}{r}\frac{d}{dr}\left(ArI_1(\lambda r/R) + BrK_1(\lambda r/R)\right)\right] = \\
&\frac{2A}{3r}\left[I_1(\lambda r/R) + \frac{r\lambda}{R}I_0(\lambda r/R) - r\left(\frac{R}{\lambda r}\right)I_1(\lambda r/R)\right] - \\
&+\frac{2B}{3r}\left[K_1(\lambda r/R) + \frac{r\lambda}{R}K_0(\lambda r/R)\left(-r\left(\frac{R}{\lambda r}\right)K_1(\lambda r/R)\right)\right] \\
&= \frac{2}{3}A\frac{\lambda}{R}I_0(\lambda r/R) + \frac{2}{3}B\frac{\lambda}{R}K_0(\lambda r/R)
\end{aligned} \tag{2.97}$$

The second term becomes by the same process

$$-\frac{2\alpha^2}{3\lambda^2}\left[A\frac{\lambda}{R}I_0(\lambda r/R) + B\frac{\lambda}{R}K_0(\lambda r/R)\right] + C_1 + 0 \tag{2.98}$$

which with

$$p/K = -\frac{2\beta^2}{3\lambda R}\left(AI_0(\lambda(r/R)) + BK_0(\lambda(r/R))\right) + C_1 \tag{2.99}$$

leads to the result that the terms multiplied by A and B both vanish, D drops out, and we find

$$C_1 + C_2 = \varepsilon_c \tag{2.100}$$

If the pad is annular, $a \le r \le b$, then there are four boundary conditions for the four constants A, B, C_1, and D namely,

$$\begin{aligned} N_r(a) &= 0 \quad N_r(b) = 0 \\ p(a) &= 0 \quad p(b) = 0 \end{aligned} \tag{2.101}$$

If the pad is a complete circle of radius R, i.e., $0 \le r \le R$, we have $N_r(R) = 0$ and $p(R) = 0$, and boundedness of u_1 and p at $r = 0$. In fact, by the assumption of radial symmetry, $u_1(0) = 0$.

Since $t_f = 0.07$ mm and $K_1(x) \to \ln\frac{1(2)}{x}$ as $x \to 0$, we must have $B = 0$ and $D = 0$. With these simplifications the solutions for the complete circular pad become

$$u_0(r) = AI_1\left(\lambda(r/R)\right) \tag{2.102}$$

$$p/K = -\frac{2\beta^2}{3\lambda R}\left(AI_0\left(\lambda(r/R)\right)\right) + C_1 \tag{2.103}$$

$$u_1(r) = -\frac{2\alpha^2}{3\lambda^2}\left(AI_1\left(\lambda(r/R)\right)\right) + \frac{\varepsilon_c - C_1}{2} r \tag{2.104}$$

The condition that the pressure is zero at the boundary $r = R$ means that $C_1 = \frac{2\beta^2}{3\lambda R} AI_0(\lambda)$; thus the pressure is given by

$$p/K = \frac{2\beta^2}{3\lambda R} A\left(I_0(\lambda) - I_0\left(\lambda(r/R)\right)\right) \tag{2.105}$$

The remaining constant of integration must be determined from the requirement that the radial stress in the reinforcement is zero at the edge, $r = R$. From Equation (2.81) we have

$$\begin{aligned} \varepsilon_r^f &= -\frac{2\alpha^2}{3\lambda R} A\left[I_0\left(\lambda(r/R)\right) - \frac{1}{\lambda(r/R)} I_1\left(\lambda(r/R)\right)\right] + \frac{1}{2}(\varepsilon_c - C_1) \\ \varepsilon_\theta^f &= -\frac{2\alpha^2}{3\lambda R} A\left[\frac{1}{\lambda(r/R)} I_1\left(\lambda(r/R)\right)\right] + \frac{1}{2}(\varepsilon_c - C_1) \end{aligned} \tag{2.106}$$

Thus

$$N_r(r)=\frac{E_f t_f}{1-\nu^2}\left\{-\frac{2\alpha^2}{3\lambda R}A\left[I_0\left(\lambda(r/R)\right)-\frac{1-\nu}{\lambda(r/R)}I_1\left(\lambda(r/R)\right)\right]+(1+\nu)\frac{1}{2}(\varepsilon_c-C_1)\right\}$$
$$N_\theta(r)=\frac{E_f t_f}{1-\nu^2}\left\{-\frac{2\alpha^2}{3\lambda R}A\left[\nu I_0\left(\lambda(r/R)\right)+\frac{1-\nu}{\alpha R}I_1\left(\lambda(r/R)\right)\right]+(1+\nu)\frac{1}{2}(\varepsilon_c-C_1)\right\}$$

(2.107)

The requirement that $N_r(R)=0$ means

$$-\frac{2\alpha^2}{3\lambda R}A\left[I_0(\lambda)-\frac{1-\nu}{\lambda}I_1(\lambda)\right]-\frac{2\beta^2}{3\lambda R}\frac{1+\nu}{2}AI_0(\lambda)=-(1+\nu)\frac{1}{2}\varepsilon_c \tag{2.108}$$

leading to

$$A=\frac{\varepsilon_c(1+\nu)}{2}\left\{\frac{1}{\frac{2\alpha^2}{3\lambda R}\left[I_0(\lambda)-\frac{1-\nu}{\lambda}I_1(\lambda)\right]+\frac{2\beta^2}{3\lambda R}\frac{1+\nu}{2}I_0(\lambda)}\right\} \tag{2.109}$$

$$u_1(r)=\frac{\Delta}{2t}\left\{r-\frac{(1+\nu)I_1(\alpha r)}{\alpha\left[I_0(\alpha r)-\frac{1-\nu}{\alpha r}I_1(\alpha r)\right]}\right\} \tag{2.110}$$

$$N_r(r)=\frac{E_f t_f}{2(1-\nu)}\frac{\Delta}{t}\left[1-\frac{I_0(\alpha r)-\frac{1-\nu}{\alpha r}I_1(\alpha r)}{I_0(\alpha R)-\frac{1-\nu}{\alpha R}I_1(\alpha R)}\right] \tag{2.111}$$

$$N_\theta(r)=\frac{E_f t_f}{2(1-\nu)}\frac{\Delta}{t}\left[1-\frac{\nu I_0(\alpha r)+\frac{1-\nu}{\alpha r}I_1(\alpha r)}{I_0(\alpha R)-\frac{1-\nu}{\alpha R}I_1(\alpha R)}\right] \tag{2.112}$$

2.2.2 Compression Stiffness and Pressure Distribution

The vertical stiffness of a rubber bearing is given by the formula

$$K_V=\frac{E_c A}{t_r} \tag{2.113}$$

where A is the area of the bearing, t_r is the total thickness of rubber in the bearing, and E_c is the instantaneous compression modulus of the rubber-steel composite under the specified level of vertical load. The value of E_c for a single rubber layer is controlled by the shape factor, S, defined as S = the loaded area/free area, which is a dimensionless measure of the aspect ratio of the single layer of the elastomer. For a circular pad of radius R and thickness t,

$$S = \frac{R}{2t} \tag{2.114}$$

To determine the compression modulus, E_c, we integrate p over area to determine the resultant normal load, P; E_c is then given by

$$E_c = P/A\varepsilon_c \tag{2.115}$$

where $A = \pi R^2$ is the area of the pad and $\varepsilon_c = \Delta/t$ is the compression strain.

The total axial load P is

$$P = 2\pi \int_0^R p(r) r dr \tag{2.116}$$

where $p(r)$ from Equation (2.103) can be written as

$$p = \frac{8GR}{\lambda t^2} A\left(I_0(\lambda) - I_0\left(\lambda(r/R)\right)\right) \tag{2.117}$$

which with Equation (2.104) becomes

$$P = \pi \frac{8GR^3 A}{\lambda t^2}\left[I_0(\lambda) - \frac{2}{\lambda} I_1(\lambda)\right] \tag{2.118}$$

which, when A is substituted from Equation (2.98), becomes

$$P = \pi R^2 \frac{8G}{\lambda t^2} \frac{\left[I_0(\lambda) - \frac{2}{\lambda} I_1(\lambda)\right]}{\frac{2\alpha^2}{3\lambda R}\left[I_0(\lambda) - \frac{1-\nu}{\lambda} I_1(\lambda)\right] + \frac{2\beta^2}{3\lambda R}\frac{1+\nu}{2} I_0(\lambda)} \frac{\varepsilon_c(1+\nu)}{2} \tag{2.119}$$

Using Equation (2.115), we have

$$E_c = 24GS^2(1+\nu) \frac{\left[I_0(\lambda) - \frac{2}{\lambda} I_1(\lambda)\right]}{\alpha^2\left[I_0(\lambda) - \frac{1-\nu}{\lambda} I_1(\lambda)\right] + \beta^2 \frac{1+\nu}{2} I_0(\lambda)} \tag{2.120}$$

In order to confirm the accuracy of this result it is useful to examine number of special cases. First assume $K \to \infty$ and $\beta \to \infty$ in which $\lambda = \alpha$ and the compression modulus is

$$E_c = 24GS^2(1+\nu)\frac{\left[I_0(\alpha)-\frac{2}{\alpha}I_1(\alpha)\right]}{\alpha^2\left[I_0(\alpha)-\frac{1-\alpha}{\alpha}I_1(\alpha)\right]} \tag{2.121}$$

and the compression modulus is $\alpha \to \infty$ This reduces to $6GS^2$ independent of ν as it should. For the other special case where $E_f \to \infty$,, $\alpha^2 \to \infty$, and ν drops out, we have $\lambda = \beta$, and the compression modulus becomes

$$E_c = 48GS^2\frac{\left[I_0(\beta)-\frac{2}{\beta}I_1(\beta)\right]}{\beta^2 I_0(\beta)} \tag{2.122}$$

In the case where $\beta \to 0$, this tends to $6GS^2$ as before.

Figure 2.9 is a three-dimensional plot of the normalized effective modulus as a function of α and β. Plots of the full equation for varying α and for several values of β are shown in Figure 2.10. Figure 2.11 is a plot of the normalized effective modulus as a function of α for $\beta = 0$ and $\nu = 0;1/3$.

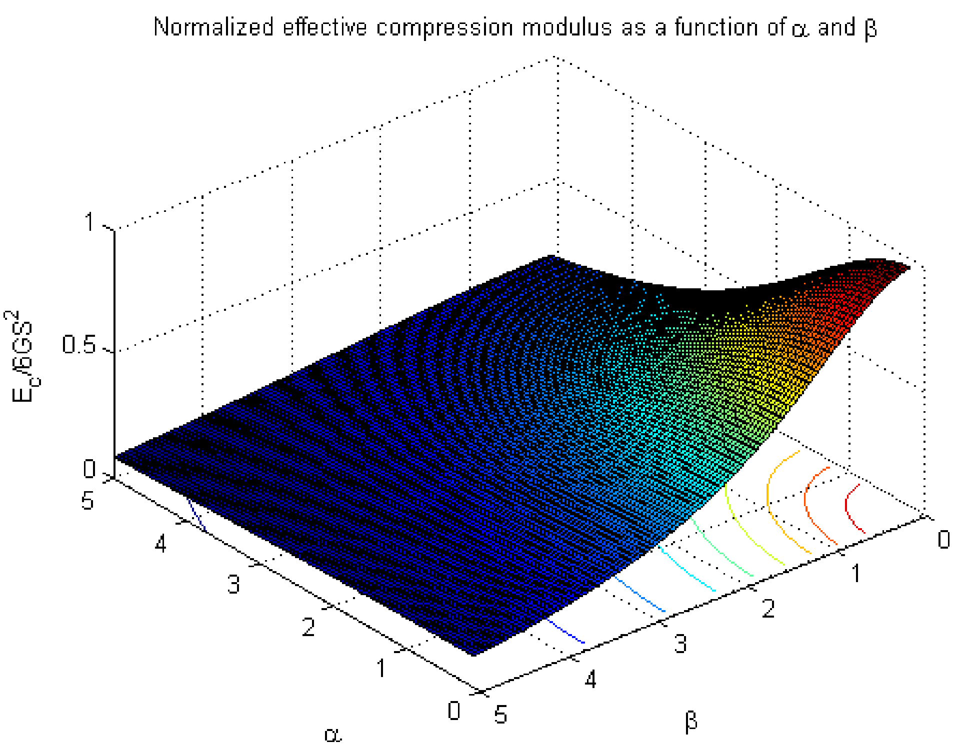

Figure 2.9 Normalized effective modulus as a function of α and β.

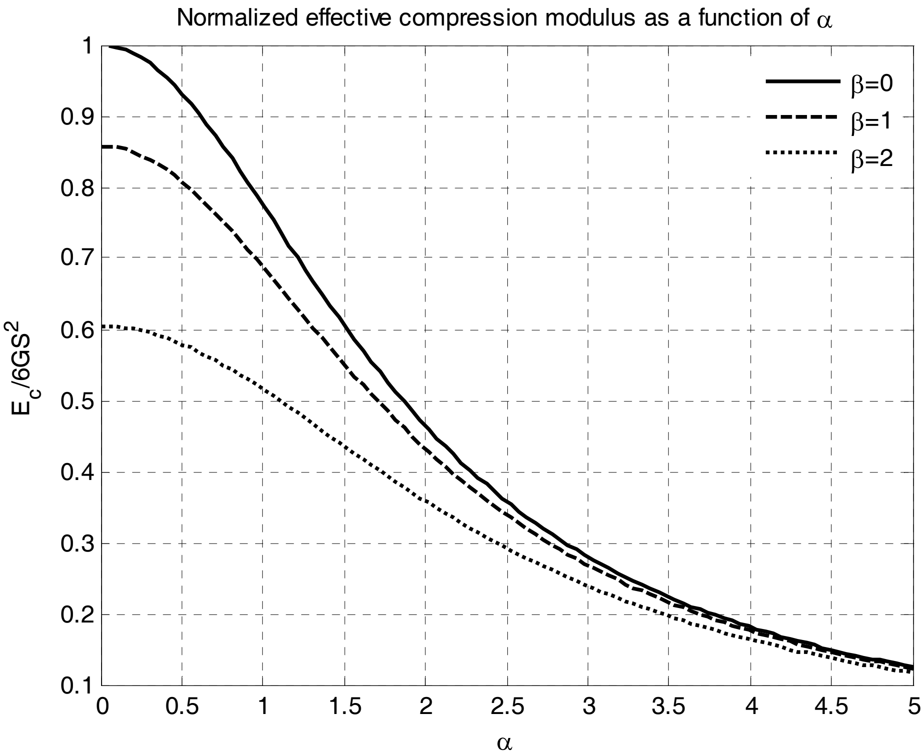

Figure 2.10 Normalized effective modulus as a function of α for different values of β.

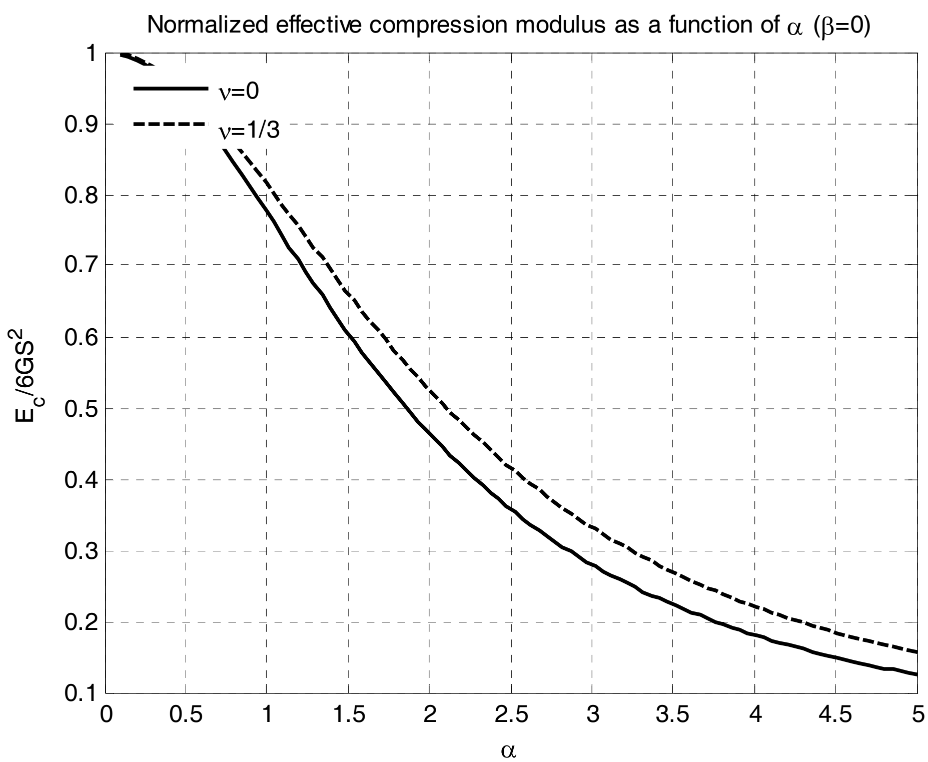

Figure 2.11 Normalized effective modulus as a function of $\alpha\left(\beta=0;\nu=0;1/3\right)$.

2.3 RECTANGULAR PAD

2.3.1 Equilibrium in Elastomeric Layer

A layer of elastomer in a rectangular isolator is shown in Figure 2.12. The elastomeric layer has a thickness of t. Its side length parallel to the x-axis is $2a$ and to the y-axis is $2b$. The elastomeric layer's top and bottom surfaces are perfectly bonded to flexible reinforcements that were modeled as an equivalent sheet of thickness t_f. Let u, v, and w denote the displacements of the elastomer in the x-, y-, and z-coordinate directions, respectively. In addition, u_1 and v_1 denote the displacements of the reinforcement in the x- and y-directions, respectively. Under the compression load P in the z-direction, the displacements of the elastomer are assumed to have the form

$$\begin{cases} u(x,y,z) = u_0(x,y)\left(1-\dfrac{4z^2}{t^2}\right)+u_1(x,y) \\ v(x,y,z) = v_0(x,y)\left(1-\dfrac{4z^2}{t^2}\right)+v_1(x,y) \\ w(x,y,z) = w(z) \end{cases} \tag{2.123}$$

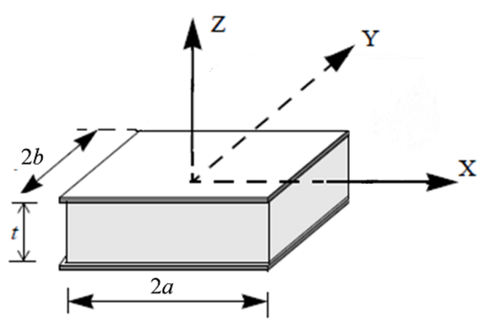

Figure 2.12 Reference system for a rectangular pad showing dimensions.

In Equation (2.123), the terms of u_0 and v_0 represent the kinematic assumption of quadratically varied displacements and are supplemented by additional displacements u_1 and v_1, respectively, which are constant through the thickness and are intended to accommodate the stretch of the reinforcement. The elastomer is assumed to have linearly elastic behavior with incompressibility. The assumption of incompressibility produces a constraint on displacements in the form

$$u_{,x} + v_{,y} + w_{,z} = 0 \tag{2.124}$$

where the commas imply partial differentiation with respect to the indicated coordinate. Substituting Equation (2.123) into the above equation and then taking integration through the thickness from $z=-t/2$ to $z=t/2$ lead to

$$\frac{2}{3}\left(u_{0,x}+v_{0,y}\right)+u_{1,x}+v_{1,y}=\varepsilon_c \tag{2.125}$$

in which $\varepsilon_c=\left[w(-t/2)-w(t/2)\right]/t$ is the nominal compression strain. The stress state in the elastomer is assumed to be dominated by the internal pressure, p, such that the stress components of the elastomer are [Kelly 1997]

$$\begin{aligned}&\sigma_{xx}\approx\sigma_{yy}\approx\sigma_{zz}\approx-p\\&\sigma_{xy}\approx 0\end{aligned} \tag{2.126}$$

The equilibrium equations in the x - and y -directions for the stresses of the elastomer are then reduced to

$$\begin{aligned}&-p_{,x}+\sigma_{xz,z}=0\\&-p_{,y}+\sigma_{yz,z}=0\end{aligned} \tag{2.127}$$

Using the displacement assumptions in Equation (2.123), the shear stress components of the elastomer become

$$\begin{aligned}&\sigma_{xz}=-\frac{8G}{t^2}u_0 z\\&\sigma_{yz}=-\frac{8G}{t^2}v_0 z\end{aligned} \tag{2.128}$$

with G being the shear modulus of the elastomer. Substitution of these into the equilibrium equations of Equation (2.127) leads to

$$\begin{aligned}&p_{,x}=-\frac{8G}{t^2}u_0\\&p_{,x}=-\frac{8G}{t^2}v_0\end{aligned} \tag{2.129}$$

Differentiating Equation (2.129) with respect to x and y, respectively, and then adding it up yields

$$p_{,xx}+p_{,yy}=-\frac{8G}{t^2}\left(u_{0,x}+v_{0,y}\right) \tag{2.130}$$

2.3.2 Equilibrium in Reinforcing Sheet

The internal forces acting in an infinitesimal dx by dy area of the reinforcing sheet are shown in Figure 2.13, where N_{xx} and N_{yy} are the normal forces per unit length in the x - and y -

directions, respectively, and N_{xy} the in-plane shear force per unit length. These internal forces are related to the shear stresses, σ_{xz} and σ_{yz}, on the surfaces of the reinforcing sheet bonded to the top and bottom layers of elastomer through two equilibrium equations in the x - and y - directions

$$dN_{xx}dy + dN_{xy}dx + (\sigma_{xz}\big|_{z=-t/2} - \sigma_{xz}\big|_{z=t/2})\, dxdy = 0 \tag{2.131}$$

$$dN_{yy}dy + dN_{xy}dy + (\sigma_{yz}\big|_{z=-t/2} - \sigma_{yz}\big|_{z=t/2})\, dxdy = 0 \tag{2.132}$$

Substituting Equation (2.128) into the above equations and then combining the results with the equilibrium equations of the elastomeric layer in Equation (2.129) to eliminate u_0 and v_0 lead to

$$\begin{aligned} N_{xx,x} + N_{xy,y} &= tp_{,x} \\ N_{yy,y} + N_{xy,x} &= tp_{,y} \end{aligned} \tag{2.133}$$

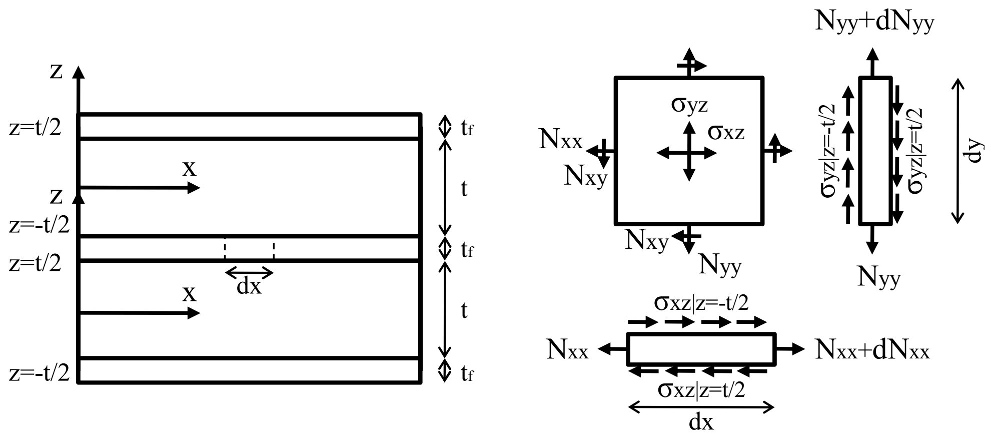

Figure 2.13 Forces in reinforcing sheet bonded to rectangular layers of elastomers.

The displacements in the reinforcement are related to the internal normal forces through the linearly elastic strain-stress relation such that

$$\begin{aligned} N_{xx} &= \frac{E_f t_f}{1-\nu^2}\left(u_{1,x} + \nu v_{1,y}\right) \\ N_{yy} &= \frac{E_f t_f}{1-\nu^2}\left(v_{1,y} + \nu u_{1,x}\right) \end{aligned} \tag{2.134}$$

where E_f and ν are the elastic modulus and Poisson's ratio of the reinforcement. The in-plane shear force has the following relation with the displacements:

$$N_{xy} = \frac{E_f t_f}{2(1+\nu)}\left(u_{1,y} + v_{1,x}\right) \tag{2.135}$$

Substitution of Equations (2.134) and (2.135) into Equation (2.133) leads to

$$u_{1,xx} + \nu v_{1,yx} + \frac{1-\nu}{2}\left(u_{1,yy} + v_{1,xy}\right) = \frac{\left(1-\nu^2\right)t}{E_f t_f} p_{,x} \tag{2.136}$$

$$v_{1,yy} + \nu u_{1,xy} + \frac{1-\nu}{2}\left(u_{1,yx} + v_{1,xx}\right) = \frac{\left(1-\nu^2\right)t}{E_f t_f} p_{,y} \tag{2.137}$$

Differentiating Equations (2.136) and (2.137) with respect to v and y, respectively, and adding them yields

$$q_{,xx} + q_{,yy} = \frac{\left(1-\nu^2\right)t}{E_f t_f}\left(p_{,xx} + p_{,yy}\right) \tag{2.138}$$

in which, for clarification, the term q is used to denote

$$q = u_{1,x} + v_{1,y} \tag{2.139}$$

Combining Equation (2.125) with Equation (2.130) to eliminate the terms of u_0 and v_0 and using the definition of q in Equation (2.139), gives

$$q = \varepsilon_c + \frac{t^2}{12G}\left(p_{,xx} + p_{,yy}\right) \tag{2.140}$$

Substitution of this into Equation (2.138) leads to

$$p_{,xxxx} + 2p_{,xxyy} + p_{,yyyy} - \alpha^2\left(p_{,xx} + p_{,yy}\right) = 0 \tag{2.141}$$

in which α is defined as

$$\alpha = \sqrt{\frac{12G\left(1-\nu^2\right)}{E_f t_f t}} \tag{2.121}$$

2.3.3 Approximate Boundary Conditions

In Equation (2.126), the in-plane shear stress of the elastomer, σ_{xy}, is assumed to be negligible

$$\sigma_{xy} = G\left(u_{,y} + v_{,x}\right) \approx 0 \tag{2.142}$$

Substituting the displacement assumptions in Equation (2.123) into the above equation and taking integration through the thickness of the elastomeric layer lead to

$$\frac{2}{3}\left(u_{0,y}+v_{0,x}\right)+\left(u_{1,y}+v_{1,x}\right)\approx 0 \tag{2.143}$$

The last term, $u_{1,y}+v_{1,x}$ is the in-plane shear strain of the reinforcement, which means that the in-plane shear strain of the reinforcement is of the second order and the in-plane shear force of the reinforcement, N_{xy}, is negligible. Therefore, we can assume

$$\begin{aligned} N_{xy,x}\left(a,y\right)&=0\\ N_{xy,y}\left(x,b\right)&=0 \end{aligned} \tag{2.144}$$

which give, from Equation (2.133),

$$\begin{aligned} N_{xx,x}\left(x,b\right)&\approx tp_{,x}\left(x,b\right)\\ N_{yy,y}\left(a,y\right)&\approx tp_{,y}\left(a,y\right) \end{aligned} \tag{2.145}$$

Another equation relating the pressure of the elastomer with the internal normal forces of the reinforcement is established by adding Equation (2.134), which gives

$$q=\frac{1-\nu}{E_f t_f}\left(N_{xx}+N_{yy}\right) \tag{2.146}$$

And combining this with Equation (2.140) to eliminate q leads to

$$\frac{t^2}{12G}\left(p_{,xx}+p_{,yy}\right)=\frac{1-\nu}{E_f t_f}\left(N_{xx}+N_{yy}\right)-\varepsilon_c \tag{2.147}$$

According to the assumption of pressure dominance given in Equation (2.126), the stress boundary conditions of the elastomeric layer give

$$\begin{aligned} p\left(\pm a,y\right)&=0\\ p\left(x,\pm b\right)&=0 \end{aligned} \tag{2.148}$$

The stress boundary conditions of the reinforcement give

$$\begin{aligned} N_{xx}\left(\pm a,y\right)&=0\\ N_{yy}\left(x,\pm b\right)&=0 \end{aligned} \tag{2.149}$$

The boundary condition $p\left(x,\pm b\right)=0$ means $p_{,x}\left(x,\pm b\right)=0$ which, when substituted into Equation (2.144), gives $N_{yy}\left(\pm a,y\right)$ being constant. From the boundary condition $N_{yy}\left(x,\pm b\right)=0,$ it is known that $N_{yy}\left(\pm a,\pm b\right)=0$, thus

$$N_{yy}(\pm a, y) = 0 \tag{2.150}$$

Bringing this into Equation (2.147) and using the boundary condition $N_{yy}(\pm a, y) = 0$ and from $p(x, \pm b) = 0$ lead to

$$p_{,xx}(\pm a, y) = -\frac{12G}{t^2}\varepsilon_c \tag{2.151}$$

The boundary condition $p(x, \pm b) = 0$ means $p(x, \pm b) = 0$ which gives $N_{yy}(\pm a, y)$ being constant. From the boundary condition $N_{yy}(x, \pm b)$, it is known that $N_{yy}(\pm a, \pm b) = 0$, thus

$$N_{xx}(x, \pm b) = 0 \tag{2.152}$$

Bringing this into Equation (2.147) and using the boundary condition $N_{yy}(x, \pm b) = 0$ and $p_{,xx}(x, \pm b) = 0$ from $p(x, \pm b) = 0$ lead to

$$p_{,yy}(x, \pm b) = -\frac{12G}{t^2}\varepsilon_c \tag{2.153}$$

Note that N_{xy} is not neglected when we derive the governing equation of the pressure in Equation (2.141). To solve for the pressure in this governing equation, we use the approximate boundary conditions of the pressure in Equations (2.151) and (2.153), which are derived by assuming that the derivatives of N_{xy} at the edges are negligible and stem from the assumption that the stress field of the elastomer is dominated by the pressure.

2.3.4 Solution of Pressure

To solve for the pressure, $p(x, y)$ is decomposed into two pressure components $p_1(x, y)$ and $p_2(x, y)$

$$p(x, y) = p_1(x, y) + p_2(x, y) \tag{2.154}$$

The boundary conditions for the pressure in Equations (2.148), (2.151), and (2.153) are split into two sets. Each pressure component satisfies a different set of boundary conditions. The first set of boundary conditions is

$$p_1(\pm a, y) = 0;\ p_{1,xx}(\pm a, y) = 0;\ p_1(x, \pm b) = 0;\ p_{1,yy}(x, \pm b) = -\frac{12G}{t^2}\varepsilon_c \tag{2.155}$$

and the second set of boundary conditions is

$$p_2(\pm a, y) = 0;\ p_{2,xx}(\pm a, y) = -\frac{12G}{t^2}\varepsilon_c;\ p_2(x, \pm b) = 0;\ p_{2,yy}(x, \pm b) = 0 \tag{2.156}$$

Adding the boundary conditions in Equation (2.156) yields the same boundary conditions defined in Equation (2.148). These pressure components are solved from the same governing equation in Equation (2.141), that is

$$p_{1,xxxx} + 2p_{1,xxyy} + p_{1,yyyy} - \alpha^2 \left(p_{1,xx} + p_{1,yy} \right) = 0 \tag{2.157}$$

$$p_{2,xxxx} + 2p_{2,xxyy} + p_{2,yyyy} - \alpha^2 \left(p_{2,xx} + p_{2,yy} \right) = 0 \tag{2.158}$$

Because the compression loading is symmetric with respect to the x-axis and y-axis, the pressure components are even functions of x and y. The first pressure component can be assumed to be a cosine series of y

$$p_1(x, y) = \sum_{n=1}^{\infty} f_1^{(n)}(y) \cos \gamma_n x \tag{2.159}$$

where the amplitude $f_1^{(n)}$ is an even function of y and

$$\bar{\gamma}_n = \left(n - \frac{1}{2} \right) \frac{\pi}{b} \tag{2.160}$$

Substituting Equation (2.159) into Equation (2.157) and using boundary conditions at $x = \pm a$ in Equation (2.155), $f_1^{(n)}$ is solved to have the form [Tsai and Kelly 2001]

$$f_1^{(n)}(y) = \varepsilon_c \frac{24G}{\pi \alpha^2 t^2} \frac{(-1)^{n-1}}{(n-1/2)} \left(\frac{\cosh \gamma_n y}{\cosh \gamma_n b} - \frac{\cosh \beta_n y}{\cosh \beta_n b} \right) \tag{2.161}$$

with

$$\beta_n = \sqrt{\gamma_n^2 + \alpha^2} \tag{2.162}$$

The second pressure component can be assumed to be a cosine series of y

$$p_2(x, y) = \sum_{n=1}^{\infty} f_2^{(n)}(x) \cos \bar{\gamma}_n y \tag{2.163}$$

where the amplitude $f_2^{(n)}$ is an even function of x and

$$\bar{\gamma}_n = \left(n - \frac{1}{2} \right) \frac{\pi}{b} \tag{2.164}$$

Substituting Equation (2.163) into Equation (2.158) and using boundary conditions at $x = \pm a$ in Equation (2.153), $f_2^{(n)}$ is solved to have the form [Tsai and Kelly 2001]

$$f_2^{(n)}(x) = \varepsilon_c \frac{24G}{\pi\alpha^2 t^2} \frac{(-1)^{n-1}}{(n-1/2)} \left(\frac{\cosh \bar{\gamma}_n x}{\cosh \bar{\gamma}_n a} - \frac{\cosh \bar{\beta}_n y}{\cosh \bar{\beta}_n a} \right) \tag{2.165}$$

With

$$\bar{\beta}_n = \sqrt{\bar{\gamma}_n^2 + \alpha^2} \tag{2.166}$$

Substitution of $p_1(x, y)$ in Equation (2.159) and $p_2(x, y)$ in Equation (2.163) into Equation (2.154) gives the solution of the pressure $p(x, y)$

$$\begin{aligned} p(x, y) = \varepsilon_c \frac{24GS^2}{\pi(\alpha a)^2} \left(1 + \frac{a}{b}\right)^2 \sum_{n=1}^{\infty} \frac{(-1)^{n-1}}{(n-1/2)} \cdot \\ \left[\left(\frac{\cosh \gamma_n y}{\cosh \gamma_n b} - \frac{\cosh \beta_n y}{\cosh \beta_n ab} \right) \cosh \gamma_n x + \left(\frac{\cosh \bar{\gamma}_n x}{\cosh \bar{\gamma}_n a} - \frac{\cosh \bar{\beta}_n x}{\cosh \bar{\beta}_n a} \right) \right] \end{aligned} \tag{2.167}$$

in which S is the shape factor of the rectangular layer of the elastomer defined as

$$S = \frac{ab}{(a+b)t} \tag{2.168}$$

2.3.5 Effective Compressive Modulus

The compression stiffness of an isolator is given by $K_c = E_c A / t_r$ where area $A = 4ab$ is the area of the isolator, t_r total thickness of the elastomer in the isolator, and E_c effective compressive modulus for a single bonded layer of elastomer, defined as $E_c = P / (A \varepsilon_c)$. Using the assumption in Equation (2.126), the resultant compression load P has the form

$$P = \int_{-b}^{b} \int_{-a}^{a} \sigma_{zz} dx dy \approx \int_{-b}^{b} \int_{-a}^{a} p(x, y) dx dy \tag{2.169}$$

Bringing the pressure solution $p(x, y)$ in Equation (2.167), the effective compressive modulus becomes

$$E_c = \frac{24GS^2}{\pi^2 (\alpha a)^2} \left(1 + \frac{a}{b}\right)^2 \sum_{n=1}^{\infty} \frac{1}{(n-1/2)^2} \left(\frac{\tanh \gamma_n b}{\gamma_n b} - \frac{\tanh \beta_n b}{\beta_n b} + \frac{\tanh \bar{\gamma}_n a}{\bar{\gamma}_n a} - \frac{\tanh \bar{\beta}_n a}{\bar{\beta}_n a} \right) \tag{2.170}$$

When the aspect ratio a/b tends to zero, Equation (2.170) is reduced to

$$E_c\big|_{a/b=0} = \frac{12GS^2}{(\alpha a)^2}\left(1+\frac{\tanh \alpha a}{\alpha a}\right) \tag{2.171}$$

which is the effective compressive modulus of the infinitely long strip isolator. When a tends to zero, Equation (2.170) becomes

$$E_c\big|_{\alpha=0} = \frac{12GS^2}{\pi^4}\left(1+\frac{a}{b}\right)^2 \sum_{n=1}^{\infty}\frac{1}{(n-1/2)^4}\cdot \left[\frac{\tanh \gamma_n b}{\gamma_n b} - \frac{1}{\cosh^2 \gamma_n b} + \frac{b^2}{a^2}\left(\frac{\tanh \bar{\gamma}_n a}{\bar{\gamma}_n a} - \frac{1}{\cosh^2 \bar{\gamma}_n a}\right)\right] \tag{2.172}$$

which is the effective compressive modulus of the rectangular elastomer with the rigid reinforcement. From Equation (2.170), it is known that the ratio $E_c/(GS^2)$ is a function of αa and the aspect ratio a/b. The variation of $E_c/(GS^2)$ with αa is plotted in Figure 2.14, which shows that the effective compressive modulus decreases with increasing αa.

To have a high compressive modulus, the value of αa must be small. Figure 2.14 also reveals that a larger value of a/b produces a larger value of the effective compressive modulus. For clarification, the in-plane stiffness of the reinforcement is defined as $k_f = E_f t_f/(1-\nu^2)$, from which Equation (2.121) becomes

$$\alpha a = \frac{a}{t}\sqrt{12\frac{Gt}{k_f}} \tag{2.173}$$

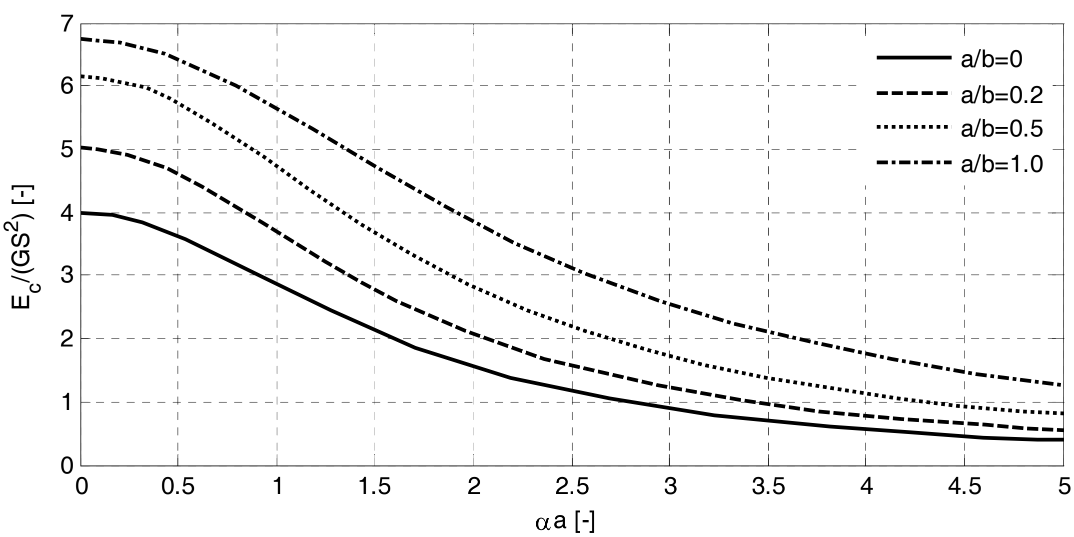

Figure 2.14 Variation of effective compressive modulus with αa in rectangular pad.

Substituting the shape factor S in Equation (2.168) and αa in Equation (2.173) into Equation (2.170), the normalized effective compression modulus E_c/G can be expressed as a function of the ratios a/b, a/t, and $k_f = Gt$. When a/t tends to infinity, Equation (2.170) becomes

$$E_c\big|_{a/t=\infty} = \frac{2}{\pi^2}\frac{k_f}{t}\sum_{n=1}^{\infty}\frac{1}{\left(n-1/2\right)^4}\left(\frac{\tanh\gamma_n b}{\gamma_n b}+\frac{\tanh\bar{\gamma}_n a}{\bar{\gamma}_n a}\right) \tag{2.174}$$

The curves of E_c/G versus k_f/Gt are plotted in Figure 2.15 for a/b and several a/t values, which shows that the effective compressive modulus increase with an increase in the reinforcement stiffness until reaching the asymptotic value in Equation (2.172). The curve of the smaller shape factor reaches a plateau at the smaller value of k_f/Gt The curves of E_c/G versus a/t are plotted in Figure 2.16 for $a/b=0.5$ and several k_f/Gt values, which shows that the effective compressive modulus increases with increasing shape factor until reaching the asymptotic value in Equation (2.174). The curve of the smaller value of k_f/Gt reaches a plateau at a smaller shape factor.

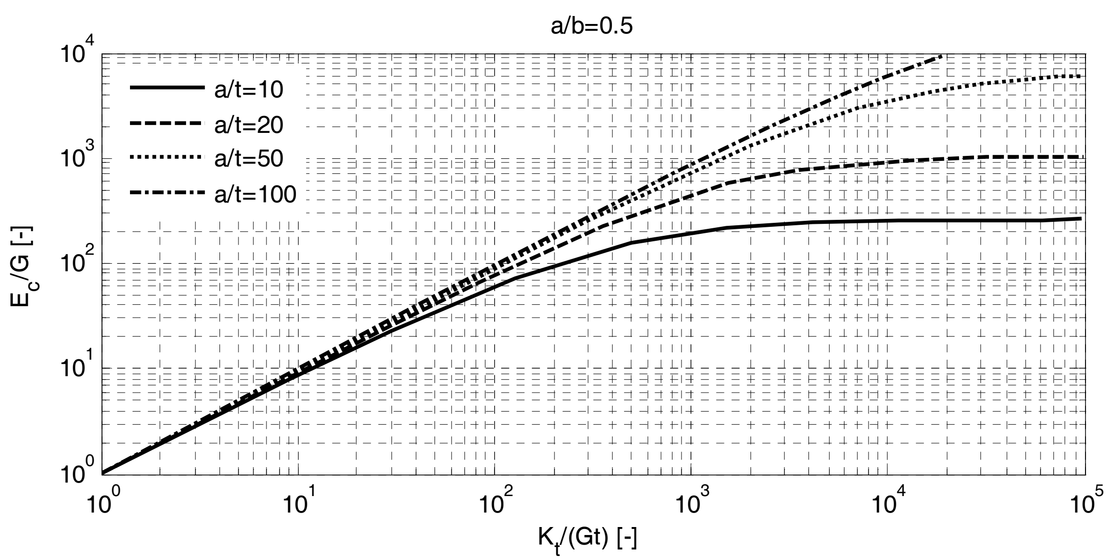

Figure 2.15 Variation of effective compressive modulus with reinforcement stiffness in rectangular pad (*a/b* = 0.5).

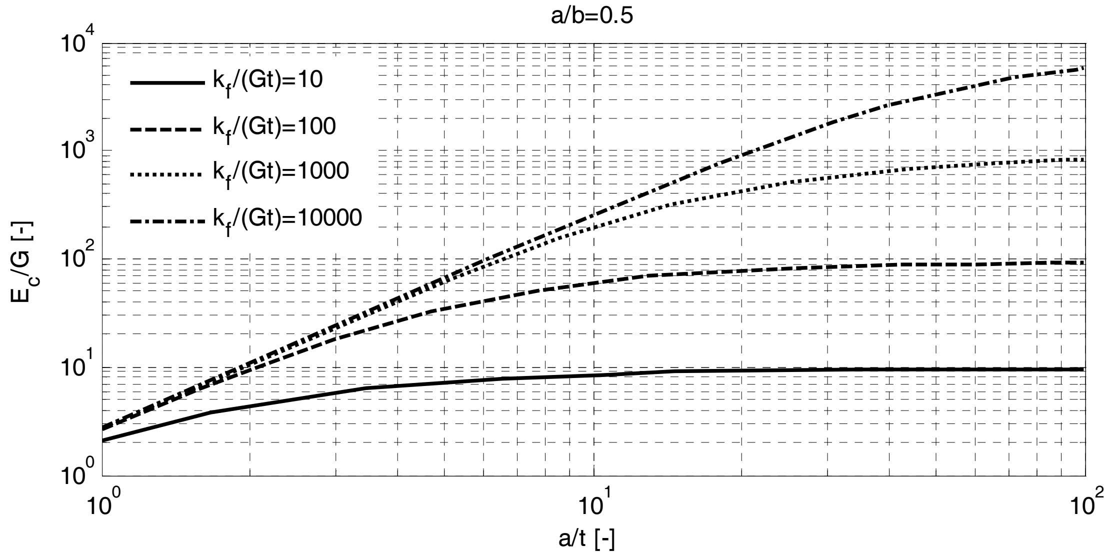

Figure 2.16 Variation of effective compressive modulus with width thickness in rectangular pad (*a/b* = 0.5).

To study the variation of the effective compressive modulus with the aspect ratio *a/b*, the ratio of the compressive modulus between the rectangular layers ($a/b > 0$) in Equation (2.170) and the infinitely long strip layer ($a/b = 0$) in Equation (2.171) is plotted in Figure 2.17, which reveals that the effective compressive modulus varies almost linearly with the aspect ratio *a/b*.

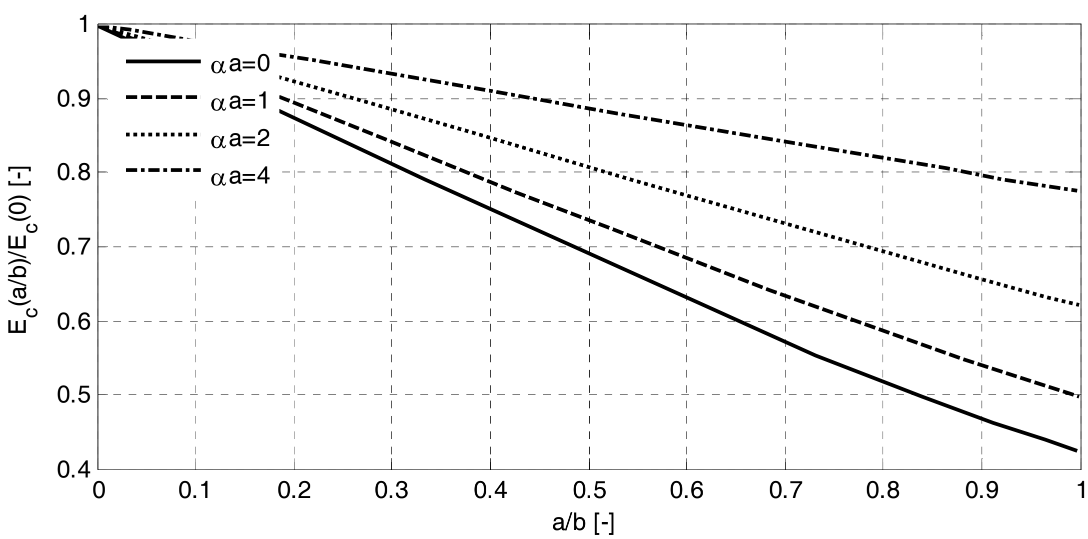

Figure 2.17 Ratio of effective compressive modulus of rectangular pad to infinitely long strip pad $(a/b=0)$ versus aspect ratio.

Utilizing the regression analysis on the data calculated from the exact formula in Equation (2.170), an approximate formula for the effective compressive modulus of rectangular reinforced layers is established [Tsai and Kelly 2001]

$$E_c = \frac{12GS^2}{(\alpha a)^2}\left(1-\frac{\tanh \alpha a}{\alpha a}\right)\left\{1+\frac{a}{b}\begin{bmatrix}-0.59+0.026\alpha a+0.074(\alpha a)^2+\\ -0.022(\alpha a)^3+0.0019(\alpha a)^4\end{bmatrix}\right\} \tag{2.175}$$

Because the range of the αa values used in the regression analysis is between 0 and 5, the effective compressive modulus in Equation (2.175) is only applicable to the range of $0 \le \alpha a \le 5$. The maximum error is smaller than 4% in this range.

2.4 GENERAL SHAPE PAD

2.4.1 Equilibrium in Elastomeric Layer

Consider a layer of elastomer in an arbitrarily shaped pad of thickness t and locate a rectangular Cartesian coordinate system (x, y, z) in the middle surface of the pad as shown Figure 2.18. The displacements of the elastomer along the coordinate directions are:

$$\begin{cases} u(x,y,z)=u_0(x,y)\left(1-4z^2/t^2\right)+u_1(x,y) \\ v(x,y,z)=v_0(x,y)\left(1-4z^2/t^2\right)+v_1(x,y) \\ w(x,y,z)=w(z) \end{cases} \tag{2.176}$$

$$\varepsilon_{xx}+\varepsilon_{yy}+\varepsilon_{zz}=-\frac{p}{K} \tag{2.177}$$

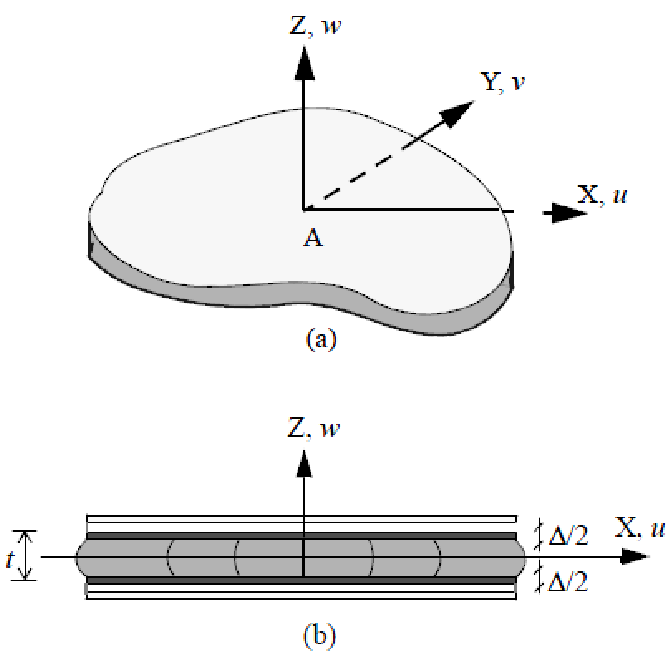

Figure 2.18 Constrained rubber pad and coordinate system.

Where K is the bulk modulus and

$$\varepsilon_{xx} = u_{o,x}\left(1 - \frac{4z^2}{t^2}\right) + u_{1,x} \tag{2.178}$$

$$\varepsilon_{yy} = v_{o,y}\left(1 - \frac{4z^2}{t^2}\right) + v_{1,y} \tag{2.179}$$

$$\varepsilon_{zz} = w_{,z} \tag{2.180}$$

in which the commas imply a partial differentiation with respect to the indicated coordinate.

Substituting in Equation (2.177), Equation (2.178), Equation (2.179), and Equation (2.180), we have

$$u_{o,x}\left(1 - \frac{4z^2}{t^2}\right) + u_{1,x} + v_{o,y}\left(1 - \frac{4z^2}{t^2}\right) + v_{1,y} + w_{,z} = -\frac{p}{K} \tag{2.181}$$

When integrated through the thickness this gives:

$$u_{o,x} + v_{o,y} + \frac{3}{2}\left(u_{1,x} + v_{1,y}\right) = \frac{3}{2}\left(\frac{\Delta}{t} - \frac{p}{K}\right) \tag{2.182}$$

Where Δ is the change of thickness of the pad (positive in compression).

Assuming that the stress state is dominated by the internal pressure, *p*, the equations of equilibrium for the stresses

$$\begin{aligned} \tau_{xx,x} + \tau_{xy,y} + \tau_{xz,z} &= 0 \\ \tau_{xy,x} + \tau_{yy,y} + \tau_{yz,z} &= 0 \\ \tau_{xz,x} + \tau_{yz,y} + \tau_{zz,z} &= 0 \end{aligned} \tag{2.183}$$

reduce under this assumption to

$$\begin{aligned} \tau_{xz,z} &= -\tau_{xx,x} = p_{,x} \\ \tau_{yz,z} &= -\tau_{yy,y} = p_{,y} \end{aligned} \tag{2.184}$$

Assuming that the material is linear elastic, the shear stresses τ_{xz} and τ_{yz} are related to the shear strains, γ_{xz} and γ_{yz}, by

$$\begin{aligned} \tau_{xz} &= G\gamma_{xz} \\ \tau_{yz} &= G\gamma_{xz} \end{aligned} \tag{2.185}$$

with G being the shear modulus of the material; thus,

$$\tau_{xz} = -Gu_0 \frac{8z}{t^2}$$
$$\tau_{yz} = -Gv_o \frac{8z}{t^2} \tag{2.186}$$

The equilibrium equations now become

$$\tau_{xx,x} = \frac{8Gu_0}{t^2} = -p_{,x}$$
$$\tau_{yy,y} = \frac{8Gv_o}{t^2} = -p_{,y} \tag{2.187}$$

2.4.2 Stress in the Reinforcement

The individual fibers are replaced by an equivalent sheet of reinforcement of thickness t_f. The internal state of stress in the reinforcing layer is denoted by the force field $\underline{F} = t_f \underline{\sigma}^f$. Equilibrium requires that

$$F_{xx,x} + F_{xy,y} + X = 0 \tag{2.188}$$

$$F_{yx,x} + F_{yy,y} + Y = 0 \tag{2.189}$$

where

$$X = -\tau_{xz}\Big|_{z=+\frac{t}{2}} + \tau_{xz}\Big|_{z=-\frac{t}{2}} \tag{2.190}$$

$$Y = -\tau_{yz}\Big|_{z=+\frac{t}{2}} + \tau_{yz}\Big|_{z=-\frac{t}{2}} \tag{2.191}$$

From Equation (2.186) we have

$$\tau_{xz}\Big|_{z=+\frac{t}{2}} = -\frac{8Gu_0}{2t}, \qquad \tau_{xz}\Big|_{z=-\frac{t}{2}} = +\frac{8Gu_0 t}{2t}, \tag{2.192}$$

and

$$\tau_{yz}\Big|_{z=+\frac{t}{2}} = -\frac{8Gv_0}{2t}, \qquad \tau_{yz}\Big|_{z=-\frac{t}{2}} = +\frac{8Gv_0 t}{2t}, \tag{2.193}$$

from which

$$X = \frac{8Gu_o}{t}, \qquad Y = \frac{8Gv_o}{t}; \tag{2.194}$$

Remembering that

$$\sigma_{xx}^{f} = \frac{F_{xx}}{t_f} = \frac{E_f}{1-\nu^2}\left(\varepsilon_{xx}^{f} + \nu\varepsilon_{yy}^{f}\right) \tag{2.195}$$

$$\sigma_{yy}^{f} = \frac{F_{yy}}{t_f} = \frac{E_f}{1-\nu^2}\left(\varepsilon_{yy}^{f} + \nu\varepsilon_{xx}^{f}\right) \tag{2.196}$$

$$\sigma_{xy}^{f} = \frac{F_{xy}}{t_f} = \frac{E_f}{2(1+\nu)}\gamma_{xy} \tag{2.197}$$

where

$$\varepsilon_{xx}^{f} = u_{1,x}, \qquad \varepsilon_{yy}^{f} = v_{1,y}, \qquad \gamma_{xy}^{f} = u_{1,y} + v_{1,x} \tag{2.198}$$

It can be derived that,

$$F_{xx} = \frac{t_f E_f}{1-\nu^2}\left[u_{1,x} + \nu v_{1,y}\right] \tag{2.199}$$

$$F_{yy} = \frac{t_f E_f}{1-\nu^2}\left[v_{1,y} + \nu u_{1,x}\right] \tag{2.200}$$

$$F_{xy} = \frac{t_f E_f}{2(1+\nu)}\left[u_{1,y} + v_{1,x}\right] \tag{2.201}$$

2.4.3 Complete System of Equation

Substituting these relations in Equation (2.188) and Equation (2.189) gives:

$$\frac{t_f E_f}{1-\nu^2}\left[u_{1,xx} + \nu v_{1,yx} + \frac{1}{2}\frac{1-\nu^2}{1+\nu}\left(u_{1,yy} + v_{1,xy}\right)\right] + \frac{8Gu_0}{t} = 0 \tag{2.202}$$

$$\frac{t_f E_f}{1-\nu^2}\left[v_{1,yy} + \nu u_{1,xy} + \frac{1}{2}\frac{1-\nu^2}{1+\nu}\left(u_{1,yx} + v_{1,xx}\right)\right] + \frac{8Gv_0}{t} = 0 \tag{2.203}$$

A complete system of five equations in five unknowns is derived

$$\tau_{xx,x} = \frac{8Gu_0}{t^2} = -p_{,x} \tag{2.204}$$

$$\tau_{yy,y} = \frac{8Gv_o}{t^2} = -p_{,y} \tag{2.205}$$

$$\frac{t_f E_f}{1-\nu^2}\left[u_{1,xx} + \nu v_{1,yx} + \frac{1}{2}\frac{1-\nu^2}{1+\nu}\left(u_{1,yy} + v_{1,xy}\right)\right] + \frac{8Gu_0}{t} = 0 \tag{2.206}$$

$$\frac{t_f E_f}{1-\nu^2}\left[v_{1,yy}+\nu u_{1,xy}+\frac{1}{2}\frac{1-\nu^2}{1+\nu}\left(u_{1,yx}+v_{1,xx}\right)\right]+\frac{8Gv_0}{t}=0 \tag{2.207}$$

$$u_{o,x}+v_{o,y}+\frac{3}{2}\left(u_{1,x}+v_{1,y}\right)=\frac{3}{2}\left(\frac{\Delta}{t}-\frac{p}{K}\right) \tag{2.208}$$

The unknowns are u_o, v_o, u_1, v_1, p. Considering the infinitely long rectangular pad of Figure 2.1 for which $u_o = 0$ and $v_o = 0$, the complete system of equations, in accordance with Section 2.1 reduces to:

$$p_{,x}=-\frac{8Gu_0}{t^2} \tag{2.209}$$

$$u_{1,xx}=-\frac{8Gu_0}{E_f t_f t} \tag{2.210}$$

$$u_{o,x}+\frac{3}{2}u_{1,x}=\frac{3}{2}\left(\frac{\Delta}{t}-\frac{p}{K}\right) \tag{2.211}$$

3 Finite Element Analysis of Unbonded Bearings

3.1 INTRODUCTION

Many studies of the global behavior of steel reinforced rubber bearings by means of FE analysis have been conducted: Seki [1987] investigated qualitatively the principal strain distributions in an elastomeric bearing denoting the rubber-steel interface as the most likely failure region; Takayama [1994] analyzed the principal strain and stress distributions for different values of the mean vertical pressure; and Simo and Kelly [1984] considered the stability of multilayer elastomeric bearings within the framework of two-dimensional finite elasticity through a finite element formulation which is capable of accounting for very general boundary conditions. Only few studies, however, have been conducted on the finite element analysis of FRBs. Next we investigated the load-displacement behavior and stress state of a strip-shaped, square and circular FRB. A series of FE analyses of the bearings were conducted using the general-purpose finite element program MSC.Marc 2005 [MSC.Software 2004].

Modeling the ultimate behavior of FRB is challenging for finite element codes because the problem involves a lot of settings such as the change of contact conditions, sliding, large strain (elastomeric behavior) and near-incompressibility of the rubber. Furthermore, the problem requires robust contact and self-contact capabilities because the bearing deforms enough to fold over upon itself. Use of traditional finite elements that have not been tailored for incompressibility analysis will produce extremely poor solutions due to ill-conditioning resulting from division by very small numbers. More importantly, the pathological behavior called volumetric mesh-locking is very likely to occur. The so-called mixed methods used in modern finite element treatments of incompressible and near-incompressible materials are based on the Hellinger-Reissner and Hu-Washizu variational principles [MSC Software 2000]. In mixed methods, both the stress and stains are treated as unknowns.

The results of analysis presented in this report are based on the widely popular mixed method proposed by Herrmann [1965]. A restricted case of the general Hellinger-Reissner variational principle is used to derive the stiffness equations. The software used to run the analyses is expressly designed to study elastomeric materials: they can be represented with popular material laws as Mooney-Rivlin and Boyce-Arruda, and a built-in curve fitting used that computes coefficients from stress-strain data. Moreover specialized element types automatically address numerical issues to get accurate solutions to large strain problems. The FE analyses consisted of two-dimensional models under the plane strain assumption for strip-type bearings and three-dimensional models for the other considered geometries.

3.1.1 Material and Mechanical Properties of the Bearings

For the two-dimensional models, the fiber reinforcement of the bearing is modeled using a rebar element: it is a tension element of a liner elastic isotropic material with Young's modulus E = 14,000 MPa, and thickness t_f = 0,07 mm (SET1) and G = 0.7 MPa (SET1). For the three-dimensional models, the reinforcing shim is modeled as a four nodes thin shell (i.e., no flexural rigidity) of constant thickness with Young's modulus E = 14,000 MPa and Poisson's ratio equal to zero.

The rubber is modeled by a single-parameter Mooney-Rivlin material (i.e., Neo-Hookean) with strain energy function that is described by the shear modulus G = 0.7 MPa, and the bulk modulus κ = 2000 MPa. In incompressible Mooney–Rivlin solids, the strain energy density function, W, is a linear combination of two invariants of the left Cauchy-Green deformation tensor:

$$W = C_1\left(\overline{I_1} - 3\right) + C_2\left(\overline{I_2} - 3\right) \tag{3.1}$$

In Equation (3.1), C_1 and C_2 are empirically determined material constants, and $\overline{I_1}$ and $\overline{I_2}$ are the first and the second invariant of the deviatoric component of the left Cauchy-Green deformation tensor

$$\overline{I_1} = J^{-2/3} I_1, \qquad I_1 = \lambda_1^2 + \lambda_2^2 + \lambda_3^2, \qquad J = \det\left(F\right) \tag{3.2}$$

$$\overline{I_2} = J^{-4/3} I_2, \qquad I_2 = \lambda_1^2\lambda_2^2 + \lambda_2^2\lambda_3^2 + \lambda_3^2\lambda_1^2; \tag{3.3}$$

where F is the deformation gradient. For an incompressible material, $J = 1$.

The constants C_1 and C_2 are determined by fitting the predicted stress from the above equations to experimental data. For a special case of uniaxial tension of an incompressible Mooney-Rivlin material, the stress-strain equation can be expressed as:

$$\sigma = 2\left(\left(1+\varepsilon\right) - \left(1+\varepsilon\right)^{-2}\right)\left(c_1 + c_2\left(1+\varepsilon\right)^{-1}\right) \tag{3.4}$$

The initial shear modulus is:

$$G = 2\left(C_1 + C_2\right) \tag{3.5}$$

If the material is incompressible, the initial tensile modulus E is calculated by:

$$E = 6\left(C_1 + C_2\right) \tag{3.6}$$

As mentioned above, the two-dimensional analysis is carried out under the plane strain assumption. In the plane models the rubber is modeled by the use of four-node, isoparametric, quadrilateral elements [element type 80]. The element uses bilinear interpolation functions, and the strains tend to be constant throughout the element. Hence, the use of a fine mesh is required. The pressure field is constant in this element. The stiffness of this element is formed using four-point Gaussian integration. This element is designed to be used for incompressible elasticity only. It can be used for either small strain behavior or large strain behavior using the Mooney or Ogden models.

For the three-dimensional models, the rubber is described by eight-node, isoparametric, three-dimensional brick elements with trilinear interpolation [element type 84].The element is based on the following type of displacement assumption and mapping from the (x, y, z) space into a cube in the :

$$\mathrm{X} = a_0 + a_1\xi + a_2\eta + a_3\xi + a_4\xi\eta + a_5\zeta\xi + a_6\xi\zeta + a_7\xi\eta\zeta \tag{3.7}$$

$$\Psi = b_0 + b_1\xi + b_2\eta + b_3\xi + b_4\xi\eta + b_5\eta\zeta + b_6\xi\zeta + b_7\xi\eta\zeta \tag{3.8}$$

Either the coordinate or function can be expressed in terms of the nodal quantities by the integration functions

$$\mathrm{X} = \sum_{i=1}^{8} X_i \Phi_i \tag{3.9}$$

$$\begin{aligned}
\Phi_1 &= \frac{1}{8}(1-\xi)(1-\eta)(1-\zeta) & \Phi_2 &= \frac{1}{8}(1+\xi)(1-\eta)(1-\zeta) \\
\Phi_3 &= \frac{1}{8}(1+\xi)(1+\eta)(1-\zeta) & \Phi_4 &= \frac{1}{8}(1-\xi)(1+\eta)(1-\zeta) \\
\Phi_5 &= \frac{1}{8}(1-\xi)(1-\eta)(1+\zeta) & \Phi_6 &= \frac{1}{8}(1+\xi)(1-\eta)(1+\zeta) \\
\Phi_7 &= \frac{1}{8}(1+\xi)(1+\eta)(1+\zeta) & \Phi_8 &= \frac{1}{8}(1-\xi)(1+\eta)(1+\zeta)
\end{aligned} \tag{3.10}$$

These elements use eight-point Gaussian integration as shown in Figure 3.1. Element 84 has one extra node with a single degree of freedom (pressure). This element uses a mixed formulation for incompressible analysis.

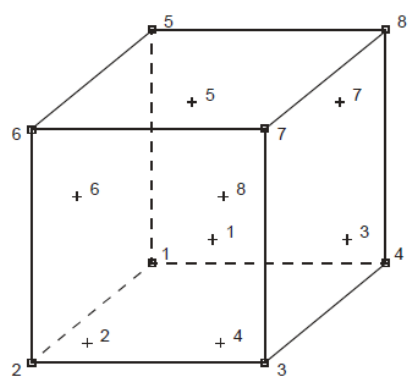

Figure 3.1 Integration points for element type 84.

Large strain theory was employed for all the analyses. The kinematics of deformation is described following the Updated Lagrangian formulation (i.e., the Lagrangian frame of reference is redefined at the last completed iteration of the current increment). Furthermore, a full Newton-Raphson solution method is used. Analysis of elastomeric bearings includes both nonlinear material and nonlinear geometric effects, since the bearings can undergo high shear strains during an earthquake

3.1.2 Contact Bodies, Boundary Conditions

The top and bottom support surfaces are modeled as rigid lines/surfaces. The contact between the rubber and the support surfaces is modeled by Coulomb friction with m = 0.9 for shear tests and m = 0 for compression test. The MSC.Marc has a CONTACT option that detects deformable body to deformable body or deformable body to rigid body contact as can occur under compression and large shear strains where the elastomer can contact the reinforcing shims.

3.2 INFINITELY LONG STRIP ISOLATORS

3.2.1 Geometrical Properties

Finite element models of FRBs with different shape factors are defined (S=B/2tr=43.48; 39.13; 34.78; 26.09; 21.74; 43.48). The different values of the shape factor are obtained by increasing the values of the base of the device (B = 250; 300; 350; 400; 450; 500 mm). The longitudinal dimension of the bearings is 750 mm. As shown in Figure 3.2, each device is made of twenty-eight rubber layers with twenty-nine interleaf fiber sheets. Each rubber layer is 5.75 mm thick (=t_r), and each fiber sheet is 0.07mm (=t_f) thick for SET1 and 0.25 mm thick for SET2. The geometrical characteristics are shown in Table 3.1, and the finite element discretization is shown in Figure 3.3. It consists of square four-node elements with side length of 2 mm and is denser at the contact interface.

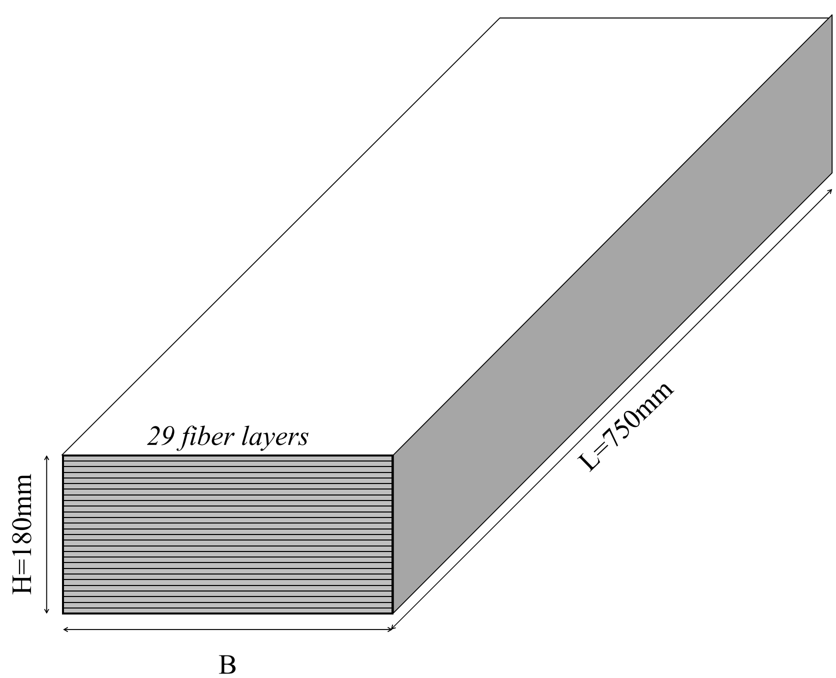

Figure 3.2 Strip type bearing showing reinforcements and dimensions.

Table 3.1 Geometrical properties of the long strip bearings.

	B [mm]	H [mm]	t_r [mm]	t_f [mm]	S [-]
Name	500				43.48
	450			0.07 (SET1)	39.13
	400	180	5.75		34.78
	350			0.25 (SET2)	30.43
	300				26.09
	250				21.74

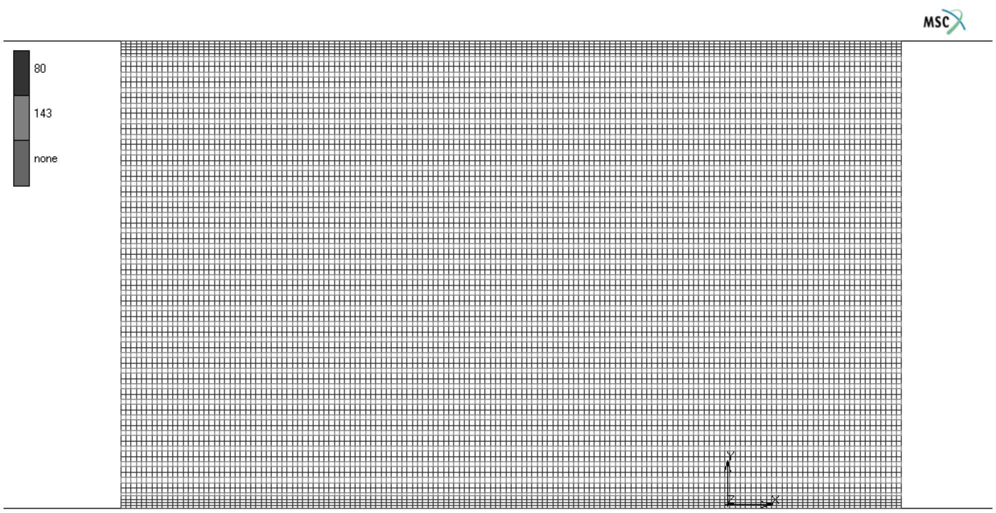

Figure 3.3 Model mesh and layout of the reinforcement layers [elements 143].

3.2.2 Compression Results

For design purposes, it is particularly important to predict the vertical stiffness and the collapse condition of FRBs under compression. Under compression, collapse of the bearing can occur for global failure due to buckling of the device, local ruptures of the reinforcement or the detachment of the rubber from the fiber sheets. Therefore, an accurate knowledge of the global characteristics of the device and of the stress distributions at the rubber fiber interfaces and in the fiber reinforcement is necessary.

Approximate analytical solutions for a pad confined by rigid and flexible reinforcements subjected to axial loads have been proposed [Kelly 2002]. Among these, the pressure solution, previously reported for strip-type bearings, seems to be particularly suited to provide a simple formulation of the vertical stiffness and to describe the stress state in elastomeric bearings. The goal of this section is to verify the validity of the results provided by the pressure solution by comparing them with results from the FE analysis.

Figures 3.4 and 3.5 show the contour maps of the equivalent stress obtained from analysis with Marc for bearings 250 and 500 (tf =0.07 mm) under pure compression. The contours show a stress concentration in the core of the bearings. For a given compressive force P (average pressure=P/A=3.45 MPa) in the considered range of bases, the maximum equivalent stress in the core of the bearing is unaffected by the change of the dimension of the device. Therefore, the stress in the core of the bearing is the same when the base dimension is modified. However, as expected, a new arrangement of stress distribution along the base length can be observed when the dimensions are changed. As a result, for bigger bearings as we move towards the free edges, the stress drops less aggressively than for smaller ones.

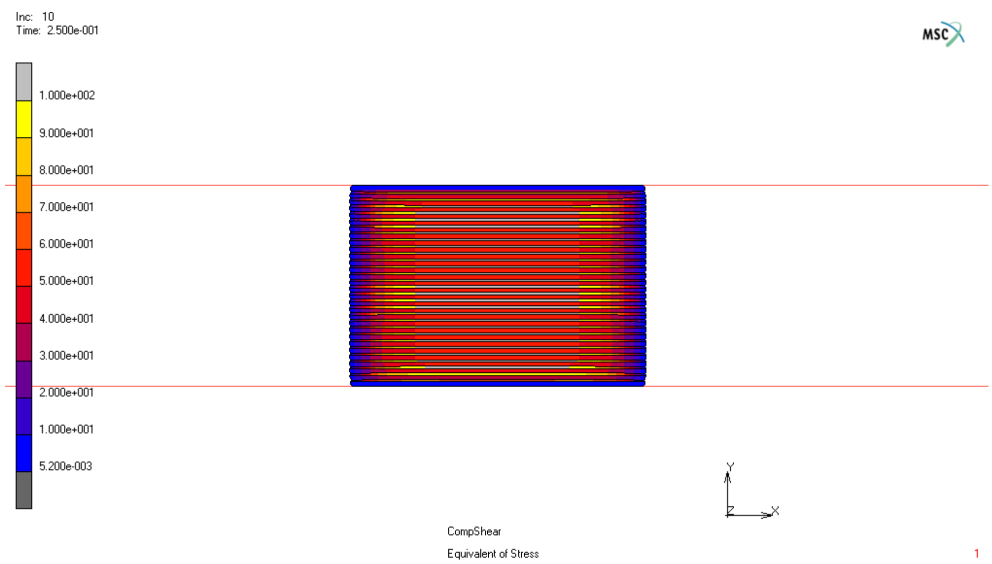

Figure 3.4 Von Mises stress contours at peak vertical force in a bearing of base B=250 mm [SET2 (t_f =0.07 mm)].

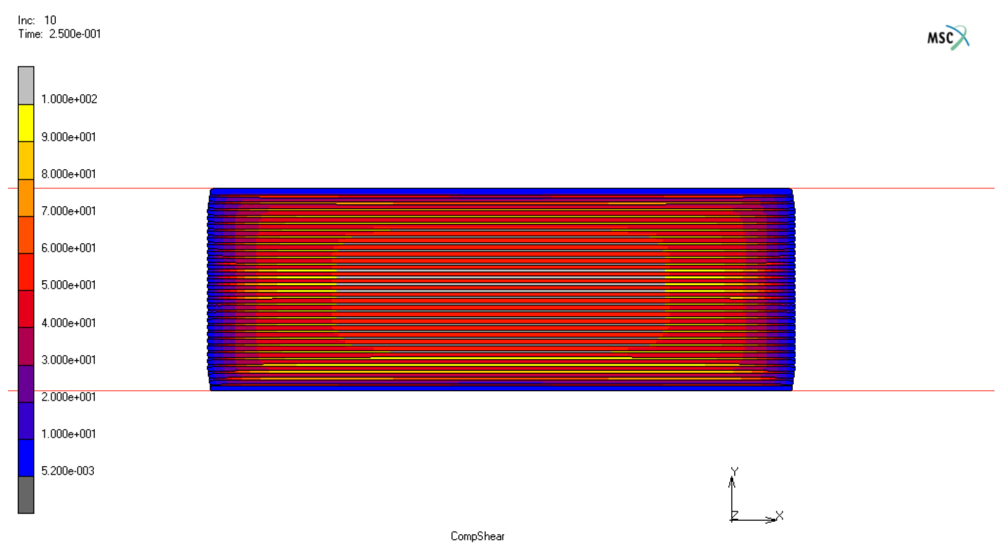

Figure 3.5 Von Mises stress contours at peak vertical force in a bearing of base B=500 mm [SET2 (t_f =0.07 mm)].

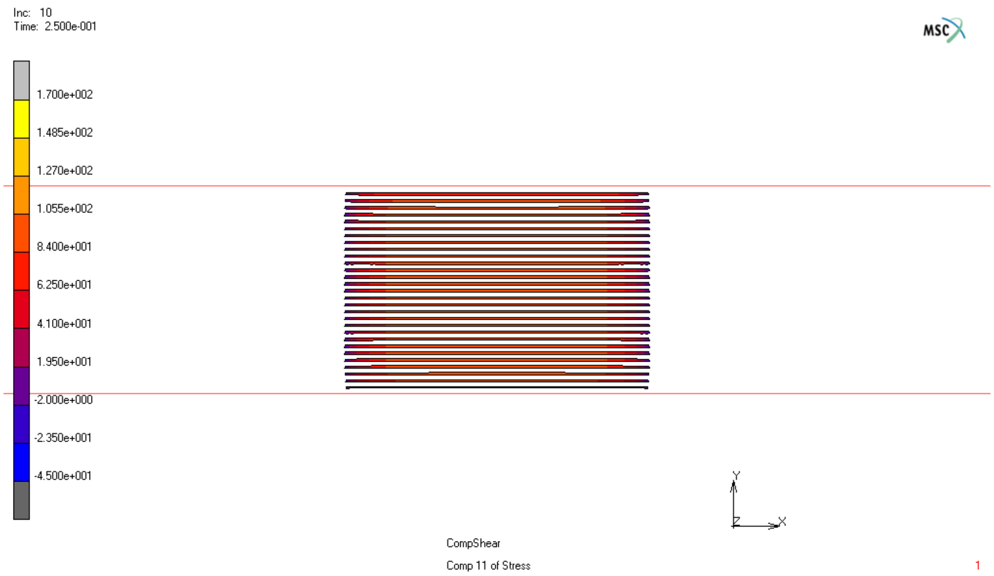

Figure 3.6 Tension contours in the fiber reinforcement (B=250 mm; S_v=3.45 MPa; SET2).

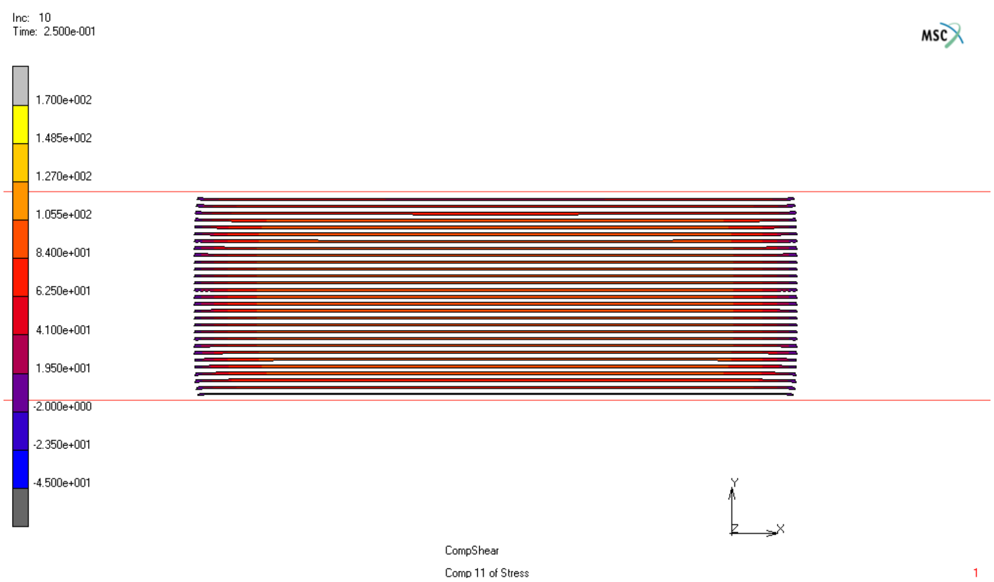

Figure 3.7 Tension contours in the fiber reinforcement (B=500 mm; S_v=3.45 MPa; SET2).

Figures 3.6 and 3.7 show the stress contours in the fiber layers. Note that due to the frictional restraint of the supports, the fiber layers closest to the supports are in compression. In the vertical direction the force displacement behavior is linear in the considered range of load. The results from FE analysis can be compared to the results of the pressure solution.

Recalling the results of Section 2.1, we can determine the vertical stiffness of the bearing, Kv, and the tensile stress in the reinforcement, σf (x),

$$K_V = \left(E_c A\right)/t_r \tag{3.11}$$

$$\sigma_f(x) = \varepsilon_c E_f \left(1 - \frac{\cosh \alpha x}{\cosh \alpha b}\right) \tag{3.12}$$

where

$$\alpha^2 = 12 G / E_f t_f t \tag{3.13}$$

and

$$E_c = 4G \frac{b^2}{t^2}\left(1 - \frac{2}{5}\alpha^2 b^2\right) \tag{3.14}$$

The previous formula refers to the hypothesis of incompressibility of the rubber. Taking the compressibility into account, we have:

$$E_c = K \frac{\beta^2}{\alpha^2 + \beta^2}\left(1 - \frac{\tanh \lambda}{\lambda}\right) \tag{3.15}$$

where K is the bulk modulus of the elastomer,

$$\beta = \sqrt{\frac{12G}{K} S^2} \tag{3.16}$$

$$\lambda = \sqrt{\alpha^2 + \beta^2} \tag{3.17}$$

Table 3.2 summarizes the model characteristics and the results of the pressure solution. The values reported in the Table 3.2 are plotted in Figure 3.8. For the considered range of bases (Eq. shape factors), the vertical stiffness is linear with respect to the shape factor. Figure 3.8 is a plot of the vertical stiffness as a function of the shape factor for the twelve bearings of different geometry/reinforcement.

Table 3.2 Model characteristics and pressure solution results (long strip bearings).

Geometrical and Mechanical Properties							
B	[mm]	250	300	350	400	450	500
H	[mm]	180					
L	[mm]	750					
t_f	[mm]	0.07 (SET1) 0.25 (SET2)					
n layers	[-]	29					
t_r	[mm]	6.37 (SET 1) 6.17 (SET 2)					
E_f	[MPa]	14000					
G	[MPa]	0.70					
Compression of Pad with Rigid Reinforcement							
$E_c = 4GS^2 \quad S = b/t$							
E_c	[MPa]	1082.93	1559.42	2122.54	2772.30	3508.69	4331.72
K_v	[N/mm]	1140919	1971509	3130683	4673206	6653842	9127356
Compression Stiffness with Compressibility of the Elastomer							
$E_c = K\left(1-\tanh\beta/\beta\right) \quad \beta^2 = 12Gb^2/Kt^2$							
SET 1 (K=2000 MPa)							
β	[-]	1.27	1.53	1.78	2.04	2.29	2.55
E_c	[MPa]	658.29	809.58	940.60	1051.90	1145.77	1224.92
K_v	[N/mm]	693539	1023520	1387352	1773163	2172814	2581018
SET 2							
β	[-]	1.31	1.575636	1.84	2.10	2.36	2.63
E_c	[MPa]	682.37	834.8608	965.72	1076.09	1168.63	1246.34
K_v	[N/mm]	740639	1087373	1467451	1868746	2283149	2705508

Compression Stiffness with Flexible Reinforcement							
$E_c = \dfrac{E_f t_f}{t}\left(1-\dfrac{\tanh\alpha}{\alpha}\right) \qquad \alpha = \sqrt{12\dfrac{Gb^2}{E_f t_f t}}$							
SET 1							
α	[-]	4.59	5.51	6.43	7.34	8.26	9.18
E_c	[MPa]	120.60	126.19	130.19	133.19	135.52	137.39
K_v	[N/mm]	127059	159541	192028	224515	257003	289491
SET 2							
α	[-]	2.46	2.96	3.45	3.94	4.44	4.93
E_c	[MPa]	340.49	376.57	403.26	423.59	439.49	452.25
K_v	[N/mm]	369562	490469	612775	735607	858636	981738

Table 3.2 (continued)

Flexible Reinforcement and Compressibility							
$E_c = K \dfrac{\beta^2}{\alpha^2+\beta^2}\left(1-\dfrac{\tanh\lambda}{\lambda}\right) \quad \lambda^2=\alpha^2+\beta^2$							
SET 1 (K=2000MPa)							
β	[-]	1.27	1.53	1.78	2.04	2.29	2.55
λ	[-]	4.76	5.72	6.67	7.62	8.58	9.53
E_c	[MPa]	113.10	118.11	121.69	124.37	126.45	128.12
K_v	[N/mm]	119160	149319	179481	209643	239806	269969
SET 2							
β	[-]	1.31	1.58	1.83	2.10	2.36	2.63
λ	[-]	2.79	3.35	3.91	4.47	5.03	5.59
E_c	[MPa]	284.90	310.41	329.02	343.08	354.05	362.83
K_v	[N/mm]	309229	404302	499954	595796	691700	787625

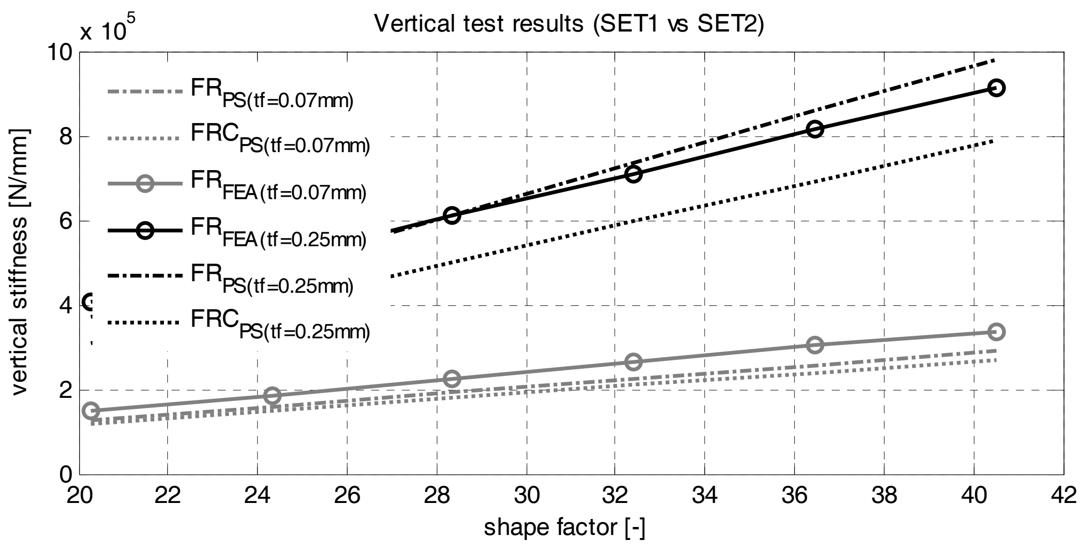

Figure 3.8 Vertical stiffness (FE analysis versus pressure solution).

The gray and the black lines refer to SET1 and SET2, respectively. The continuous lines (FRFEA) are plots of the FE analysis results, FRPS and FRCPS are the theoretical vertical stiffness results of FRBs for incompressible and compressible material respectively. The FE analysis and pressure solution outputs result are in good agreement. The FE analysis gives higher values of vertical stiffness because of a stiffening contribution of the quadratic mesh.

Figure 3.9 and Figure 3.10 show the plot of tensile stress as a function of the dimensionless length of the device, *x/B*, for the mid-height fiber layer—where the stresses are the largest—for B=250 mm and B=500 mm, respectively. The gray lines refer to t_f = 0.07 mm (SET1) while the black lines refer to t_f = 0.25 mm (SET2). In each figure the solid lines represent the pressure solution results and the dashed lines represent the FE analysis results. The pressure solution and the FE analysis curves have the same trend.

For all the considered values of shape factor , the pressure solution gives higher values of vertical stiffness than the FE analysis. The results show that the pressure solution loses accuracy as the shape factor increases. This result is in agreement with [Kelly and Takhirov 2002]. The author suggests that the loss of accuracy is due mainly to the assumption of incompressibility of the material, and that the results presented there can be considered valid only for low values of the shape factors (S < 5).

The results of the pressure solution (dashed lines) show a good agreement with the output of the FE analysis. In Figure 3.11 the ratio between the stresses derived by the FE model and the stresses derived by the pressure solution is plotted against the dimensionless length *x/B*. The pressure solution gives accurate results for the description of the stress of the fiber in the bearing's core. Towards the free edges of the bearings, for a length of 10% of the base, the FE and the pressure solution results are different. This difference is very low for bearings with lower shape factors, but it is significant as the shape factor increases.

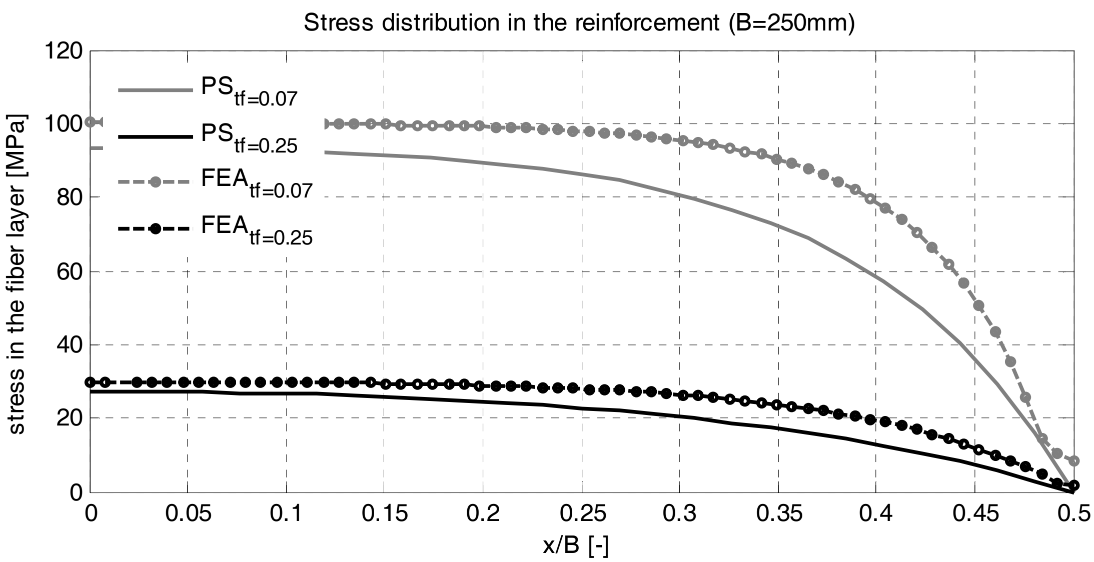

Figure 3.9 Stress distributions in the reinforcement (FE analysis versus pressure solution) for B=250 mm.

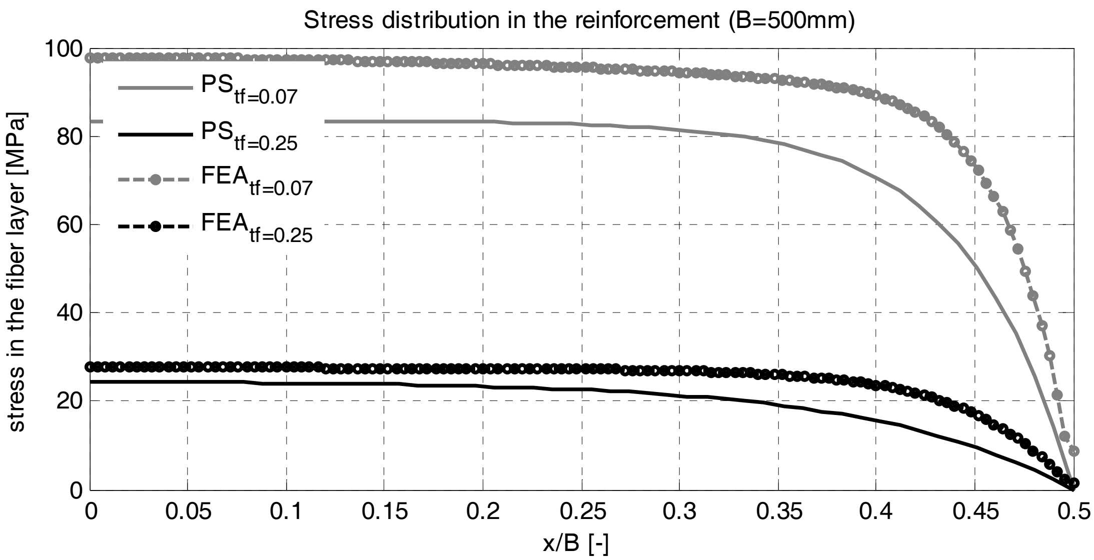

Figure 3.10 Stress distributions in the reinforcement (analyses versus pressure solution) for B=500 mm.

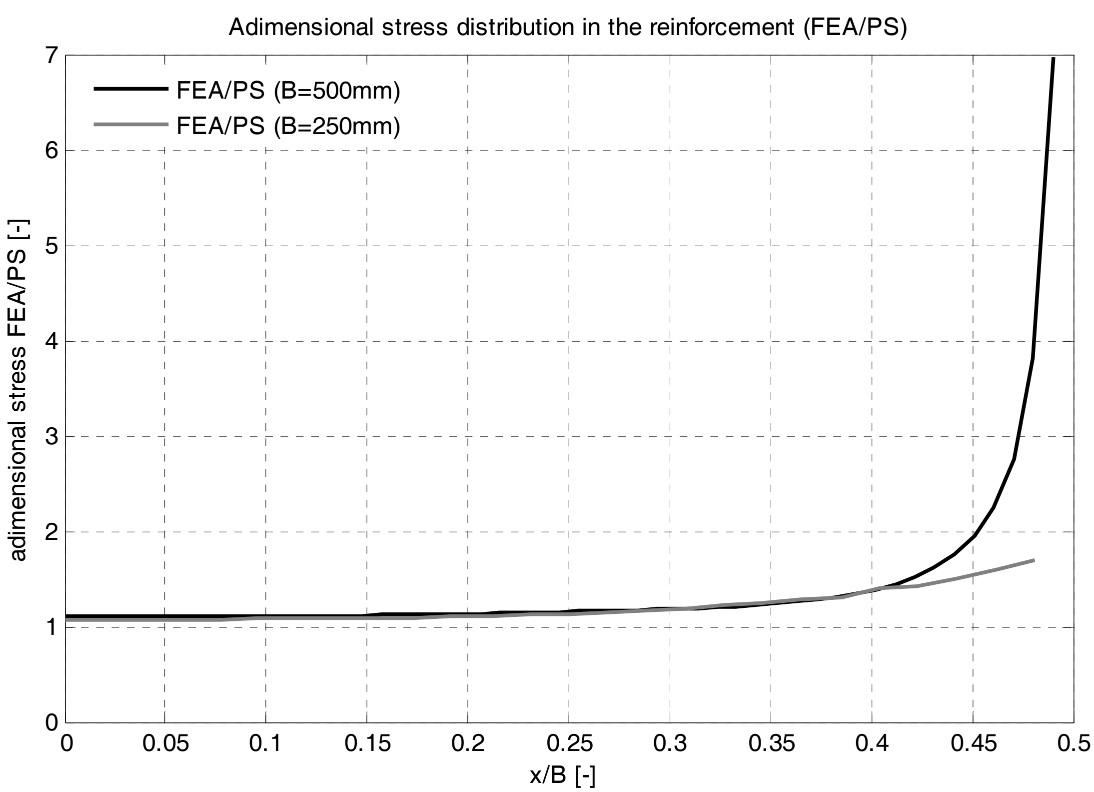

Figure 3.11 Non-dimensional stress (FE/pressure solution) against non-dimensional length (*x*/*B*).

3.2.3 Shear Results

In the second part of the analysis, a constant vertical load is applied, and then the horizontal displacement is increased in order to investigate the ultimate behavior of the bearings. Figure 3.12 and Figure 3.13 are Von Mises stress contour maps for B=250 mm and B=500 mm [SET1, t_f = 0.07 mm)], respectively, at the displacement that corresponds to the peak force in the load-displacement curve.

The aforementioned figures clearly show the favorable response of an isolator that is not bonded to the top or bottom supports. This is due to the elimination of tension in the elastomer. In a bonded bearing under the simultaneous action of shear and compression, the presence of an unbalanced moment at both top and bottom surfaces produces a distribution of tensile stresses in the triangular region outside the overlap between top and bottom. The compression load is carried through the overlap area, and the triangular regions created by the shear displacement provide the tensile stresses to balance the moment. These tensile stresses must be sustained by the elastomer and also by the bonding between the elastomer and the steel reinforcement plates. The provision of these bonding requirements is the main reason for the high cost of current designs of isolator bearings for buildings. With the elimination of these tension stresses, the bonding requirements for this type of bearing are reduced.

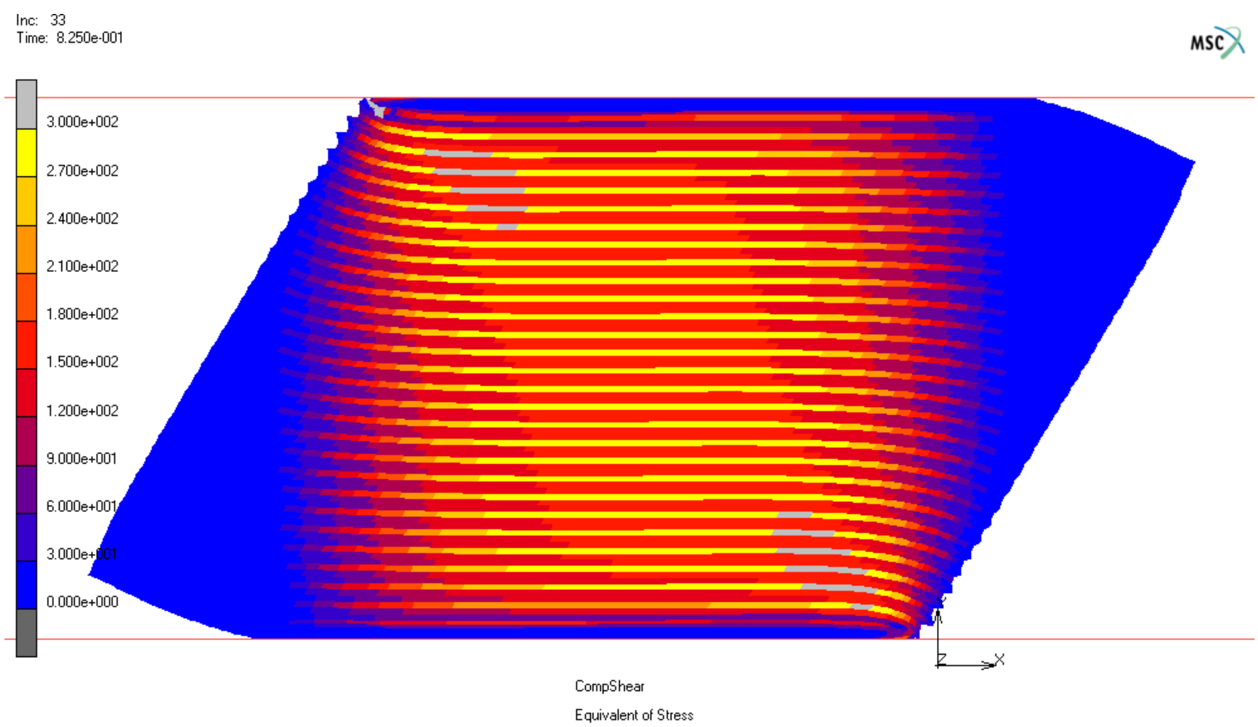

Figure 3.12 Von Mises stress contours at peak horizontal force in a bearing of base B=250 mm.

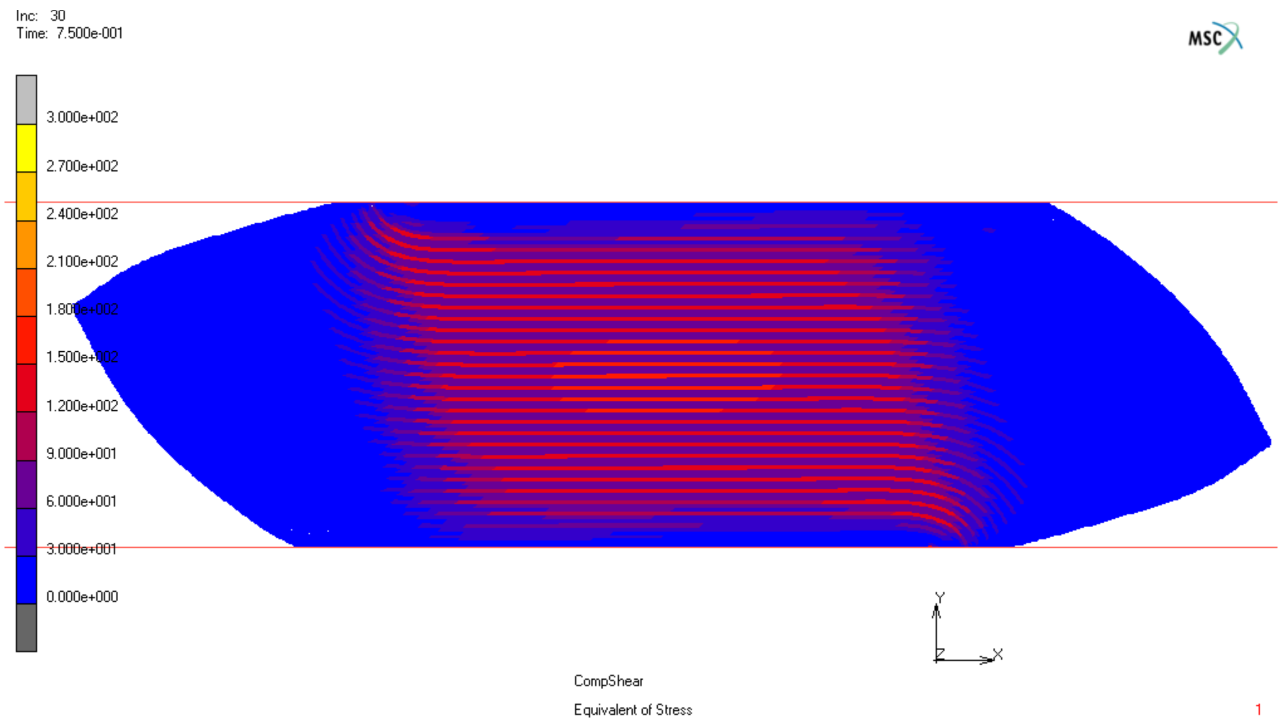

Figure 3.13 Von Mises stress contours at peak horizontal force in a bearing of base B=500 mm.

For both bearings, a concentration of stress in the cores is evident. The stress at peak horizontal force is twice the one due to compressive load. For different geometries, the maximum value of stress is the same. Changing shape factor has the only effect of changing the distribution of the stress in the bearing. Figures 3.14 and 3.15 are the stress contours in the reinforcement at peak horizontal force for which the previous considerations are still valid. Figure 3.16 plots the horizontal load as a function of the horizontal displacement for the six bearings of SET1 under a vertical pressure of 3.45 MPa. The maximum horizontal displacement is double for the 500-mm bearing than for the 250-mm bearing, while the peak force is quadruple. Figure 3.17 shows the horizontal load versus the dimensionless horizontal displacement. The peak lateral displacement that the bearings exhibit is approximately equal to half the base. Figure 3.18 is a plot of the shear stress versus shear strain curves.

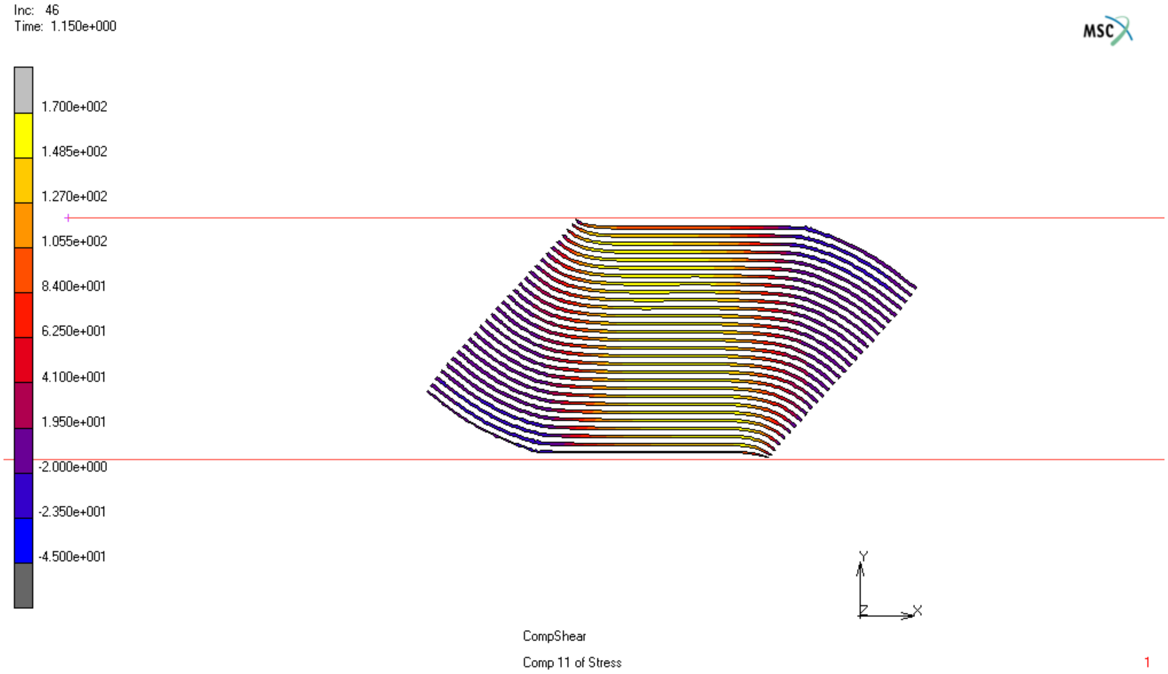

Figure 3.14 **Tension contours in the fiber reinforcement at maximum shear (B=250 mm).**

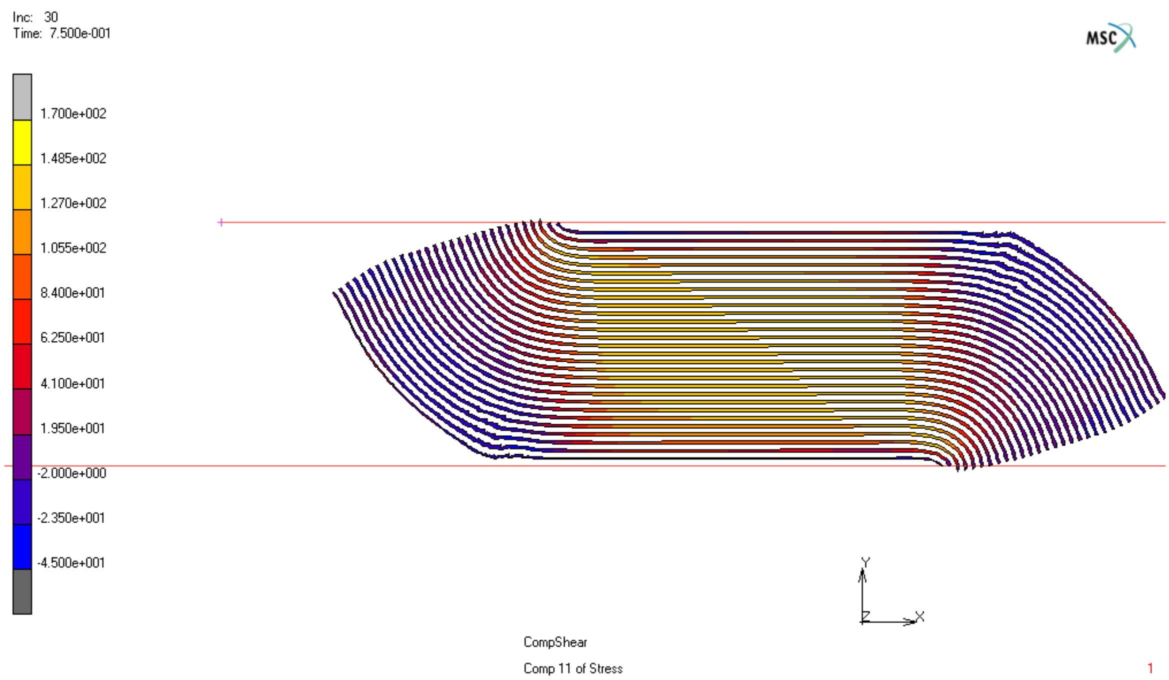

Figure 3.15 **Tension contours in the fiber reinforcement at maximum shear (B=500 mm).**

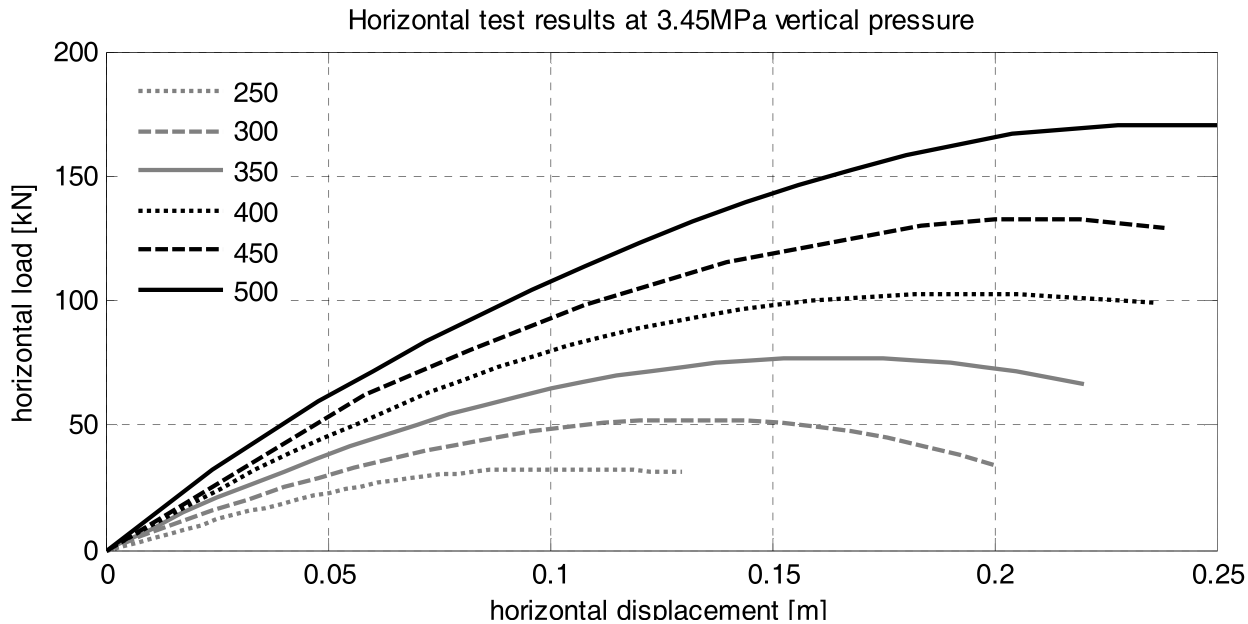

Figure 3.16 Force-displacement curves.

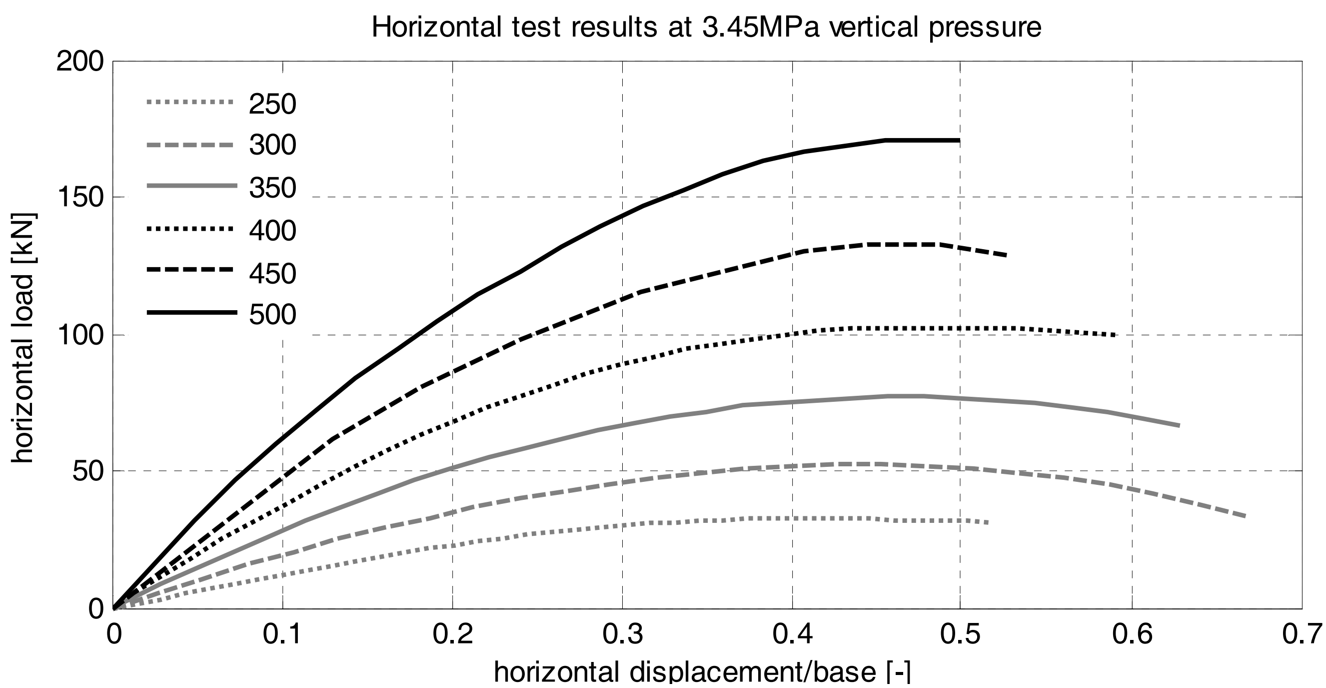

Figure 3.17 Force-displacement/base curves.

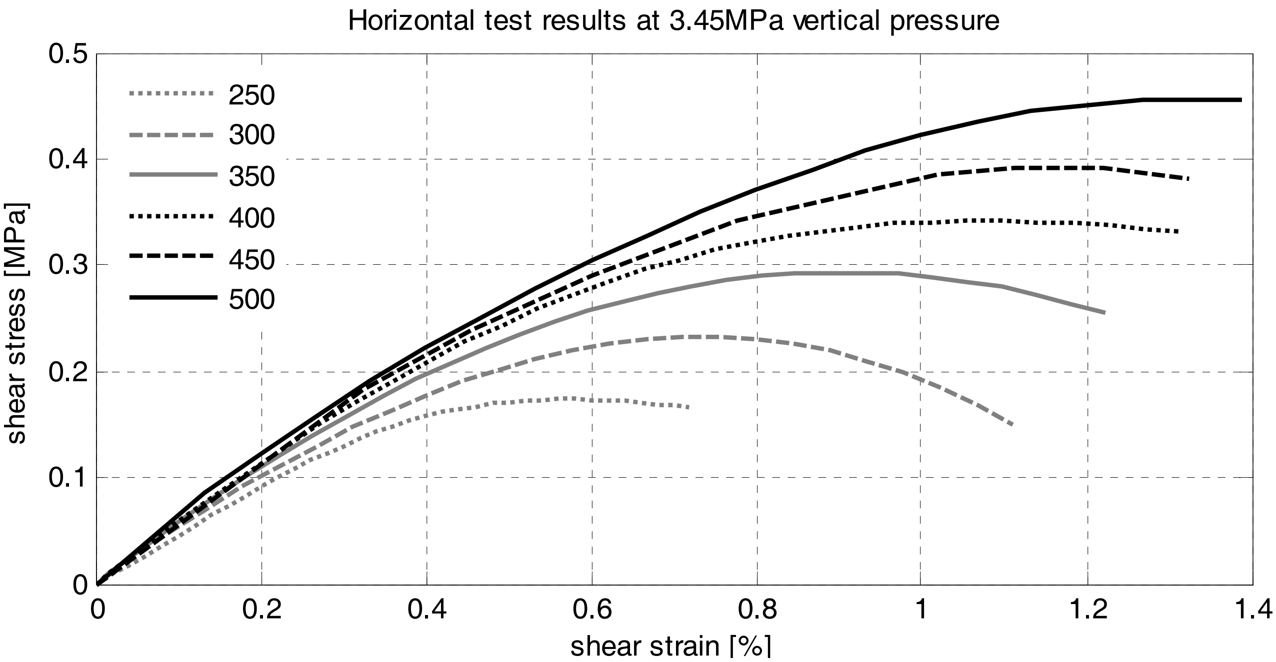

Figure 3.18 Stress-strain curves.

These curves are straight lines up to the value of the lateral load for which roll-off of the right end starts to occur. A progressive reduction of the lateral tangent stiffness is then observed with further increase of the lateral load. The large deformation that FRBs experience can be modeled accurately in Marc. However, the finite element mesh distorts so heavily that the analysis becomes grossly inaccurate or stops due to individual mesh elements turning inside out and pre-specified convergence criteria not being satisfied. This problem could be solved by employing remeshing, but the program has no algorithm that can be used to automatically remesh the rebar elements. Therefore, the ultimate theoretical displacement cannot be verified easily, because of the very large distortion in the mesh. The values that describe the ultimate behavior for the bearings SET1 are summarized in Table 3.3.

Table 3.3 Ultimate performances of the bearings (SET1) under horizontal load.

B [mm]	S [-]	$F_{h,u}$ [kN]	τ_u [MPa]	Δ_u [mm]	Δ_u/B [-]	γ_u [%]
500	43.48	170.5	0.45	204	0.4	1.1
450	39.13	139.9	0.41	195	0.4	1.1
400	34.78	104.1	0.35	190	0.5	1.1
350	26.09	77.17	0.29	167	0.5	0.9
300	21.74	52.13	0.23	136	0.5	0.8
250	43.48	32.92	0.18	104	0.4	0.6

3.3 CIRCULAR BEARINGS

3.3.1 Geometrical Properties

Finite element models of FRBs with different shape factors are defined (S=Φ/4, t_r= 10.13; 12.17; 14.18; 16.21; 18.23; 20.26). The different values of the shape factor are obtained by increasing the values of the diameter of the device (Φ = 250; 300; 350; 400; 450; 500 mm). As shown in Figure 3.19, each device is made of twenty-nine fiber layers with twenty-eight interleaf rubber sheets. Each rubber layer is 5.75 mm thick (=t_r), and each fiber sheet is 0.07 mm (=t_f) thick for SET1 and 0.25 mm thick for SET2. The geometrical characteristics are shown in Table 3.4. The FE discretization is shown in Figure 3.20, consisting of 8 + 1-node hexahedron elements with side length of ~2 mm.

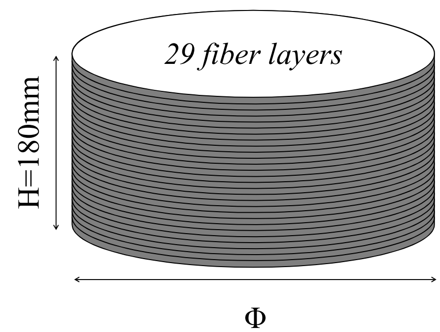

Figure 3.19 Circular type bearing showing reinforcements and dimensions.

Table 3.4 Geometrical properties of the circular bearings.

	Φ [mm]	H [mm]	t_r [mm]	t_f [mm]	S [-]
	500				20.26
	450			0.07 (SET1)	18.23
Name	400	180	5.75		16.21
	350				14.18
	300			0.25 (SET2)	12.17
	250				10.13

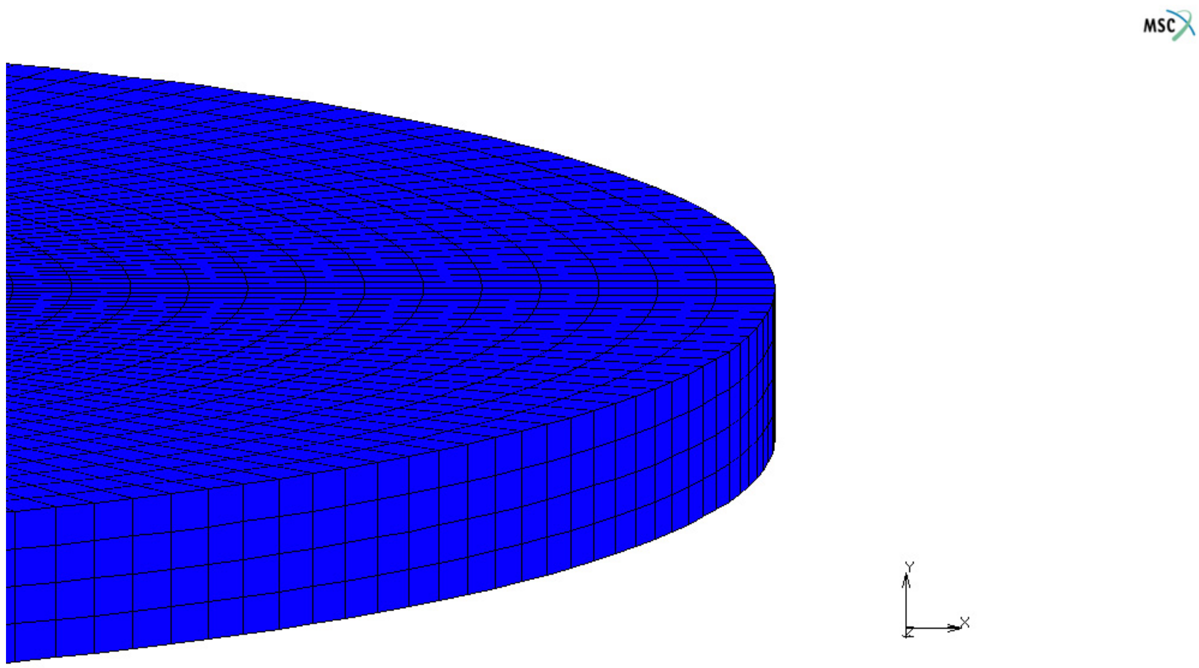

Figure 3.20 Model mesh and layout of the reinforcement layers (elements 143).

3.3.2 Compression Results

The goal of this section is to verify the validity of the results provided by the pressure solution by comparing them with results from FE analysis. Figures 3.21–3.24 show the contour maps of the equivalent stress in cross sections of a rubber layer obtained from analysis with Marc for bearings 250 mm and 500 mm [(t_f = 0.07 mm) and (t_f = 0.25 mm)], respectively, under pure compression (peak vertical force = average pressure = P/A = 3.45 MPa). The plots show the results on half of the bearing. Figures 3.25 and 3.29 show the stress contours in the fiber layers. In the vertical direction the force displacement behavior is linear in the considered range of load. The results from FE analysis can be compared to the results of the pressure solution.

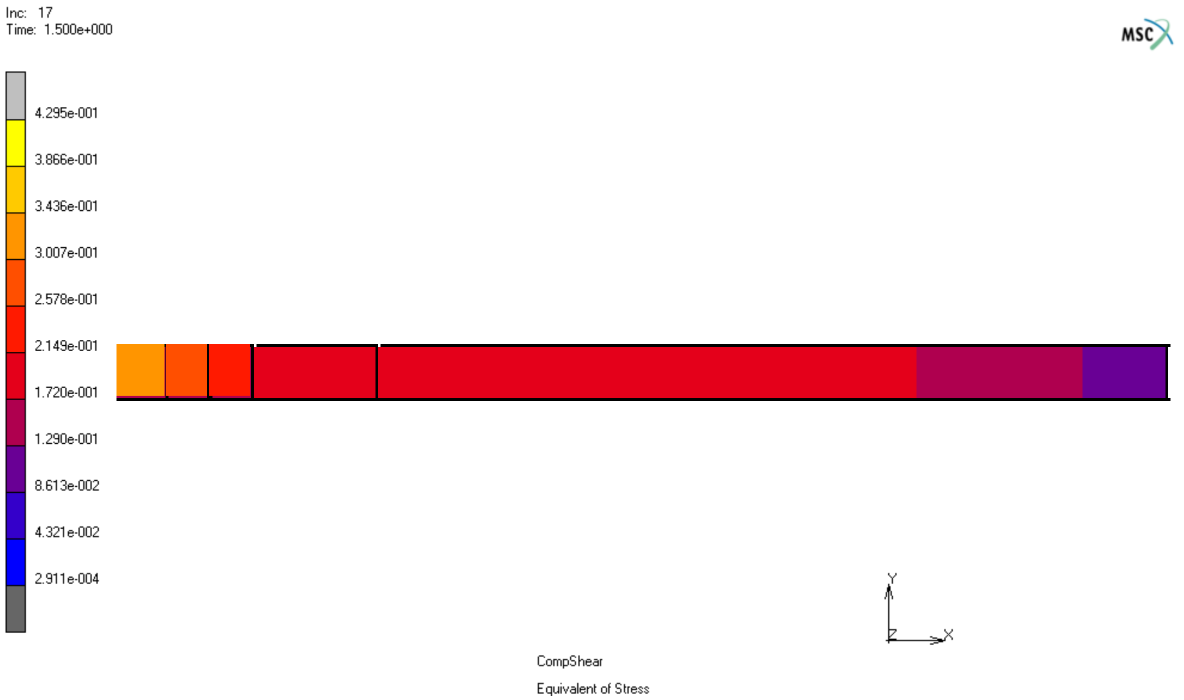

Figure 3.21 Von Mises stress contours at peak vertical force in a cross section of a circular bearing (Φ=250 mm–SET1 t_f =0.07 mm).

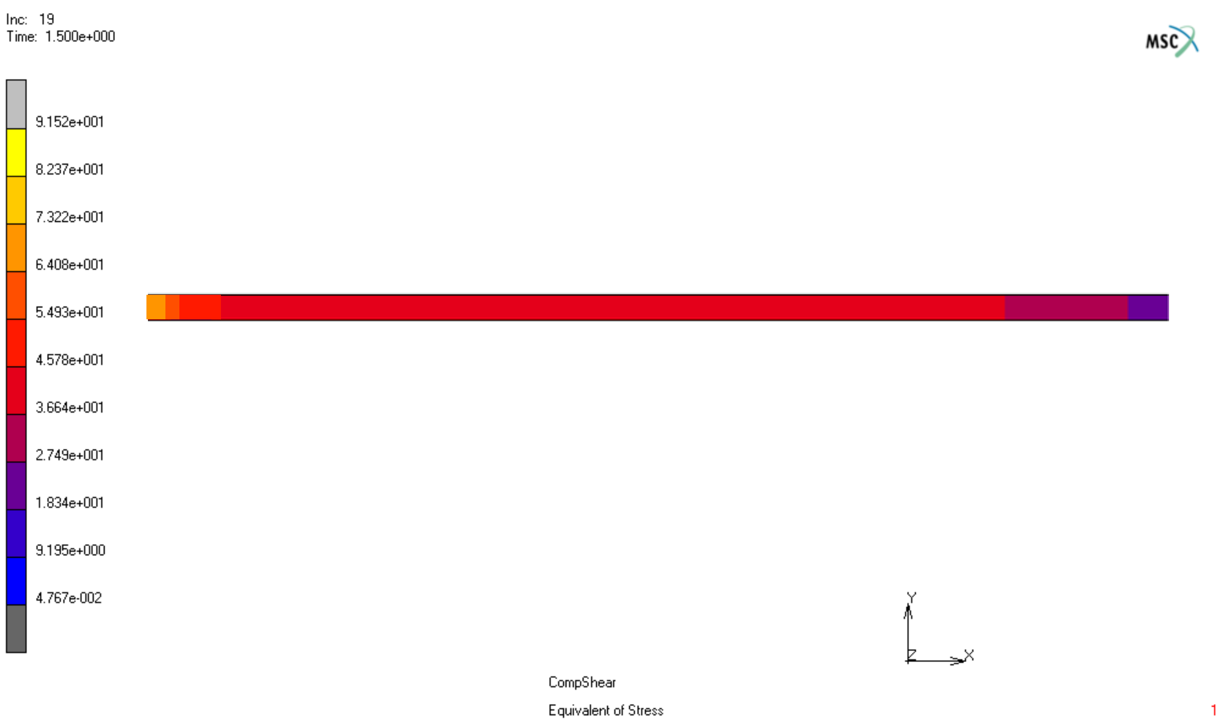

Figure 3.22 Von Mises stress contours at peak vertical force in a cross section of a circular bearing (Φ=500 mm–SET1 t_f =0.07 mm).

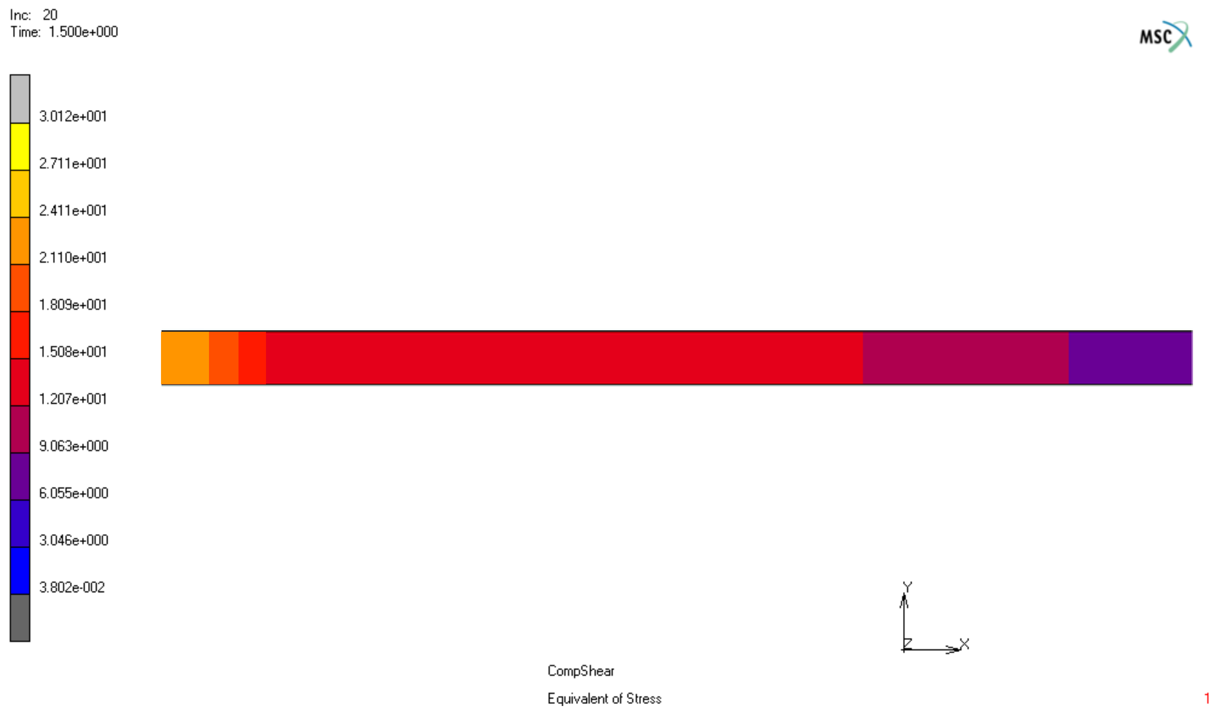

Figure 3.23 Von Mises stress contours at peak vertical force in a cross section of a circular bearing (Φ=250 mm–SET1 t_f =0.25 mm).

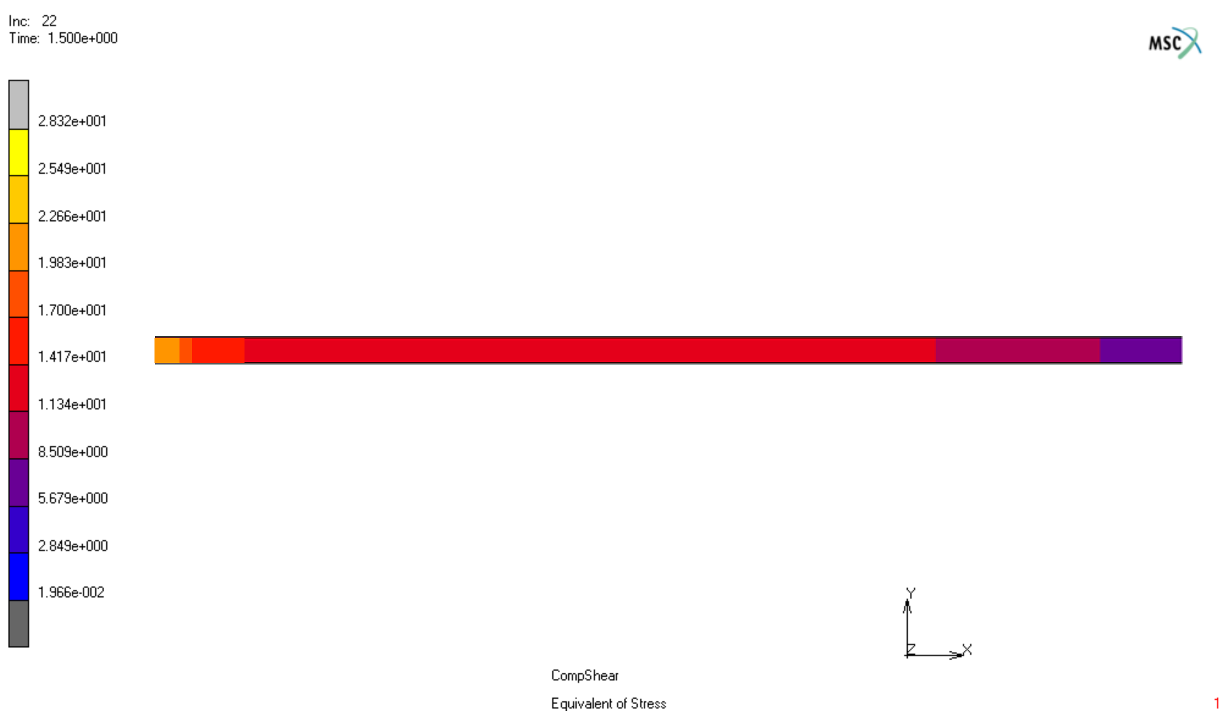

Figure 3.24 Von Mises stress contours at peak vertical force in a cross section of a circular bearing (Φ=500 mm - SET2 t_f =0.25 mm).

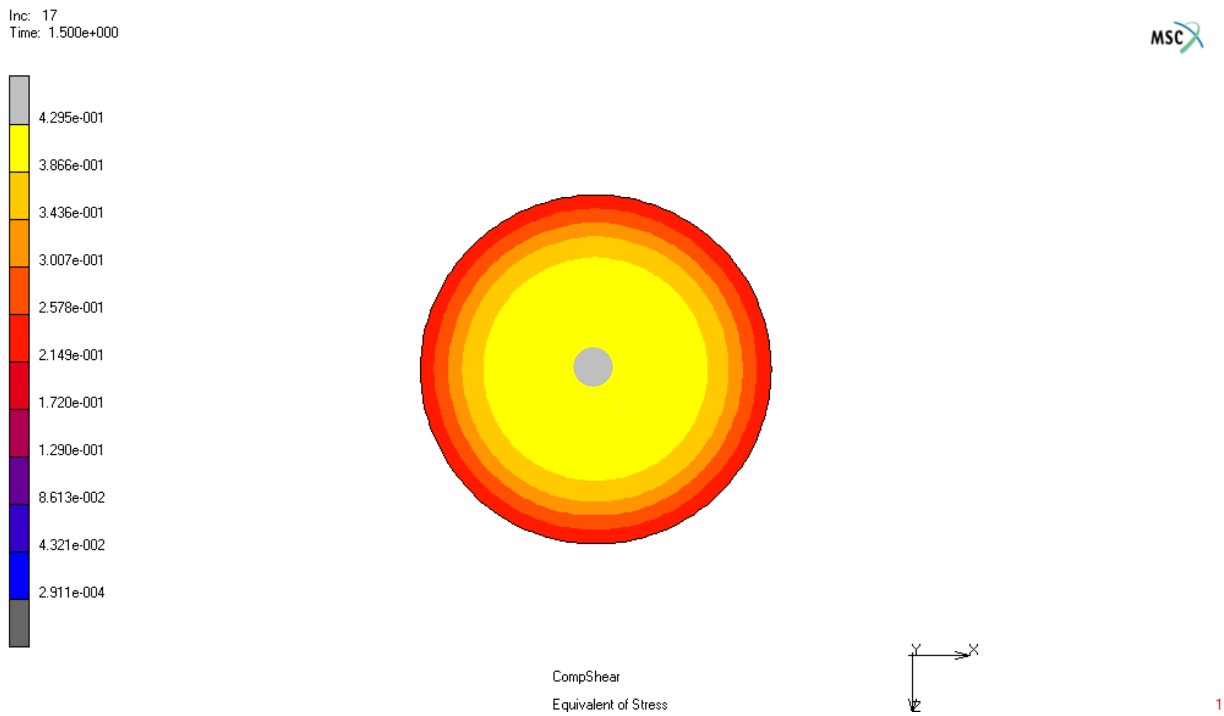

Figure 3.25 Tension contours in the fiber reinforcement (Φ=250 mm–SET1 t_f=0.07 mm, S_v=3.45 MPa).

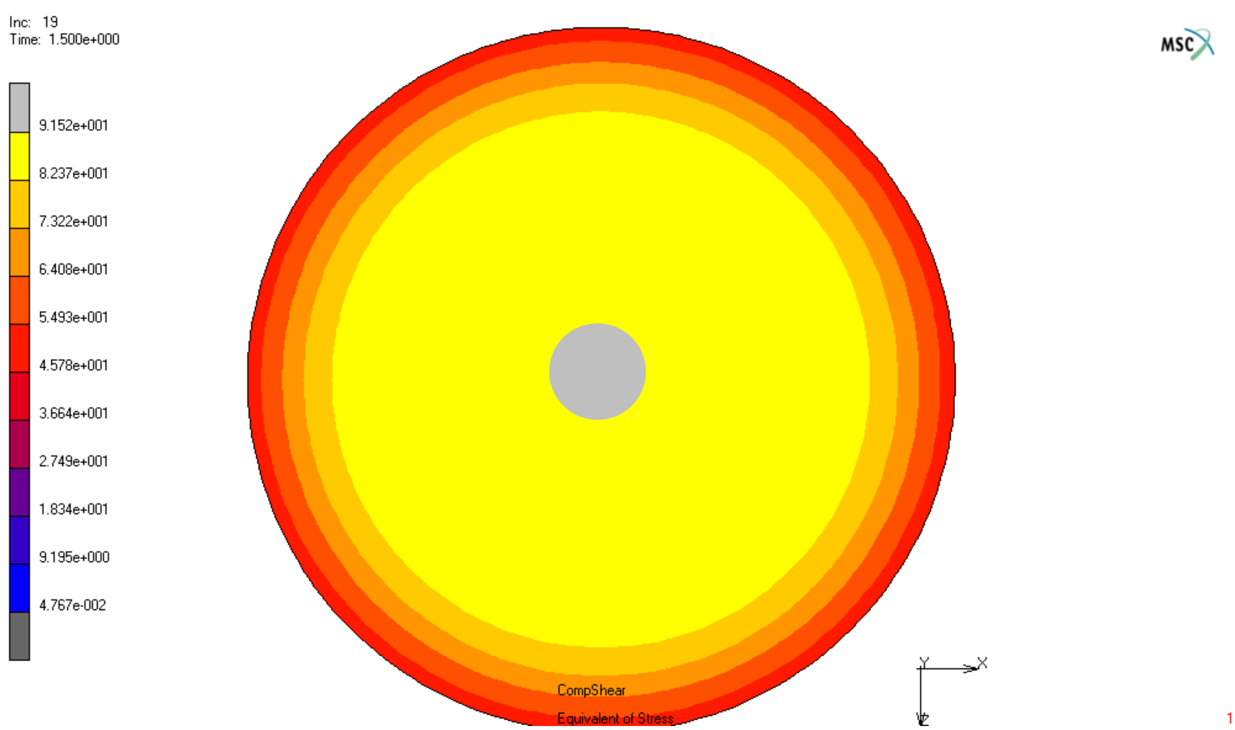

Figure 3.26 Tension contours in the fiber reinforcement (Φ=500 mm–SET1 t_f=0.07 mm S_v=3.45 MPa).

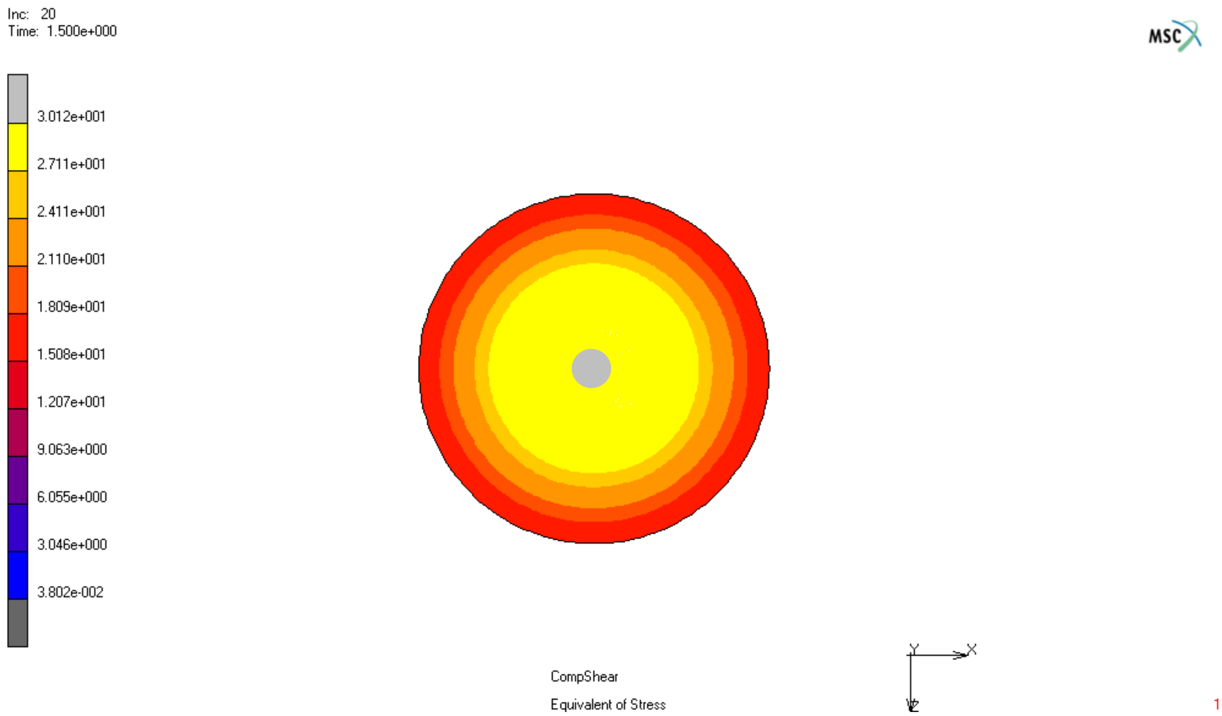

Figure 3.27 Tension contours in the fiber reinforcement (Φ=250 mm–SET2 t_f =0.25 mm S_v=3.45 MPa).

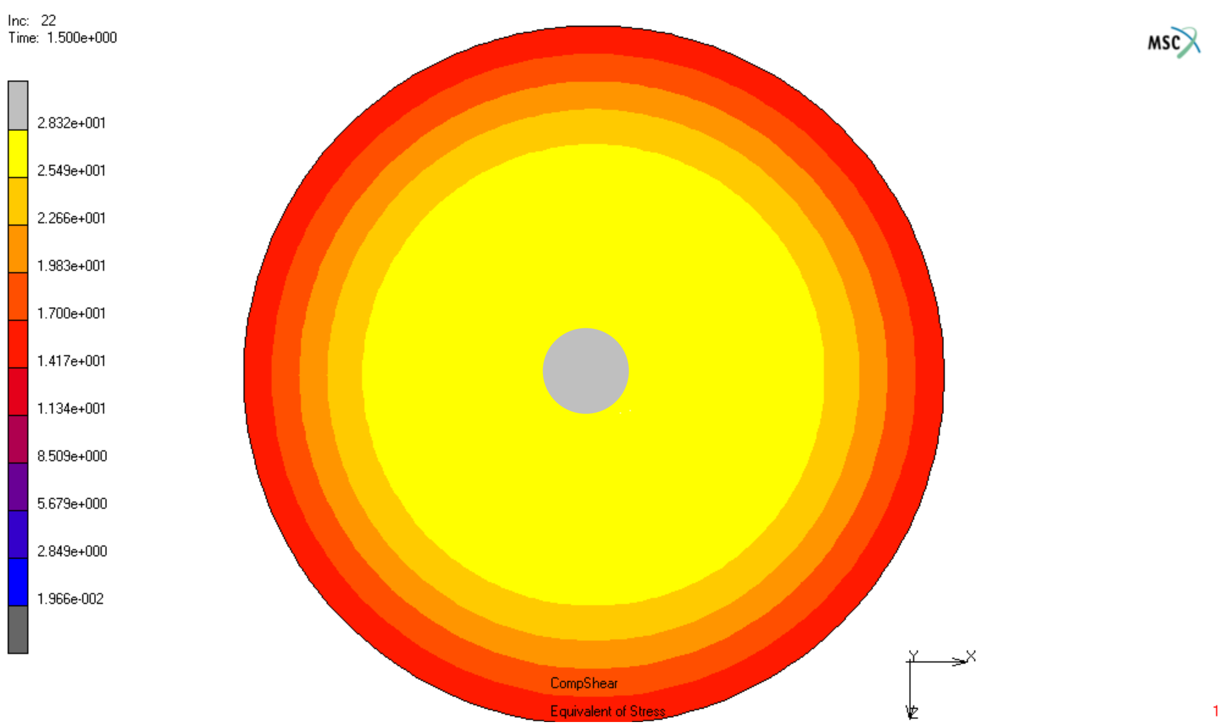

Figure 3.28 Tension contours in the fiber reinforcement (Φ=500 mm–SET2 t_f =0.25 mm S_v =3.45 MPa).

Recalling Section 2.2, we can determine the vertical stiffness of the bearing, K_V , as

$$K_V = \left(E_c A\right)/t_r \tag{3.18}$$

where

$$E_c = 24GS^2\left(1+\nu\right)\frac{\left[I_0\left(\lambda\right)-\frac{2}{\lambda}I_1\left(\lambda\right)\right]}{\alpha^2\left[I_0\left(\lambda\right)-\frac{1-\nu}{\lambda}I_1\left(\lambda\right)\right]+\beta^2\frac{1+\nu}{2}I_0\left(\lambda\right)} \tag{3.19}$$

In which I_n , are modified Bessel functions of the first and second kind of order n , $S = \Phi/4t_r$, and

$$\alpha^2 = \frac{12\left(1-\nu^2\right)GR^2}{E_f t_f t} \tag{3.20}$$

$$\beta^2 = \frac{12GR^2}{Kt^2} \tag{3.21}$$

$$\lambda^2 = \alpha^2 + \beta^2 \tag{3.22}$$

Table 3.5 summarizes the model characteristics and the results of the pressure solution, and Figure 3.29 is a plot of the load displacement relations for the twelve bearings of different geometry/reinforcement.

The values reported in Table 3.5 are plotted in Figure 3.30 where the vertical stiffness is a function of the shape factor for the twelve bearings of different geometry/reinforcement. The gray curves refer SET1 bearings and the black curves to SET2. Continuous lines describe the pressure solution results for flexible reinforcement and the dashed lines refer to flexible reinforcement and compressibility. Continuous marked lines are the FE analysis results. The gray and the black lines refer to SET1 and SET2, respectively. The pressure solution and pressure solution + C lines are the theoretical vertical stiffness results of FRBs for incompressible and compressible materials, respectively. The FE analysis results and pressure solution outputs are in good agreement. Note that the FE analysis gives higher values of vertical stiffness because of a stiffening contribution of the hexahedric mesh.

Figure 3.31 is the plot of non-dimensional stiffness $K_{v0.25}/K_{v0.07}$ as a function of the diameter, Φ . The solid line represents the pressure solution result and the dashed line represents the FE analysis outputs. The FE analysis and pressure solution outputs are in good agreement (see Figure 3.32), although the FE analysis gives higher values of vertical stiffness because of a stiffening contribution of the hexahedral mesh. For t_f = 0.25 mm, it is evident that the ratio between the different solutions increases with increasing the nominal dimension of the device: because the compressibility of the rubber is the main quota of the deformation, it can't be neglected.

Table 3.5 Model characteristics and pressure solution results (circular bearings).

Geometrical and Mechanical Properties							
Φ	[mm]	250	300	350	400	450	500
H	[mm]			180			
t_f	[mm]			0.07 (SET1) 0.25 (SET2)			
n layers	[-]			29			
t_r	[mm]			6.37 (SET 1) 6.17 (SET 2)			
E_f	[MPa]			14000			
ν	[-]			0			
G	[MPa]			0.70			
Compression Stiffness with Flexible Reinforcement							
				SET 1			
E_c	[MPa]	50,04	52,51	54,25	55,55	56,54	57,33
K_v	[N/mm]	14218,00	21485,00	30216,00	40406,00	52055,00	65162,00
				SET 2			
E_c	[MPa]	142,04	158,64	171,00	180,39	187,73	193,56
K_v	[N/mm]	40362,00	64914,00	95235,00	131220,00	172830,00	220000,00
Flexible Reinforcement and Compressibility							
				SET 1(K=2000MPa)			
E_c	[MPa]	48,56	50,92	52,58	53,82	54,77	55,53
K_v	[N/mm]	13799,00	20835,00	29286,00	39151,00	50428,00	63116,00
				SET 2			
E_c	[MPa]	130,42	144,51	154,93	162,85	169,03	173,96
K_v	[N/mm]	37059,00	59130,00	86287,00	118460,00	155620,00	197730,00

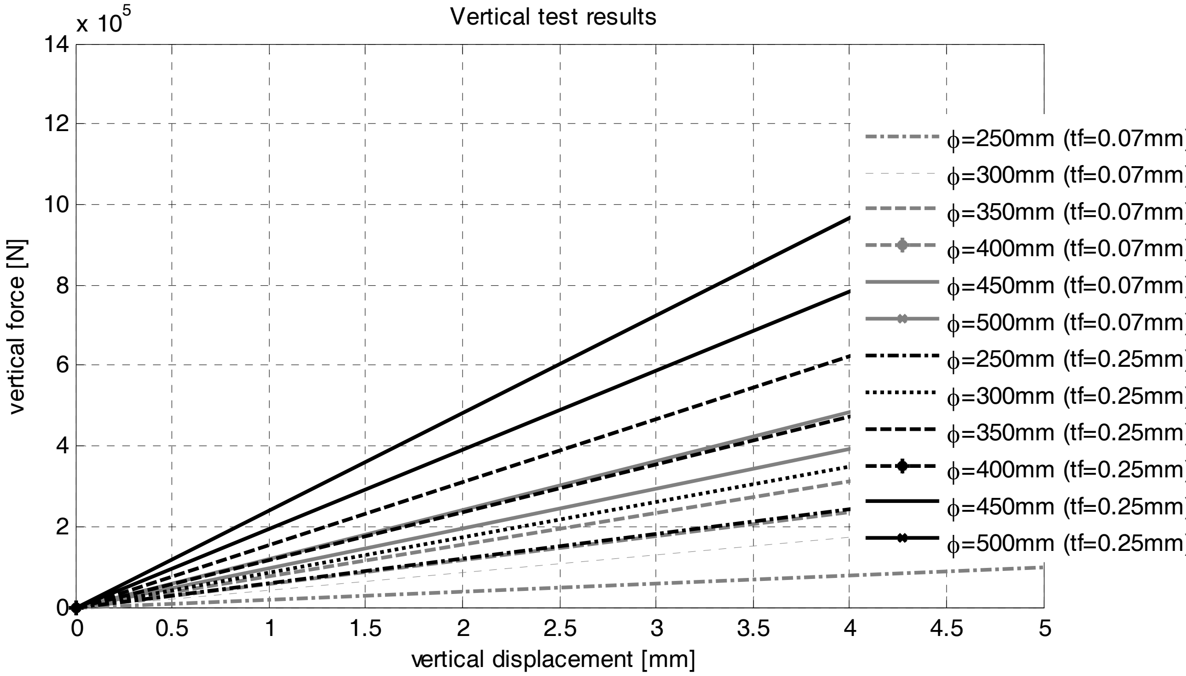

Figure 3.29 Vertical test results (FE analysis versus pressure solution).

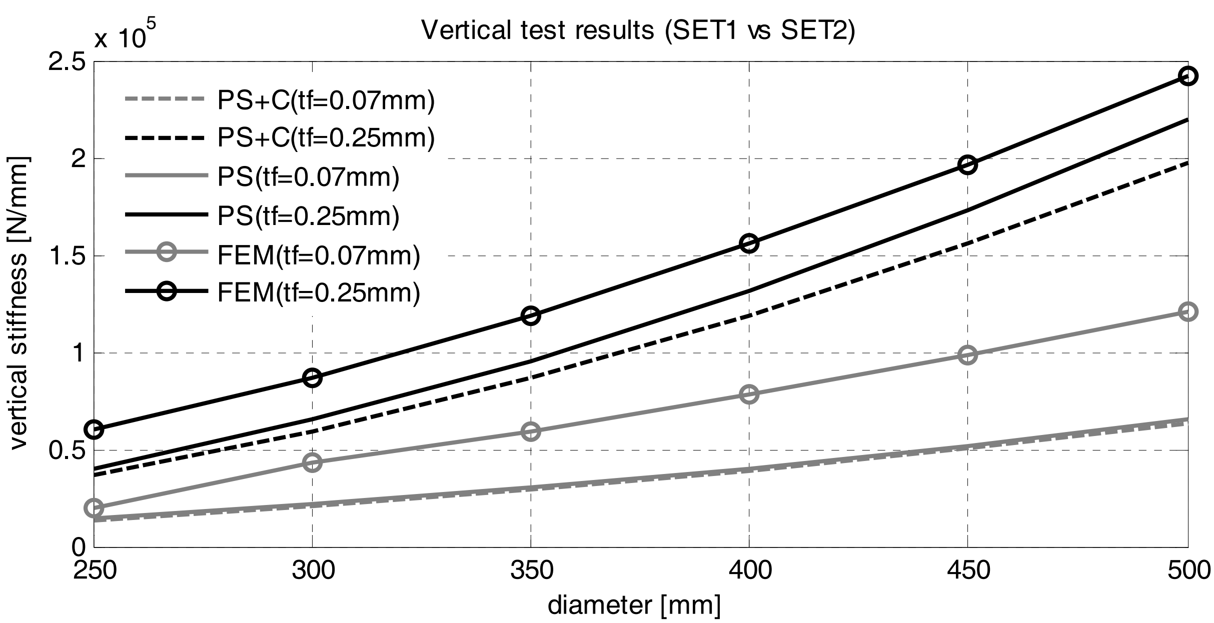

Figure 3.30 Vertical stiffness results.

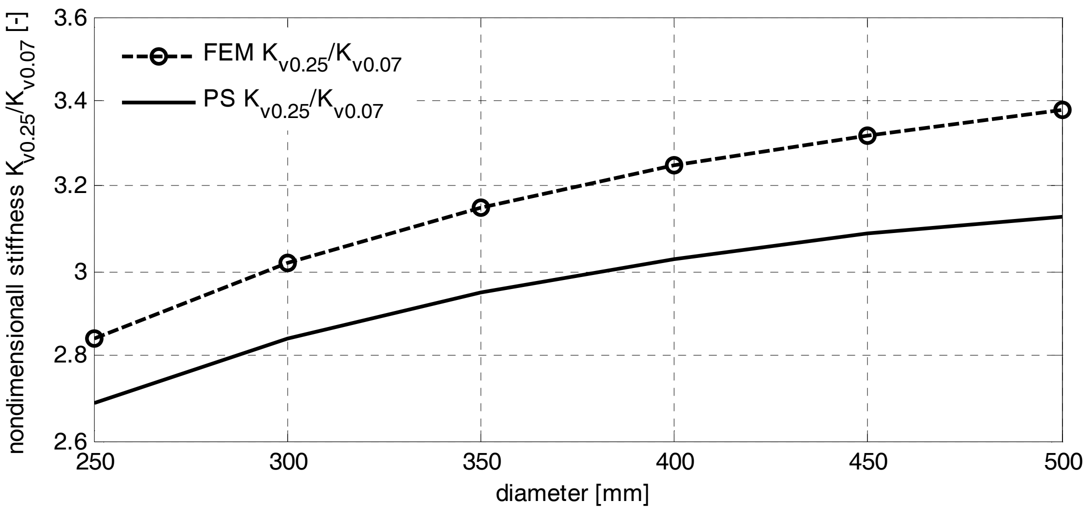

Figure 3.31 Non-dimensional stiffness versus diameter.

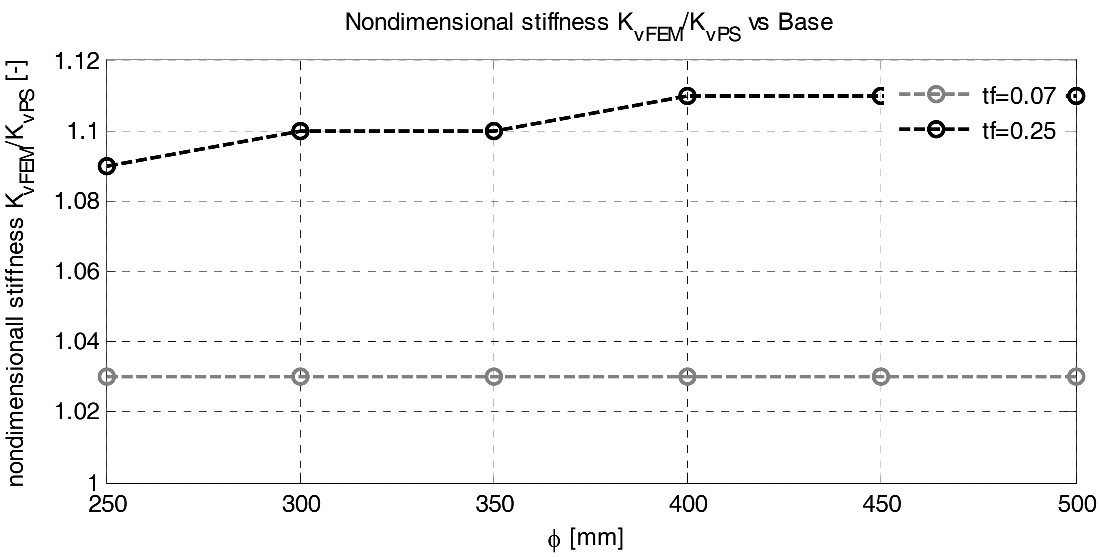

Figure 3.32 K_{vFEM}/K_{vPS} **as a function of the diameter.**

3.4 SQUARE BEARINGS

3.4.1 Geometrical Properties

Finite element models of square type FRBs with different shape factors are defined (S=B/4t_r=10.87; 13.04; 15.22; 17.39; 19.57; 21.74). The different values of the shape factor are obtained by increasing the values of the base of the device (B = 250; 300; 350; 400; 450; 500 mm). As shown in Figure 3.32, each device is made of twenty-eight rubber layers with twenty-nine interleaf fiber sheets. Each rubber layer is ~5.7 mm thick (=t_r), and each fiber sheet is 0.07 mm (=t_f) thick for SET1 and 0.25 mm thick for SET2. Figure 3.33 shows a cross section of the model of the square-type FRB investigated in this study. The geometrical characteristics are shown in Table 3.4.

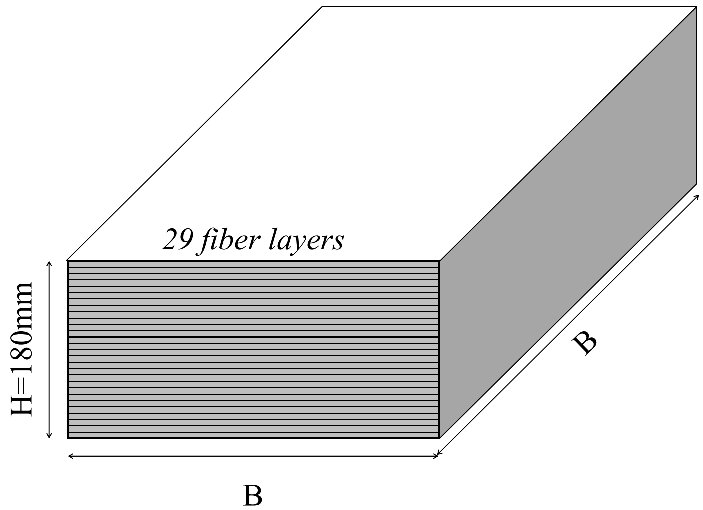

Figure 3.33 Square type bearing showing reinforcements and dimensions.

Table 3.6 Geometrical properties of the square bearings.

B [mm]	H [mm]	t_r [mm]	t_f [mm]	S [-]
500	180	5.75	0.07 (SET1) 0.25 (SET2)	21.74
450				19.57
400				17.39
350				15.22
300				13.04
250				10.87

The finite element discretization is shown in Figure 3.34. As assumed in the pressure solution, the FE models assumes there is no friction between the rubber and the top and bottom surfaces, and the bearings are loaded in pure compression only. Because there isn't any friction, each layer of the bearing deforms equally under compression, and it is sufficient to model only a single layer of the device to fully describe the behavior of the bearing. For the specific load condition, the model is doubly-symmetric: the symmetry with respect two orthogonal planes will be applied as boundary condition. The three-dimensional mesh consists of eight-node, isoparametric, three-dimensional brick elements with trilinear interpolation (element type 84). Four layers of elements were used through the thickness, and the size of the mesh along the base was chosen to have ratio of distortion next to one.

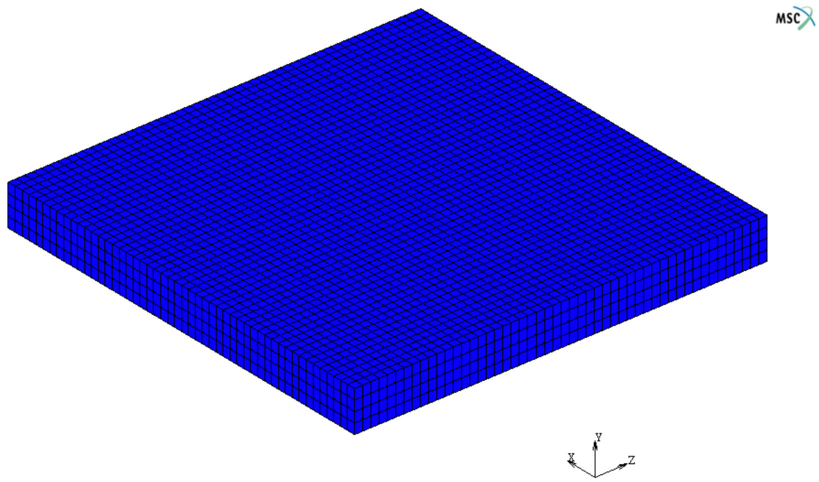

Figure 3.34 Model mesh for a single pad (element type 84).

3.4.2 Compression Results

The results from FE analysis can be compared to the results of the pressure solution. Recalling Section 2.3, we can determine the vertical stiffness of the bearing, K_V , as

$$K_V = \left(E_c A\right)/t_r \tag{3.23}$$

where

$$E_c = \frac{96GS^2}{\pi^2\left(\alpha a\right)^2}\sum_{n=1}^{\infty}\frac{2}{\left(n-1/2\right)^2}\left(\frac{\tanh\gamma_n a}{\gamma_n a}-\frac{\tanh\beta_n a}{\beta_n a}\right) \tag{3.24}$$

$$\alpha = \sqrt{\frac{12G\left(1-\nu^2\right)}{E_f t_f t}} \tag{3.25}$$

$$\gamma_n = \left(n-\frac{1}{2}\right)\frac{\pi}{a} \tag{3.26}$$

$$\beta_n = \sqrt{\gamma_n^2+\alpha^2} \tag{3.27}$$

The previous formula are referred to the hypothesis of incompressibility of the rubber. Table 3.7 summarizes the model characteristics and the pressure solution results for square type bearings. The values reported in the Table 3.7 are plotted in Figure 3.3.6 and Figure 3.37. For the considered range of bases (eq. shape factors), the vertical stiffness is linear with respect to the shape factor. Figure 3.35 is a plot of the vertical test results.

Table 3.7 Model characteristics and pressure solution results (square bearings).

Geometrical and Mechanical Properties							
B	[mm]	250	300	350	400	450	500
H	[mm]	180					
t_f	[mm]	0.07 (SET1) 0.25 (SET2)					
n layers	[-]	29					
t_r	[mm]	6.37 (SET 1) 6.17 (SET 2)					
E_f	[MPa]	14000					
G	[MPa]	0.70					
Compression Stiffness with Flexible Reinforcement							
SET 1							
α	[-]	0.02					
$E_{c\,(n=9)}$	[MPa]	120.60	126.19	130.19	133.19	135.52	137.39
SET 2							
α	[-]	0.04					
$E_{c\,(n=9)}$	[MPa]	340.49	376.57	403.26	423.59	439.49	452.25

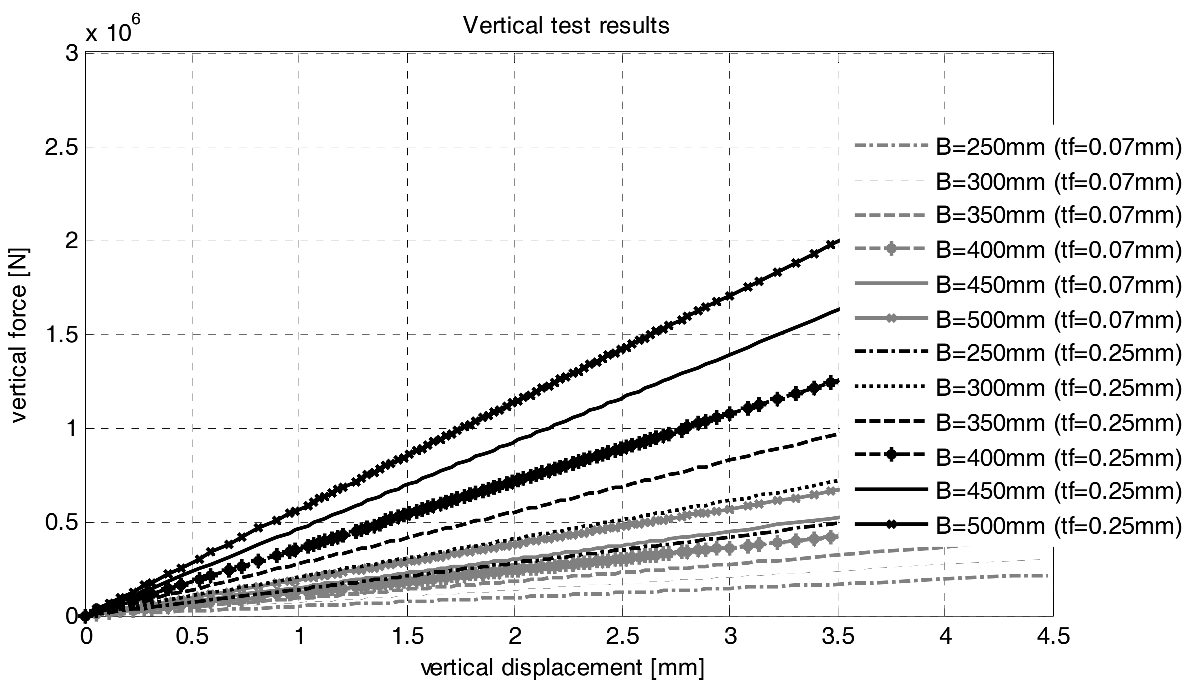

Figure 3.35 Vertical force–vertical displacement.

Figure 3.36 is a plot of the vertical stiffness as a function of the base (eq. shape factor) for the twelve bearings of different geometry/reinforcement. The gray lines refer to t_f = 0.07 mm (SET1) while the black lines refer to t_f = 0.25 mm (SET2). In each figure the solid lines represent the pressure solution results, and the lines with markers represent the FE analysis results. Figure 3.37 is a plot of the non-dimensional vertical stiffness (FE model/pressure solution) as a function of the base. Figure 3.38 is a plot of the non-dimensional vertical stiffness (FE model/pressure solution) as a function of the base/diameter for the square and the circular bearings.

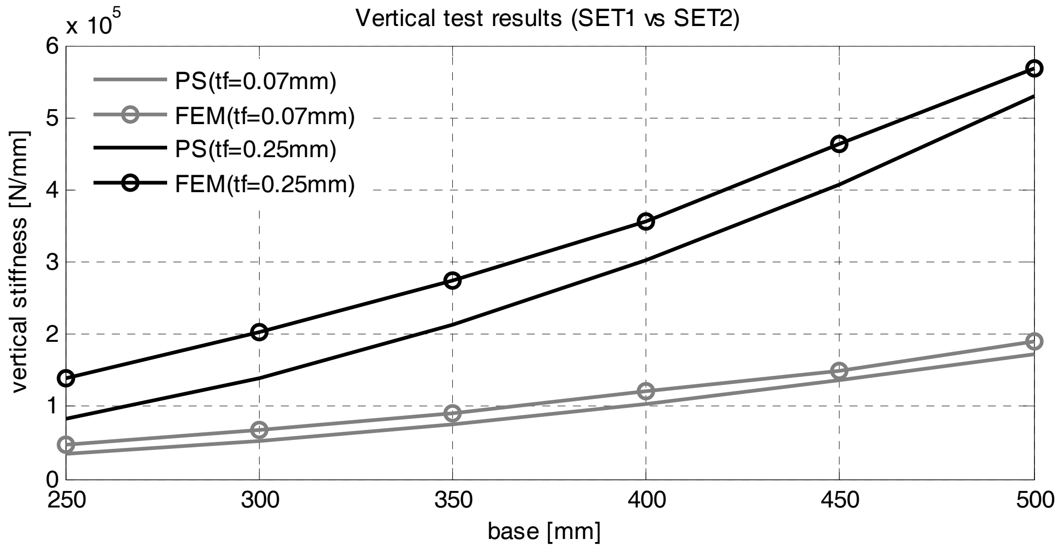

Figure 3.36 Vertical stiffness versus base.

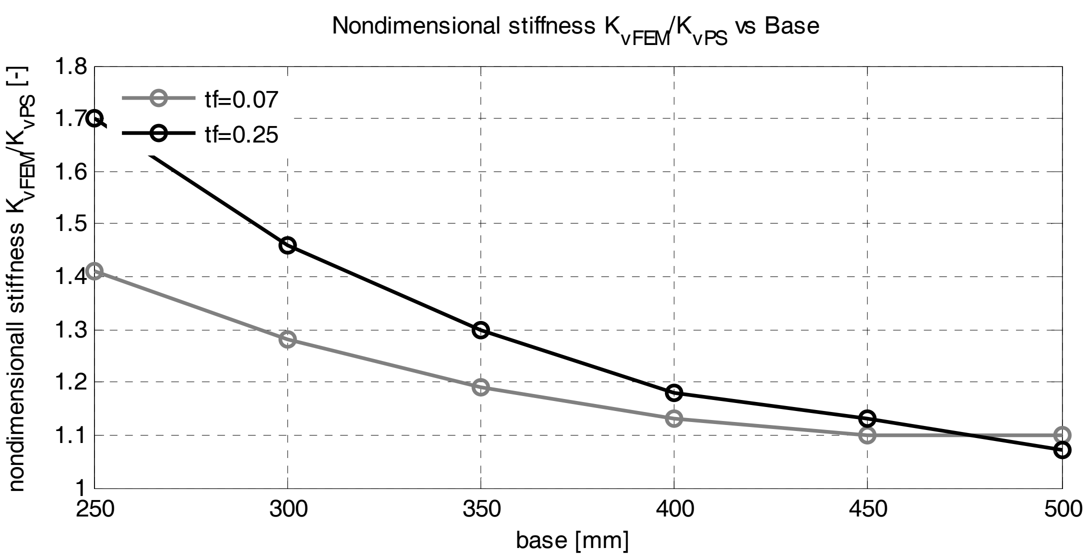

Figure 3.37 K_{vFEM}/K_{vPS} **as a function of the base.**

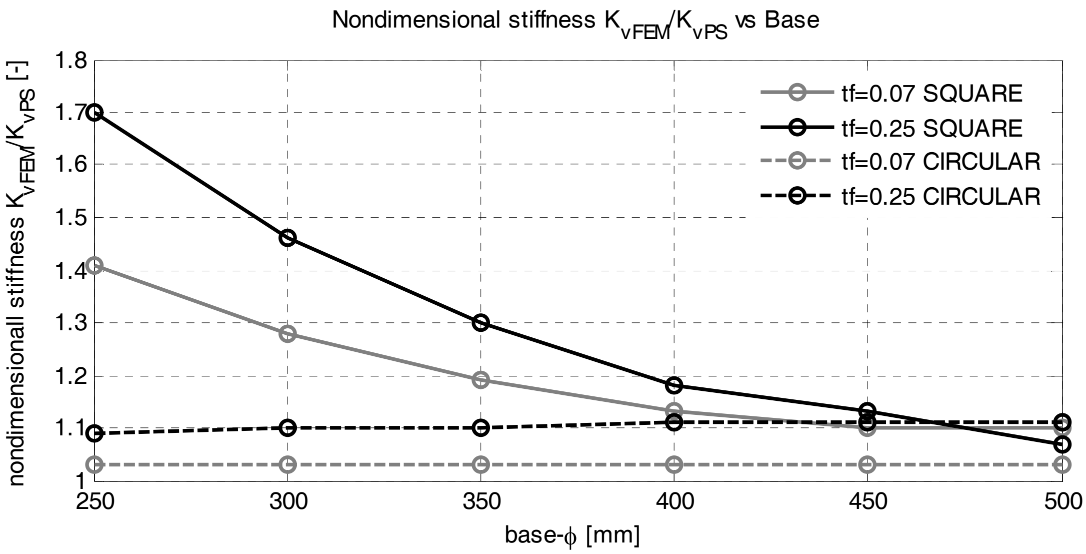

Figure 3.38 K_{vFEM}/K_{vPS} **as a function of the base-diameter for square and circular bearings.**

4 Ultimate Displacement and Stability of Unbonded Bearings

4.1 INTRODUCTION

The most important aspects of FRBs are that they do not have thick end plates, they are not bonded to the top and bottom support surfaces, and their reinforcements are flexible. These features at first sight might seem to be deficiencies of their design, but they have the advantage of eliminating the presence of tensile stresses in the bearing by allowing it to roll off the supports. This reduces the costly stringent bonding requirements that are typical for conventional bearings. The FRBs can deform without damage if displacements of seismic magnitude are applied because the top and bottom surfaces can roll off the support surfaces and no tension stresses are produced. The unbalanced moments are resisted by the vertical load through offset of the force resultants on the top and bottom surfaces. In conventional bonded bearings, the compression is carried through the overlap region between top and bottom surfaces, and the unbalanced moment is carried by tension stresses in the regions outside the overlap Figure 4.1. In unbonded FRB, the moment created by the offset of the resultant compressive loads, *P*, balances the moment created by the shear, *V*, as shown in Figure 4.2.

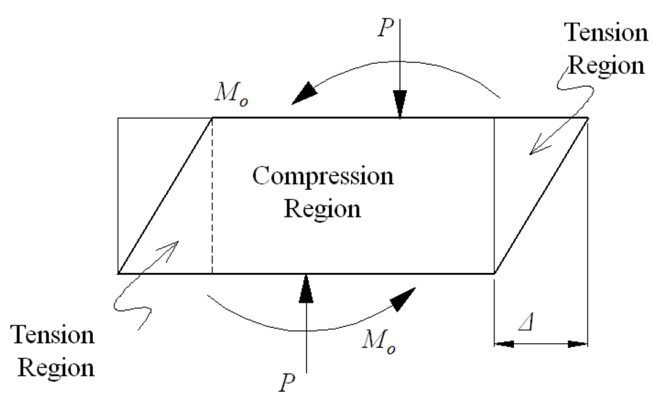

Figure 4.1 Bonded bearing under compression and shear.

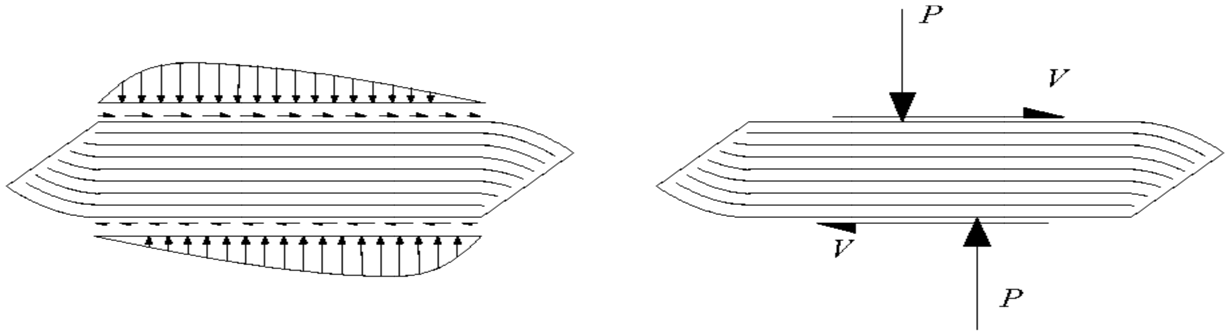

Figure 4.2 Normal and shear stress distributions on the top and bottom faces of the unbonded bearing in its deformed shape.

4.2 LIMITING DISPLACEMENT CRITERIA

In this section two limiting displacement criteria are introduced:

- overall stability
- no contact with horizontal subgrade

The overall stability represents the displacement at which the peak value of horizontal forces is reached in the horizontal load-displacement path. After the peak is reached, the bearing can be displaced further. Experimental results [Kelly 1999] demonstrated that the roll-off response is limited by the fact that the free edge of the bearing rotates from the vertical towards the horizontal with increasing shear displacement. The limit of this process is reached when the originally vertical surfaces at each side come in contact with the horizontal surfaces at both top and bottom. Further horizontal displacement beyond this point can only be achieved by slip. The friction coefficient between rubber and other surfaces often can take very large values, possibly as high as one, and slip can produce damage to the bearing through tearing of the surface and heat generated by the sliding motion.

4.2.1 Stability of Horizontal Displacement

The basic assumption for the behavior of these bearings under horizontal displacement is that the areas of the roll-off are free of stress and the area below the contact region has constant shear stress, as shown in Figure 4.3. The basic premise for the analysis of these bearings is that the regions of the bearing that have rolled off the rigid supports are free of all stress, and that the volume under the contact area has constant shear stress. Under this assumption, the active area that produces the force of resistance F to displacement Δ is $B-\Delta$, and thus the force (per unit width of the bearing) is $F = G\gamma\left(B-\Delta\right)$, but $\gamma = \Delta / t_r$, thus $F = G\left(B-\Delta\right)\Delta / t_r$. Consequently, the force displacement curve has zero slope when

$$\frac{dF}{d\Delta} = \frac{G}{t_r}\left(B-2\Delta\right) = 0, \quad \text{i.e., when } \Delta = B/2 \tag{4.1}$$

implying that the bearing remains stable in the sense of positive tangential force-displacement relationship so long as the displacement is less than half the length in the direction of the displacement. As a result of the limiting displacement analysis, it is possible to determine a simple design criterion for this type of bearing. We need only to determine a maximum required design displacement that normally would depend on the site, the anticipated isolation period, and damping. If we denote this by Δ, then the requirement for positive incremental horizontal stiffness requires that the width B of the bearing in the direction of the displacement be at least twice the displacement, i.e., $B \geq 2\Delta$.

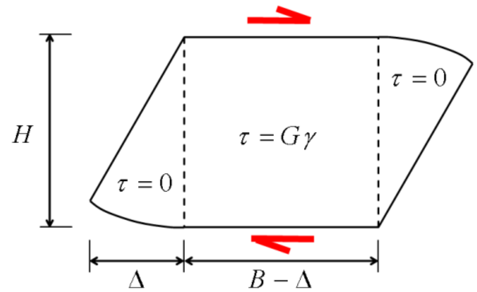

Figure 4.3 Unbonded bearing under shear load.

4.2.2 No Contact with Horizontal Subgrade

In FRBs, the fiber sheets are much more flexible compared to the steel reinforcing in current designs of building isolators. Under horizontal load this flexibility allows the unbonded surfaces to roll off the loading surfaces. Thus the maximum displacement for a bearing of this type can be specified as that which transforms the vertical free edge to a horizontal plane. In the normal situation, where the bearing thickness is small in comparison to the plan dimension in the direction of loading, this can be estimated by studying only the deformation of one side and neglecting the interaction between the deformations at each end.

The basic assumptions used to predict the limiting shear deformation are

- the material is incompressible
- the plates are completely flexible
- the free surface of the roll-off portion is stress free

The first two are reasonable for the elastomer and reinforcement of these bearings, and the third means that the displacement when the vertical surface touches the horizontal support is the length of the curved arc of the free surface.

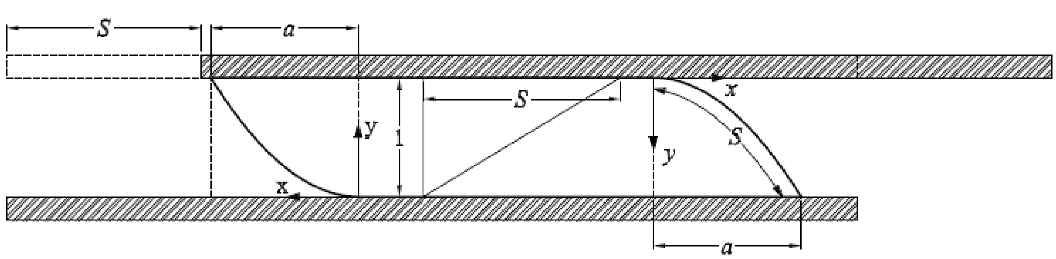

Figure 4.4 Schematic of the deformed bearing.

The geometry assumed in the derivation is shown in Figure 4.4. The thickness of the bearing is one, and the horizontal projection of the curved free surface is *a*. Assuming that the curved free surface *S* is a parabolic arc, then in the coordinate system x, y shown in the figure, the curved surface is given by

$$y = \frac{x^2}{a^2}; \quad x = ay^{1/2} \tag{4.2}$$

The area of the region enclosed by the curved arc of length S is

$$A = \int_0^1 dy \int_0^{ay^{1/2}} dx = \int_0^1 ay^{1/2} dy = \frac{2}{3} a \tag{4.3}$$

The requirement of incompressibility means that the volume before deformation and after are preserved, thus

$$\frac{1}{2} S = \frac{2}{3} a, \quad \text{or} \quad a = \frac{3}{4} S \tag{4.4}$$

The curved arc length S is given by

$$dS = \left(dx^2 + dy^2 \right)^{1/2} \tag{4.5}$$

where

$$dy = \frac{2xdx}{a^2} \tag{4.6}$$

And

$$S = \int_0^a \left(1 + \frac{4x^2}{a^4} \right)^{1/2} dx \tag{4.7}$$

Using the change of variable $u = 2x / a^2$ and $du = 2 / a^2 dx$, we have

$$S = \frac{a^2}{2} \int_0^{2/a} \left(1 + u^2 \right)^{1/2} du \tag{4.8}$$

Let $u = \sinh(t)$. Then

$$S = \frac{a^2}{2} \int_0^{\operatorname{arcsinh}(2/a)} \cosh(t)^2 \, dt \tag{4.9}$$

Since $\cosh(t)^2 = 1/2 \left(\cosh(2t) + 1 \right)$, this leads to

$$S = \frac{a^2}{4} \left[\sinh(t) \cosh(t) + t \right]_0^{\operatorname{arcsinh}(2/a)} \tag{4.10}$$

and with $\cosh(t) = \left(1 + \sinh(t)^2 \right)^{1/2}$, we have

$$S = \frac{a^2}{4}\left[\frac{2}{a}\left(1+\frac{4}{a^2}\right)^{1/2} + \operatorname{arcsinh}\left(\frac{2}{a}\right)\right] \tag{4.11}$$

The incompressibility condition requires that $S = 4a/3$ leading to an equation for a in the form

$$\operatorname{arcsinh}\left(\frac{2}{a}\right) = \frac{16}{3a} - \frac{2}{a}\left(1+\frac{4}{a^2}\right)^{1/2} \tag{4.12}$$

Replacing $2/a$ by t and inverting the equation leads to a transcendental equation for t in the form

$$t = \sinh\left[\left(\frac{8}{3} - \left(1+t^2\right)^{1/2}\right)t\right] \tag{4.13}$$

which after solving for t gives a and in turn S. The solution to a high degree of accuracy is $t = 1.60$, $a = 1.25$ and $S = 1.67$. This is the overall shear strain. The conclusion is that in broad terms these bearings can experience a displacement equal to the thickness of the rubber before they run the risk of damage by sliding.

The shear tests conducted in Marc for the different bearings show that the peak horizontal displacement is approximately half of the base length. The theoretical model, which used to determine the peak horizontal displacement, gives good results even when compared against the FE analysis with non-zero vertical load. Note that for a fixed axial load, the shear load goes through a maximum as the shear deflection is further increased. The displacement at which this maximum occurs decreases with increasing axial load. Therefore, it can be concluded that further FE analysis are necessary to precisely evaluate the influence of the vertical load on the horizontal behavior of the bearings. Moreover, this study was conducted considering the shape factor, S, as the only variable. Analytical results showed that although shape factor is an important geometrical parameter that characterizes the mechanics of the bearings; there are other parameters—such as the slenderness of the bearing—that should be taken into account to fully describe the global behavior of the device.

5 Conclusions

Many large urban centers are extremely vulnerable to the damaging effects of large earthquakes. For example, large cities such as Istanbul and Tehran have many thousands of buildings that were built prior to the enforcement of stringent building codes. Buildings in the range of two to six stories have been constructed using only vertical load designs and no provision for horizontal resistance. These are in many cases valuable buildings and are used as residences, offices, and shops. There are so many of them that they cannot realistically be demolished and replaced, and retrofitting them by conventional methods would be highly disruptive to occupants. Development of low-cost seismic isolators that can be mass produced by a relatively simplified manufacturing process would stimulate world-wide application of the seismic isolation technology to the retrofit of existing structures with deficiencies and to new construction in lesser developed countries.

Modern methods of structural control would be much too expensive for these buildings, but it is possible that a system of inexpensive seismic isolation could be adapted to improve the seismic resistance of poor housing and other buildings such as schools and hospitals. In at least one retrofit project in Armenia, a large multi-family housing block was retrofitted using rubber isolators with no need for the families to leave while the work was done.

This report has described a potential approach to the provision of a low-cost, light-weight rubber isolation systems. It has been extensively tested in laboratory test program and a theoretical analysis of the mechanical behavior of this type of isolator has also been verified in this report by finite element studies. These isolators have much less severe bonding requirements than conventional isolators and have the potential of lending themselves to mass production manufacturing, which will be required for any type of retrofit of vulnerable buildings in the urban environment.

The most important aspects of these bearings are that they do not have thick end plates, they are not bonded to the top and bottom support surfaces, and their reinforcement is very flexible. At first sight this might seem to be a deficiency of their design, but in fact it has the advantage that it eliminates the presence of tensile stresses in the bearing by allowing it to roll off the supports. This reduces the costly stringent bonding requirements that are typical for conventional bearings. The weight and the cost of isolators is reduced by using fiber reinforcement, no end-plates, and no bonding to the support surfaces, thereby offering a low-cost light-weight isolation system for retrofit in large cities such as Tehran and Istanbul, and also for new housing and public buildings in developing countries.

REFERENCES

Chalhoub MS, Kelly JM (1986). Reduction of the stiffness of rubber bearings due to compressibility, *Rept. No. UCB/SESM-86/06*, Department of Civil Engineering, University of California, Berkeley, CA.

Gent AN, Lindley PB (1959). Compression of bounded rubber blocks, *Proceedings*, Institution of Mechanical Engineers, 173(3):111−122.

Gent AN, Meinecke EA (1970). Compression, bending and shear of bonded rubber blocks, *Polymer Engrg., Sci.*,10 (1):48−53.

Kelly JM (1982). Aseismic base isolation, *Shock and Vibration Digest*, 14(5):17–25.

Kelly JM (1997). *Earthquake-resistant Design with Rubber*, 2nd ed., Springer-Verlag, London.

Kelly JM (1999). Analysis of fiber-reinforced elastomeric isolator, *J. Seismol. Earthq. Engrg*., 2:19–34.

Kelly JM, Takhirov SM (2002). Analytical and experimental study of fiber-reinforced bearings, *Rept. No. 2002/11*, Pacific Earthquake Engineering Research Center, University of California, Berkeley, CA.

MSC Software (2000). *Nonlinear Finite Element Analysis of Elastomers*, White Paper. Santa Ana, CA.

MSC Software (2004). MSC Marc 2005 and MSC Marc Mentat 2005, Santa Ana, CA.

Rocard Y (1973). Note sur le calcul des proprietes elastique des supports en caoutchouc adherent, *J. Phys. Radium*, 8:197–203.

Seky W, Fukahori Y, Iseda Y, Matsunaga T (1987). A large deformation finite element analysis for multilayer elastomeric bearings, *Rubber Chem. Tech*., 60:856−869.

Simo JC, Kelly JM (1984). Finite element analysis of the stability of multilayer elastomeric bearings, *Engrg Struct*., 6(3):162−174.

Takayama M, Tada H, Tanaka R (1994). Finite element analysis of laminated rubber bearings used in base-isolation system, *Rubber Chem. Tech*.,65:46−62.

Tsai H-C, Kelly JM (2001). Stiffness analysis of fiber reinforced elastomeric isolators, *Rept. No. 2001/05*, Pacific Earthquake Engineering Research Center, University of California, Berkeley, CA.

PEER REPORTS

PEER reports are available individually or by yearly subscription. PEER reports can be ordered at http://peer.berkeley.edu/publications/peer_reports.html or by contacting the Pacific Earthquake Engineering Research Center, 325 Davis Hall mail code 1792, Berkeley, CA 94720. Tel.: (510) 642-3437; Fax: (510) 665-1655; Email: peer_editor@berkeley.edu

PEER 2011/10 *Earthquake Engineering for Resilient Communities: 2011 PEER Internship Program Research Report Collection.* Eds. Heidi Faison and Stephen A. Mahin. December 2011.

PEER 2011/09 *Calibration of Semi-Stochastic Procedure for Simulating High-Frequency Ground Motions.* Jonathan P. Stewart, Emel Seyhan, and Robert W. Graves. December 2011.

PEER 2011/08 *Water Supply in regard to Fire Following Earthquake.* Charles Scawthorn. November 2011.

PEER 2011/07 *Seismic Risk Management in Urban Areas. Proceedings of a U.S.-Iran-Turkey Seismic Workshop.* September 2011.

PEER 2011/06 *The Use of Base Isolation Systems to Achieve Complex Seismic Performance Objectives.* Troy A. Morgan and Stephen A. Mahin. July 2011.

PEER 2011/05 *Case Studies of the Seismic Performance of Tall Buildings Designed by Alternative Means.* Task 12 Report for the Tall Buildings Initiative. Jack Moehle, Yousef Bozorgnia, Nirmal Jayaram, Pierson Jones, Mohsen Rahnama, Nilesh Shome, Zeynep Tuna, John Wallace, Tony Yang, and Farzin Zareian. July 2011.

PEER 2011/04 *Recommended Design Practice for Pile Foundations in Laterally Spreading Ground.* Scott A. Ashford, Ross W. Boulanger, and Scott J. Brandenberg. June 2011.

PEER 2011/03 *New Ground Motion Selection Procedures and Selected Motions for the PEER Transportation Research Program.* Jack W. Baker, Ting Lin, Shrey K. Shahi, and Nirmal Jayaram. March 2011.

PEER 2011/02 *A Bayesian Network Methodology for Infrastructure Seismic Risk Assessment and Decision Support.* Michelle T. Bensi, Armen Der Kiureghian, and Daniel Straub. March 2011.

PEER 2011/01 *Demand Fragility Surfaces for Bridges in Liquefied and Laterally Spreading Ground.* Scott J. Brandenberg, Jian Zhang, Pirooz Kashighandi, Yili Huo, and Minxing Zhao. March 2011.

PEER 2010/05 *Guidelines for Performance-Based Seismic Design of Tall Buildings.* Developed by the Tall Buildings Initiative. November 2010.

PEER 2010/04 *Application Guide for the Design of Flexible and Rigid Bus Connections between Substation Equipment Subjected to Earthquakes.* Jean-Bernard Dastous and Armen Der Kiureghian. September 2010.

PEER 2010/03 *Shear Wave Velocity as a Statistical Function of Standard Penetration Test Resistance and Vertical Effective Stress at Caltrans Bridge Sites.* Scott J. Brandenberg, Naresh Bellana, and Thomas Shantz. June 2010.

PEER 2010/02 *Stochastic Modeling and Simulation of Ground Motions for Performance-Based Earthquake Engineering.* Sanaz Rezaeian and Armen Der Kiureghian. June 2010.

PEER 2010/01 *Structural Response and Cost Characterization of Bridge Construction Using Seismic Performance Enhancement Strategies.* Ady Aviram, Božidar Stojadinović, Gustavo J. Parra-Montesinos, and Kevin R. Mackie. March 2010.

PEER 2009/03 *The Integration of Experimental and Simulation Data in the Study of Reinforced Concrete Bridge Systems Including Soil-Foundation-Structure Interaction.* Matthew Dryden and Gregory L. Fenves. November 2009.

PEER 2009/02 *Improving Earthquake Mitigation through Innovations and Applications in Seismic Science, Engineering, Communication, and Response. Proceedings of a U.S.-Iran Seismic Workshop.* October 2009.

PEER 2009/01 *Evaluation of Ground Motion Selection and Modification Methods: Predicting Median Interstory Drift Response of Buildings.* Curt B. Haselton, Ed. June 2009.

PEER 2008/10 *Technical Manual for Strata.* Albert R. Kottke and Ellen M. Rathje. February 2009.

PEER 2008/09 *NGA Model for Average Horizontal Component of Peak Ground Motion and Response Spectra.* Brian S.-J. Chiou and Robert R. Youngs. November 2008.

PEER 2008/08 *Toward Earthquake-Resistant Design of Concentrically Braced Steel Structures.* Patxi Uriz and Stephen A. Mahin. November 2008.

PEER 2008/07 *Using OpenSees for Performance-Based Evaluation of Bridges on Liquefiable Soils.* Stephen L. Kramer, Pedro Arduino, and HyungSuk Shin. November 2008.

PEER 2008/06 *Shaking Table Tests and Numerical Investigation of Self-Centering Reinforced Concrete Bridge Columns.* Hyung IL Jeong, Junichi Sakai, and Stephen A. Mahin. September 2008.

PEER 2008/05 *Performance-Based Earthquake Engineering Design Evaluation Procedure for Bridge Foundations Undergoing Liquefaction-Induced Lateral Ground Displacement.* Christian A. Ledezma and Jonathan D. Bray. August 2008.

PEER 2008/04 *Benchmarking of Nonlinear Geotechnical Ground Response Analysis Procedures.* Jonathan P. Stewart, Annie On-Lei Kwok, Yousseff M. A. Hashash, Neven Matasovic, Robert Pyke, Zhiliang Wang, and Zhaohui Yang. August 2008.

PEER 2008/03 *Guidelines for Nonlinear Analysis of Bridge Structures in California.* Ady Aviram, Kevin R. Mackie, and Božidar Stojadinović. August 2008.

PEER 2008/02 *Treatment of Uncertainties in Seismic-Risk Analysis of Transportation Systems.* Evangelos Stergiou and Anne S. Kiremidjian. July 2008.

PEER 2008/01 *Seismic Performance Objectives for Tall Buildings.* William T. Holmes, Charles Kircher, William Petak, and Nabih Youssef. August 2008.

PEER 2007/12 *An Assessment to Benchmark the Seismic Performance of a Code-Conforming Reinforced Concrete Moment-Frame Building.* Curt Haselton, Christine A. Goulet, Judith Mitrani-Reiser, James L. Beck, Gregory G. Deierlein, Keith A. Porter, Jonathan P. Stewart, and Ertugrul Taciroglu. August 2008.

PEER 2007/11 *Bar Buckling in Reinforced Concrete Bridge Columns.* Wayne A. Brown, Dawn E. Lehman, and John F. Stanton. February 2008.

PEER 2007/10 *Computational Modeling of Progressive Collapse in Reinforced Concrete Frame Structures.* Mohamed M. Talaat and Khalid M. Mosalam. May 2008.

PEER 2007/09 *Integrated Probabilistic Performance-Based Evaluation of Benchmark Reinforced Concrete Bridges.* Kevin R. Mackie, John-Michael Wong, and Božidar Stojadinović. January 2008.

PEER 2007/08 *Assessing Seismic Collapse Safety of Modern Reinforced Concrete Moment-Frame Buildings.* Curt B. Haselton and Gregory G. Deierlein. February 2008.

PEER 2007/07 *Performance Modeling Strategies for Modern Reinforced Concrete Bridge Columns.* Michael P. Berry and Marc O. Eberhard. April 2008.

PEER 2007/06 *Development of Improved Procedures for Seismic Design of Buried and Partially Buried Structures.* Linda Al Atik and Nicholas Sitar. June 2007.

PEER 2007/05 *Uncertainty and Correlation in Seismic Risk Assessment of Transportation Systems.* Renee G. Lee and Anne S. Kiremidjian. July 2007.

PEER 2007/04 *Numerical Models for Analysis and Performance-Based Design of Shallow Foundations Subjected to Seismic Loading.* Sivapalan Gajan, Tara C. Hutchinson, Bruce L. Kutter, Prishati Raychowdhury, José A. Ugalde, and Jonathan P. Stewart. May 2008.

PEER 2007/03 *Beam-Column Element Model Calibrated for Predicting Flexural Response Leading to Global Collapse of RC Frame Buildings.* Curt B. Haselton, Abbie B. Liel, Sarah Taylor Lange, and Gregory G. Deierlein. May 2008.

PEER 2007/02 *Campbell-Bozorgnia NGA Ground Motion Relations for the Geometric Mean Horizontal Component of Peak and Spectral Ground Motion Parameters.* Kenneth W. Campbell and Yousef Bozorgnia. May 2007.

PEER 2007/01 *Boore-Atkinson NGA Ground Motion Relations for the Geometric Mean Horizontal Component of Peak and Spectral Ground Motion Parameters.* David M. Boore and Gail M. Atkinson. May. May 2007.

PEER 2006/12 *Societal Implications of Performance-Based Earthquake Engineering.* Peter J. May. May 2007.

PEER 2006/11 *Probabilistic Seismic Demand Analysis Using Advanced Ground Motion Intensity Measures, Attenuation Relationships, and Near-Fault Effects.* Polsak Tothong and C. Allin Cornell. March 2007.

PEER 2006/10 *Application of the PEER PBEE Methodology to the I-880 Viaduct.* Sashi Kunnath. February 2007.

PEER 2006/09 *Quantifying Economic Losses from Travel Forgone Following a Large Metropolitan Earthquake.* James Moore, Sungbin Cho, Yue Yue Fan, and Stuart Werner. November 2006.

PEER 2006/08 *Vector-Valued Ground Motion Intensity Measures for Probabilistic Seismic Demand Analysis*. Jack W. Baker and C. Allin Cornell. October 2006.

PEER 2006/07 *Analytical Modeling of Reinforced Concrete Walls for Predicting Flexural and Coupled–Shear-Flexural Responses*. Kutay Orakcal, Leonardo M. Massone, and John W. Wallace. October 2006.

PEER 2006/06 *Nonlinear Analysis of a Soil-Drilled Pier System under Static and Dynamic Axial Loading.* Gang Wang and Nicholas Sitar. November 2006.

PEER 2006/05 *Advanced Seismic Assessment Guidelines.* Paolo Bazzurro, C. Allin Cornell, Charles Menun, Maziar Motahari, and Nicolas Luco. September 2006.

PEER 2006/04 *Probabilistic Seismic Evaluation of Reinforced Concrete Structural Components and Systems.* Tae Hyung Lee and Khalid M. Mosalam. August 2006.

PEER 2006/03 *Performance of Lifelines Subjected to Lateral Spreading.* Scott A. Ashford and Teerawut Juirnarongrit. July 2006.

PEER 2006/02 *Pacific Earthquake Engineering Research Center Highway Demonstration Project.* Anne Kiremidjian, James Moore, Yue Yue Fan, Nesrin Basoz, Ozgur Yazali, and Meredith Williams. April 2006.

PEER 2006/01 *Bracing Berkeley. A Guide to Seismic Safety on the UC Berkeley Campus*. Mary C. Comerio, Stephen Tobriner, and Ariane Fehrenkamp. January 2006.

PEER 2005/16 *Seismic Response and Reliability of Electrical Substation Equipment and Systems.* Junho Song, Armen Der Kiureghian, and Jerome L. Sackman. April 2006.

PEER 2005/15 *CPT-Based Probabilistic Assessment of Seismic Soil Liquefaction Initiation.* R. E. S. Moss, R. B. Seed, R. E. Kayen, J. P. Stewart, and A. Der Kiureghian. April 2006.

PEER 2005/14 *Workshop on Modeling of Nonlinear Cyclic Load-Deformation Behavior of Shallow Foundations.* Bruce L. Kutter, Geoffrey Martin, Tara Hutchinson, Chad Harden, Sivapalan Gajan, and Justin Phalen. March 2006.

PEER 2005/13 *Stochastic Characterization and Decision Bases under Time-Dependent Aftershock Risk in Performance-Based Earthquake Engineering.* Gee Liek Yeo and C. Allin Cornell. July 2005.

PEER 2005/12 *PEER Testbed Study on a Laboratory Building: Exercising Seismic Performance Assessment.* Mary C. Comerio, editor. November 2005.

PEER 2005/11 *Van Nuys Hotel Building Testbed Report: Exercising Seismic Performance Assessment*. Helmut Krawinkler, editor. October 2005.

PEER 2005/10 *First NEES/E-Defense Workshop on Collapse Simulation of Reinforced Concrete Building Structures.* September 2005.

PEER 2005/09 *Test Applications of Advanced Seismic Assessment Guidelines.* Joe Maffei, Karl Telleen, Danya Mohr, William Holmes, and Yuki Nakayama. August 2006.

PEER 2005/08 *Damage Accumulation in Lightly Confined Reinforced Concrete Bridge Columns.* R. Tyler Ranf, Jared M. Nelson, Zach Price, Marc O. Eberhard, and John F. Stanton. April 2006.

PEER 2005/07 *Experimental and Analytical Studies on the Seismic Response of Freestanding and Anchored Laboratory Equipment.* Dimitrios Konstantinidis and Nicos Makris. January 2005.

PEER 2005/06 *Global Collapse of Frame Structures under Seismic Excitations*. Luis F. Ibarra and Helmut Krawinkler. September 2005.

PEER 2005//05 *Performance Characterization of Bench- and Shelf-Mounted Equipment.* Samit Ray Chaudhuri and Tara C. Hutchinson. May 2006.

PEER 2005/04 *Numerical Modeling of the Nonlinear Cyclic Response of Shallow Foundations.* Chad Harden, Tara Hutchinson, Geoffrey R. Martin, and Bruce L. Kutter. August 2005.

PEER 2005/03 *A Taxonomy of Building Components for Performance-Based Earthquake Engineering.* Keith A. Porter. September 2005.

PEER 2005/02 *Fragility Basis for California Highway Overpass Bridge Seismic Decision Making.* Kevin R. Mackie and Božidar Stojadinović. June 2005.

PEER 2005/01 *Empirical Characterization of Site Conditions on Strong Ground Motion.* Jonathan P. Stewart, Yoojoong Choi, and Robert W. Graves. June 2005.

PEER 2004/09 *Electrical Substation Equipment Interaction: Experimental Rigid Conductor Studies.* Christopher Stearns and André Filiatrault. February 2005.

PEER 2004/08 *Seismic Qualification and Fragility Testing of Line Break 550-kV Disconnect Switches.* Shakhzod M. Takhirov, Gregory L. Fenves, and Eric Fujisaki. January 2005.

PEER 2004/07 *Ground Motions for Earthquake Simulator Qualification of Electrical Substation Equipment.* Shakhzod M. Takhirov, Gregory L. Fenves, Eric Fujisaki, and Don Clyde. January 2005.

PEER 2004/06 *Performance-Based Regulation and Regulatory Regimes.* Peter J. May and Chris Koski. September 2004.

PEER 2004/05 *Performance-Based Seismic Design Concepts and Implementation: Proceedings of an International Workshop.* Peter Fajfar and Helmut Krawinkler, editors. September 2004.

PEER 2004/04 *Seismic Performance of an Instrumented Tilt-up Wall Building.* James C. Anderson and Vitelmo V. Bertero. July 2004.

PEER 2004/03 *Evaluation and Application of Concrete Tilt-up Assessment Methodologies.* Timothy Graf and James O. Malley. October 2004.

PEER 2004/02 *Analytical Investigations of New Methods for Reducing Residual Displacements of Reinforced Concrete Bridge Columns*. Junichi Sakai and Stephen A. Mahin. August 2004.

PEER 2004/01 *Seismic Performance of Masonry Buildings and Design Implications.* Kerri Anne Taeko Tokoro, James C. Anderson, and Vitelmo V. Bertero. February 2004.

PEER 2003/18 *Performance Models for Flexural Damage in Reinforced Concrete Columns.* Michael Berry and Marc Eberhard. August 2003.

PEER 2003/17 *Predicting Earthquake Damage in Older Reinforced Concrete Beam-Column Joints.* Catherine Pagni and Laura Lowes. October 2004.

PEER 2003/16 *Seismic Demands for Performance-Based Design of Bridges.* Kevin Mackie and Božidar Stojadinović. August 2003.

PEER 2003/15 *Seismic Demands for Nondeteriorating Frame Structures and Their Dependence on Ground Motions.* Ricardo Antonio Medina and Helmut Krawinkler. May 2004.

PEER 2003/14 *Finite Element Reliability and Sensitivity Methods for Performance-Based Earthquake Engineering.* Terje Haukaas and Armen Der Kiureghian. April 2004.

PEER 2003/13 *Effects of Connection Hysteretic Degradation on the Seismic Behavior of Steel Moment-Resisting Frames.* Janise E. Rodgers and Stephen A. Mahin. March 2004.

PEER 2003/12 *Implementation Manual for the Seismic Protection of Laboratory Contents: Format and Case Studies.* William T. Holmes and Mary C. Comerio. October 2003.

PEER 2003/11 *Fifth U.S.-Japan Workshop on Performance-Based Earthquake Engineering Methodology for Reinforced Concrete Building Structures.* February 2004.

PEER 2003/10 *A Beam-Column Joint Model for Simulating the Earthquake Response of Reinforced Concrete Frames.* Laura N. Lowes, Nilanjan Mitra, and Arash Altoontash. February 2004.

PEER 2003/09 *Sequencing Repairs after an Earthquake: An Economic Approach.* Marco Casari and Simon J. Wilkie. April 2004.

PEER 2003/08 *A Technical Framework for Probability-Based Demand and Capacity Factor Design (DCFD) Seismic Formats*. Fatemeh Jalayer and C. Allin Cornell. November 2003.

PEER 2003/07 *Uncertainty Specification and Propagation for Loss Estimation Using FOSM Methods.* Jack W. Baker and C. Allin Cornell. September 2003.

PEER 2003/06 *Performance of Circular Reinforced Concrete Bridge Columns under Bidirectional Earthquake Loading.* Mahmoud M. Hachem, Stephen A. Mahin, and Jack P. Moehle. February 2003.

PEER 2003/05 *Response Assessment for Building-Specific Loss Estimation.* Eduardo Miranda and Shahram Taghavi. September 2003.

PEER 2003/04 *Experimental Assessment of Columns with Short Lap Splices Subjected to Cyclic Loads*. Murat Melek, John W. Wallace, and Joel Conte. April 2003.

PEER 2003/03 *Probabilistic Response Assessment for Building-Specific Loss Estimation.* Eduardo Miranda and Hesameddin Aslani. September 2003.

PEER 2003/02 *Software Framework for Collaborative Development of Nonlinear Dynamic Analysis Program.* Jun Peng and Kincho H. Law. September 2003.

PEER 2003/01 *Shake Table Tests and Analytical Studies on the Gravity Load Collapse of Reinforced Concrete Frames.* Kenneth John Elwood and Jack P. Moehle. November 2003.

PEER 2002/24 *Performance of Beam to Column Bridge Joints Subjected to a Large Velocity Pulse.* Natalie Gibson, André Filiatrault, and Scott A. Ashford. April 2002.

PEER 2002/23 *Effects of Large Velocity Pulses on Reinforced Concrete Bridge Columns.* Greg L. Orozco and Scott A. Ashford. April 2002.

PEER 2002/22 *Characterization of Large Velocity Pulses for Laboratory Testing.* Kenneth E. Cox and Scott A. Ashford. April 2002.

PEER 2002/21 *Fourth U.S.-Japan Workshop on Performance-Based Earthquake Engineering Methodology for Reinforced Concrete Building Structures*. December 2002.

PEER 2002/20 *Barriers to Adoption and Implementation of PBEE Innovations.* Peter J. May. August 2002.

PEER 2002/19 *Economic-Engineered Integrated Models for Earthquakes: Socioeconomic Impacts.* Peter Gordon, James E. Moore II, and Harry W. Richardson. July 2002.

PEER 2002/18 *Assessment of Reinforced Concrete Building Exterior Joints with Substandard Details.* Chris P. Pantelides, Jon Hansen, Justin Nadauld, and Lawrence D. Reaveley. May 2002.

PEER 2002/17 *Structural Characterization and Seismic Response Analysis of a Highway Overcrossing Equipped with Elastomeric Bearings and Fluid Dampers: A Case Study.* Nicos Makris and Jian Zhang. November 2002.

PEER 2002/16 *Estimation of Uncertainty in Geotechnical Properties for Performance-Based Earthquake Engineering.* Allen L. Jones, Steven L. Kramer, and Pedro Arduino. December 2002.

PEER 2002/15 *Seismic Behavior of Bridge Columns Subjected to Various Loading Patterns*. Asadollah Esmaeily-Gh. and Yan Xiao. December 2002.

PEER 2002/14 *Inelastic Seismic Response of Extended Pile Shaft Supported Bridge Structures.* T.C. Hutchinson, R.W. Boulanger, Y.H. Chai, and I.M. Idriss. December 2002.

PEER 2002/13 *Probabilistic Models and Fragility Estimates for Bridge Components and Systems.* Paolo Gardoni, Armen Der Kiureghian, and Khalid M. Mosalam. June 2002.

PEER 2002/12 *Effects of Fault Dip and Slip Rake on Near-Source Ground Motions: Why Chi-Chi Was a Relatively Mild M7.6 Earthquake.* Brad T. Aagaard, John F. Hall, and Thomas H. Heaton. December 2002.

PEER 2002/11 *Analytical and Experimental Study of Fiber-Reinforced Strip Isolators*. James M. Kelly and Shakhzod M. Takhirov. September 2002.

PEER 2002/10 *Centrifuge Modeling of Settlement and Lateral Spreading with Comparisons to Numerical Analyses***.** Sivapalan Gajan and Bruce L. Kutter. January 2003.

PEER 2002/09 *Documentation and Analysis of Field Case Histories of Seismic Compression during the 1994 Northridge, California, Earthquake.* Jonathan P. Stewart, Patrick M. Smith, Daniel H. Whang, and Jonathan D. Bray. October 2002.

PEER 2002/08 *Component Testing, Stability Analysis and Characterization of Buckling-Restrained Unbonded Braces™.* Cameron Black, Nicos Makris, and Ian Aiken. September 2002.

PEER 2002/07 *Seismic Performance of Pile-Wharf Connections.* Charles W. Roeder, Robert Graff, Jennifer Soderstrom, and Jun Han Yoo. December 2001.

PEER 2002/06 *The Use of Benefit-Cost Analysis for Evaluation of Performance-Based Earthquake Engineering Decisions*. Richard O. Zerbe and Anthony Falit-Baiamonte. September 2001.

PEER 2002/05 *Guidelines, Specifications, and Seismic Performance Characterization of Nonstructural Building Components and Equipment*. André Filiatrault, Constantin Christopoulos, and Christopher Stearns. September 2001.

PEER 2002/04 *Consortium of Organizations for Strong-Motion Observation Systems and the Pacific Earthquake Engineering Research Center Lifelines Program: Invited Workshop on Archiving and Web Dissemination of Geotechnical Data, 4–5 October 2001*. September 2002.

PEER 2002/03 *Investigation of Sensitivity of Building Loss Estimates to Major Uncertain Variables for the Van Nuys Testbed.* Keith A. Porter, James L. Beck, and Rustem V. Shaikhutdinov. August 2002.

PEER 2002/02 *The Third U.S.-Japan Workshop on Performance-Based Earthquake Engineering Methodology for Reinforced Concrete Building Structures*. July 2002.

PEER 2002/01 *Nonstructural Loss Estimation: The UC Berkeley Case Study.* Mary C. Comerio and John C. Stallmeyer. December 2001.

PEER 2001/16 *Statistics of SDF-System Estimate of Roof Displacement for Pushover Analysis of Buildings.* Anil K. Chopra, Rakesh K. Goel, and Chatpan Chintanapakdee. December 2001.

PEER 2001/15 *Damage to Bridges during the 2001 Nisqually Earthquake.* R. Tyler Ranf, Marc O. Eberhard, and Michael P. Berry. November 2001.

PEER 2001/14 *Rocking Response of Equipment Anchored to a Base Foundation.* Nicos Makris and Cameron J. Black. September 2001.

PEER 2001/13 *Modeling Soil Liquefaction Hazards for Performance-Based Earthquake Engineering.* Steven L. Kramer and Ahmed-W. Elgamal. February 2001.

PEER 2001/12 *Development of Geotechnical Capabilities in OpenSees.* Boris Jeremić. September 2001.

PEER 2001/11 *Analytical and Experimental Study of Fiber-Reinforced Elastomeric Isolators*. James M. Kelly and Shakhzod M. Takhirov. September 2001.

PEER 2001/10 *Amplification Factors for Spectral Acceleration in Active Regions.* Jonathan P. Stewart, Andrew H. Liu, Yoojoong Choi, and Mehmet B. Baturay. December 2001.

PEER 2001/09 *Ground Motion Evaluation Procedures for Performance-Based Design.* Jonathan P. Stewart, Shyh-Jeng Chiou, Jonathan D. Bray, Robert W. Graves, Paul G. Somerville, and Norman A. Abrahamson. September 2001.

PEER 2001/08 *Experimental and Computational Evaluation of Reinforced Concrete Bridge Beam-Column Connections for Seismic Performance.* Clay J. Naito, Jack P. Moehle, and Khalid M. Mosalam. November 2001.

PEER 2001/07 *The Rocking Spectrum and the Shortcomings of Design Guidelines.* Nicos Makris and Dimitrios Konstantinidis. August 2001.

PEER 2001/06 *Development of an Electrical Substation Equipment Performance Database for Evaluation of Equipment Fragilities*. Thalia Agnanos. April 1999.

PEER 2001/05 *Stiffness Analysis of Fiber-Reinforced Elastomeric Isolators.* Hsiang-Chuan Tsai and James M. Kelly. May 2001.

PEER 2001/04 *Organizational and Societal Considerations for Performance-Based Earthquake Engineering.* Peter J. May. April 2001.

PEER 2001/03 *A Modal Pushover Analysis Procedure to Estimate Seismic Demands for Buildings: Theory and Preliminary Evaluation.* Anil K. Chopra and Rakesh K. Goel. January 2001.

PEER 2001/02 *Seismic Response Analysis of Highway Overcrossings Including Soil-Structure Interaction.* Jian Zhang and Nicos Makris. March 2001.

PEER 2001/01 *Experimental Study of Large Seismic Steel Beam-to-Column Connections.* Egor P. Popov and Shakhzod M. Takhirov. November 2000.

PEER 2000/10 *The Second U.S.-Japan Workshop on Performance-Based Earthquake Engineering Methodology for Reinforced Concrete Building Structures.* March 2000.

PEER 2000/09 *Structural Engineering Reconnaissance of the August 17, 1999 Earthquake: Kocaeli (Izmit), Turkey.* Halil Sezen, Kenneth J. Elwood, Andrew S. Whittaker, Khalid Mosalam, John J. Wallace, and John F. Stanton. December 2000.

PEER 2000/08 *Behavior of Reinforced Concrete Bridge Columns Having Varying Aspect Ratios and Varying Lengths of Confinement.* Anthony J. Calderone, Dawn E. Lehman, and Jack P. Moehle. January 2001.

PEER 2000/07 *Cover-Plate and Flange-Plate Reinforced Steel Moment-Resisting Connections.* Taejin Kim, Andrew S. Whittaker, Amir S. Gilani, Vitelmo V. Bertero, and Shakhzod M. Takhirov. September 2000.

PEER 2000/06 *Seismic Evaluation and Analysis of 230-kV Disconnect Switches.* Amir S. J. Gilani, Andrew S. Whittaker, Gregory L. Fenves, Chun-Hao Chen, Henry Ho, and Eric Fujisaki. July 2000.

PEER 2000/05 *Performance-Based Evaluation of Exterior Reinforced Concrete Building Joints for Seismic Excitation.* Chandra Clyde, Chris P. Pantelides, and Lawrence D. Reaveley. July 2000.

PEER 2000/04 *An Evaluation of Seismic Energy Demand: An Attenuation Approach.* Chung-Che Chou and Chia-Ming Uang. July 1999.

PEER 2000/03 *Framing Earthquake Retrofitting Decisions: The Case of Hillside Homes in Los Angeles.* Detlof von Winterfeldt, Nels Roselund, and Alicia Kitsuse. March 2000.

PEER 2000/02 *U.S.-Japan Workshop on the Effects of Near-Field Earthquake Shaking.* Andrew Whittaker, ed. July 2000.

PEER 2000/01 *Further Studies on Seismic Interaction in Interconnected Electrical Substation Equipment.* Armen Der Kiureghian, Kee-Jeung Hong, and Jerome L. Sackman. November 1999.

PEER 1999/14 *Seismic Evaluation and Retrofit of 230-kV Porcelain Transformer Bushings*. Amir S. Gilani, Andrew S. Whittaker, Gregory L. Fenves, and Eric Fujisaki. December 1999.

PEER 1999/13 *Building Vulnerability Studies: Modeling and Evaluation of Tilt-up and Steel Reinforced Concrete Buildings.* John W. Wallace, Jonathan P. Stewart, and Andrew S. Whittaker, editors. December 1999.

PEER 1999/12 *Rehabilitation of Nonductile RC Frame Building Using Encasement Plates and Energy-Dissipating Devices.* Mehrdad Sasani, Vitelmo V. Bertero, James C. Anderson. December 1999.

PEER 1999/11 *Performance Evaluation Database for Concrete Bridge Components and Systems under Simulated Seismic Loads.* Yael D. Hose and Frieder Seible. November 1999.

PEER 1999/10 *U.S.-Japan Workshop on Performance-Based Earthquake Engineering Methodology for Reinforced Concrete Building Structures.* December 1999.

PEER 1999/09 *Performance Improvement of Long Period Building Structures Subjected to Severe Pulse-Type Ground Motions*. James C. Anderson, Vitelmo V. Bertero, and Raul Bertero. October 1999.

PEER 1999/08 *Envelopes for Seismic Response Vectors.* Charles Menun and Armen Der Kiureghian. July 1999.

PEER 1999/07 *Documentation of Strengths and Weaknesses of Current Computer Analysis Methods for Seismic Performance of Reinforced Concrete Members.* William F. Cofer. November 1999.

PEER 1999/06 *Rocking Response and Overturning of Anchored Equipment under Seismic Excitations.* Nicos Makris and Jian Zhang. November 1999.

PEER 1999/05 *Seismic Evaluation of 550 kV Porcelain Transformer Bushings.* Amir S. Gilani, Andrew S. Whittaker, Gregory L. Fenves, and Eric Fujisaki. October 1999.

PEER 1999/04 *Adoption and Enforcement of Earthquake Risk-Reduction Measures.* Peter J. May, Raymond J. Burby, T. Jens Feeley, and Robert Wood.

PEER 1999/03 *Task 3 Characterization of Site Response General Site Categories*. Adrian Rodriguez-Marek, Jonathan D. Bray, and Norman Abrahamson. February 1999.

PEER 1999/02 *Capacity-Demand-Diagram Methods for Estimating Seismic Deformation of Inelastic Structures: SDF Systems*. Anil K. Chopra and Rakesh Goel. April 1999.

PEER 1999/01 *Interaction in Interconnected Electrical Substation Equipment Subjected to Earthquake Ground Motions.* Armen Der Kiureghian, Jerome L. Sackman, and Kee-Jeung Hong. February 1999.

PEER 1998/08 *Behavior and Failure Analysis of a Multiple-Frame Highway Bridge in the 1994 Northridge Earthquake.* Gregory L. Fenves and Michael Ellery. December 1998.

PEER 1998/07 *Empirical Evaluation of Inertial Soil-Structure Interaction Effects.* Jonathan P. Stewart, Raymond B. Seed, and Gregory L. Fenves. November 1998.

PEER 1998/06 *Effect of Damping Mechanisms on the Response of Seismic Isolated Structures.* Nicos Makris and Shih-Po Chang. November 1998.

PEER 1998/05 *Rocking Response and Overturning of Equipment under Horizontal Pulse-Type Motions.* Nicos Makris and Yiannis Roussos. October 1998.

PEER 1998/04 *Pacific Earthquake Engineering Research Invitational Workshop Proceedings, May 14–15, 1998: Defining the Links between Planning, Policy Analysis, Economics and Earthquake Engineering.* Mary Comerio and Peter Gordon. September 1998.

PEER 1998/03 *Repair/Upgrade Procedures for Welded Beam to Column Connections.* James C. Anderson and Xiaojing Duan. May 1998.

PEER 1998/02 *Seismic Evaluation of 196 kV Porcelain Transformer Bushings.* Amir S. Gilani, Juan W. Chavez, Gregory L. Fenves, and Andrew S. Whittaker. May 1998.

PEER 1998/01 *Seismic Performance of Well-Confined Concrete Bridge Columns.* Dawn E. Lehman and Jack P. Moehle. December 2000.

ONLINE REPORTS

The following PEER reports are available by Internet only at http://peer.berkeley.edu/publications/peer_reports.html

PEER 2012/101 *Mechanics of Fiber Reinforced Bearings.* James M. Kelly and Andrea Calabrese. February 2012.

PEER 2011/107 *Nonlinear Site Response and Seismic Compression at Vertical Array Strongly Shaken by 2007 Niigata-ken Chuetsu-oki Earthquake.* Eric Yee, Jonathan P. Stewart, and Kohji Tokimatsu. December 2011.

PEER 2011/106 *Self Compacting Hybrid Fiber Reinforced Concrete Composites for Bridge Columns.* Pardeep Kumar, Gabriel Jen, William Trono, Marios Panagiotou, and Claudia Ostertag. September 2011.

PEER 2011/105 *Stochastic Dynamic Analysis of Bridges Subjected to Spacially Varying Ground Motions.* Katerina Konakli and Armen Der Kiureghian. August 2011.

PEER 2011/104 *Design and Instrumentation of the 2010 E-Defense Four-Story Reinforced Concrete and Post-Tensioned Concrete Buildings.* Takuya Nagae, Kenichi Tahara, Taizo Matsumori, Hitoshi Shiohara, Toshimi Kabeyasawa, Susumu Kono, Minehiro Nishiyama (Japanese Research Team) and John Wallace, Wassim Ghannoum, Jack Moehle, Richard Sause, Wesley Keller, Zeynep Tuna (U.S. Research Team). June 2011.

PEER 2011/103 *In-Situ Monitoring of the Force Output of Fluid Dampers: Experimental Investigation.* Dimitrios Konstantinidis, James M. Kelly, and Nicos Makris. April 2011.

PEER 2011/102 *Ground-motion prediction equations 1964 - 2010.* John Douglas. April 2011.

PEER 2011/101 *Report of the Eighth Planning Meeting of NEES/E-Defense Collaborative Research on Earthquake Engineering.* Convened by the Hyogo Earthquake Engineering Research Center (NIED), NEES Consortium, Inc. February 2011.

PEER 2010/111 *Modeling and Acceptance Criteria for Seismic Design and Analysis of Tall Buildings.* Task 7 Report for the Tall Buildings Initiative - Published jointly by the Applied Technology Council. October 2010.

PEER 2010/110 *Seismic Performance Assessment and Probabilistic Repair Cost Analysis of Precast Concrete Cladding Systems for Multistory Buildlings.* Jeffrey P. Hunt and Božidar Stojadinovic. November 2010.

PEER 2010/109 *Report of the Seventh Joint Planning Meeting of NEES/E-Defense Collaboration on Earthquake Engineering. Held at the E-Defense, Miki, and Shin-Kobe, Japan, September 18–19, 2009*. August 2010.

PEER 2010/108 *Probabilistic Tsunami Hazard in California.* Hong Kie Thio, Paul Somerville, and Jascha Polet, preparers. October 2010.

PEER 2010/107 *Performance and Reliability of Exposed Column Base Plate Connections for Steel Moment-Resisting Frames.* Ady Aviram, Božidar Stojadinovic, and Armen Der Kiureghian. August 2010.

PEER 2010/106 *Verification of Probabilistic Seismic Hazard Analysis Computer Programs.* Patricia Thomas, Ivan Wong, and Norman Abrahamson. May 2010.

PEER 2010/105 *Structural Engineering Reconnaissance of the April 6, 2009, Abruzzo, Italy, Earthquake, and Lessons Learned.* M. Selim Günay and Khalid M. Mosalam. April 2010.

PEER 2010/104 *Simulating the Inelastic Seismic Behavior of Steel Braced Frames, Including the Effects of Low-Cycle Fatigue.* Yuli Huang and Stephen A. Mahin. April 2010.

PEER 2010/103 *Post-Earthquake Traffic Capacity of Modern Bridges in California.* Vesna Terzic and Božidar Stojadinović. March 2010.

PEER 2010/102 *Analysis of Cumulative Absolute Velocity (CAV) and JMA Instrumental Seismic Intensity (I_{JMA}) Using the PEER–NGA Strong Motion Database.* Kenneth W. Campbell and Yousef Bozorgnia. February 2010.

PEER 2010/101 *Rocking Response of Bridges on Shallow Foundations.* Jose A. Ugalde, Bruce L. Kutter, and Boris Jeremic. April 2010.

PEER 2009/109 *Simulation and Performance-Based Earthquake Engineering Assessment of Self-Centering Post-Tensioned Concrete Bridge Systems.* Won K. Lee and Sarah L. Billington. December 2009.

PEER 2009/108 *PEER Lifelines Geotechnical Virtual Data Center.* J. Carl Stepp, Daniel J. Ponti, Loren L. Turner, Jennifer N. Swift, Sean Devlin, Yang Zhu, Jean Benoit, and John Bobbitt. September 2009.

PEER 2009/107 *Experimental and Computational Evaluation of Current and Innovative In-Span Hinge Details in Reinforced Concrete Box-Girder Bridges: Part 2: Post-Test Analysis and Design Recommendations.* Matias A. Hube and Khalid M. Mosalam. December 2009.

PEER 2009/106 *Shear Strength Models of Exterior Beam-Column Joints without Transverse Reinforcement.* Sangjoon Park and Khalid M. Mosalam. November 2009.

PEER 2009/105 *Reduced Uncertainty of Ground Motion Prediction Equations through Bayesian Variance Analysis.* Robb Eric S. Moss. November 2009.

PEER 2009/104 *Advanced Implementation of Hybrid Simulation.* Andreas H. Schellenberg, Stephen A. Mahin, Gregory L. Fenves. November 2009.

PEER 2009/103 *Performance Evaluation of Innovative Steel Braced Frames.* T. Y. Yang, Jack P. Moehle, and Božidar Stojadinovic. August 2009.

PEER 2009/102 *Reinvestigation of Liquefaction and Nonliquefaction Case Histories from the 1976 Tangshan Earthquake.* Robb Eric Moss, Robert E. Kayen, Liyuan Tong, Songyu Liu, Guojun Cai, and Jiaer Wu. August 2009.

PEER 2009/101 *Report of the First Joint Planning Meeting for the Second Phase of NEES/E-Defense Collaborative Research on Earthquake Engineering.* Stephen A. Mahin et al. July 2009.

PEER 2008/104 *Experimental and Analytical Study of the Seismic Performance of Retaining Structures.* Linda Al Atik and Nicholas Sitar. January 2009.

PEER 2008/103 *Experimental and Computational Evaluation of Current and Innovative In-Span Hinge Details in Reinforced Concrete Box-Girder Bridges. Part 1: Experimental Findings and Pre-Test Analysis.* Matias A. Hube and Khalid M. Mosalam. January 2009.

PEER 2008/102 *Modeling of Unreinforced Masonry Infill Walls Considering In-Plane and Out-of-Plane Interaction.* Stephen Kadysiewski and Khalid M. Mosalam. January 2009.

PEER 2008/101 *Seismic Performance Objectives for Tall Buildings.* William T. Holmes, Charles Kircher, William Petak, and Nabih Youssef. August 2008.

PEER 2007/101 *Generalized Hybrid Simulation Framework for Structural Systems Subjected to Seismic Loading.* Tarek Elkhoraibi and Khalid M. Mosalam. July 2007.

PEER 2007/100 *Seismic Evaluation of Reinforced Concrete Buildings Including Effects of Masonry Infill Walls.* Alidad Hashemi and Khalid M. Mosalam. July 2007.

The Pacific Earthquake Engineering Research Center (PEER) is a multi-institutional research and education center with headquarters at the University of California, Berkeley. Investigators from over 20 universities, several consulting companies, and researchers at various state and federal government agencies contribute to research programs focused on performance-based earthquake engineering.

These research programs aim to identify and reduce the risks from major earthquakes to life safety and to the economy by including research in a wide variety of disciplines including structural and geotechnical engineering, geology/seismology, lifelines, transportation, architecture, economics, risk management, and public policy.

PEER is supported by federal, state, local, and regional agencies, together with industry partners.

PEER Core Institutions:
University of California, Berkeley (Lead Institution)
California Institute of Technology
Oregon State University
Stanford University
University of California, Davis
University of California, Irvine
University of California, Los Angeles
University of California, San Diego
University of Southern California
University of Washington

PEER reports can be ordered at http://peer.berkeley.edu/publications/peer_reports.html or by contacting

Pacific Earthquake Engineering Research Center
University of California, Berkeley
325 Davis Hall, mail code 1792
Berkeley, CA 94720-1792
Tel: 510-642-3437
Fax: 510-642-1655
Email: peer_editor@berkeley.edu

ISSN 1547-0587X